Understanding the effects of volumetric defects on the uniaxial fatigue behavior of additively manufactured metallic materials

by

Muztahid Muhammad

A dissertation submitted to the Graduate Faculty of
Auburn University
in partial fulfillment of the
requirements for the Degree of
Doctor of Philosophy

Auburn, Alabama
August 9, 2025

Keywords: Additive manufacturing; Laser powder bed fusion; Fatigue behavior; Defect size; Defect shape; Fatigue design curve.

Approved by

Nima Shamsaei, Chair, Philpott-WestPoint Stevens Distinguished Professor, Department of Mechanical Engineering
Shuai Shao, McWane Associate Professor, Department of Mechanical Engineering
Stefano Beretta, Professor, Department of Mechanical Engineering
Jingyi Zheng, Associate Professor, Department of Mathematics and Statistics
Jia Liu, Associate Professor, Department of Industrial and Systems Engineering

Abstract

Volumetric defects in additively manufactured parts cause significant fatigue scatter due to the variations in their size, shape, and location. This dissertation aimed to identify the morphological features of process-induced volumetric defects that most influence the fatigue behavior of laser powder bed fused (L-PBF) Ti-6Al-4V. Firstly, fatigue test specimens were machined from round bars fabricated using eight distinct process parameter sets and three build orientations to ensure a wide range of defect morphologies and populations. Uniaxial, constant amplitude, fully-reversed fatigue tests were conducted on these specimens. Fractography was performed to identify the defect responsible for the fatigue crack initiation and extract its morphological features. The influence of these features on fatigue behavior was examined by analyzing experimental data and finite element analysis results. While size was the most critical defect feature influencing fatigue behavior, it could not fully explain the variation in fatigue life by itself. For defects of similar size located at the same location, circular defects appeared to be more detrimental than irregularly shaped ones. A new defect size parameter, $\sqrt{area}$ of the maximum inscribed circle, was introduced to account for both the size and shape of the volumetric defects, which exhibited an improved correlation with life compared to existing parameters. Fatigue cracks initiated from the surface and internal defects exhibited distinct crack growth behavior. Using the distinct material constants for surface and internal defects obtained from the Shiozawa plots, a novel fatigue life prediction model was proposed, which accounted for the distinct crack growth rates for surface and internal defects. Additionally, a probabilistic approach was utilized to determine the size of the largest possible defect for a given probability of failure. The fatigue design curve estimated with this defect size, using the proposed crack growth model, has been

shown to be a more accurate estimate compared to the design curves developed using conventional approaches for fatigue qualification. Furthermore, the cross-platform transferability of the structure-property relationships, specifically defect-fatigue, was assessed for L-PBF Ti-6Al-4V. The transferability of defect-fatigue relationships established for the specimens fabricated on the EOS M290 platform was tested and validated with those fabricated on the Renishaw RenAM 500Q platform. Fatigue crack growth parameters derived from the EOS M290 specimens could be successfully applied to the fatigue life prediction of the RenAM 500Q specimens. The validity of fatigue design curves constructed using the short crack growth model with parameters from the EOS M290 platform was verified with data from the RenAM 500Q.

Acknowledgments

I would like to sincerely thank my advisor, Dr. Nima Shamsaei, for his relentless guidance, encouragement, and support throughout my PhD journey. Without his mentorship—from countless meetings to detailed feedback on research results and papers—this dissertation would not have been possible. I am also deeply grateful to Dr. Shuai Shao for his mentorship and technical insight. His guidance and feedback helped lay the foundation for this dissertation. In addition, I thank Dr. Stefano Beretta for his guidance, feedback, and support throughout the project. I would like to thank Dr. Jingyi Zheng for her time and support as a member of my PhD committee, and Dr. Jia Liu for serving as the University Reader and offering helpful comments on my dissertation. I am also thankful to Dr. Sajith Soman for his collaboration and support throughout the later stages of this work.

This research was made possible through the financial support of Auburn University, the Federal Aviation Administration (FAA) under Cooperative Agreement 12-C-AM-AU, and the National Science Foundation (NSF) under grants #1919818 and #2118756. I am grateful for their support. Finally, I would like to thank my parents, family, and friends for always being there, and my colleagues at the National Center for Additive Manufacturing Excellence (NCAME) for their support, feedback, and camaraderie along the way.

Table of Contents

List of Tables

List of Figures

Abbreviations

2D	Two-dimensional
3D	Three-dimensional
AM	Additive manufacturing/Additively manufactured
BSE	Back-scattered electron
D	Diagonal
E	Energy density
GEP	Gas-entrapped pore
H	Horizontal
KH	Keyhole
LEVD	Largest extreme value distribution
LoF	Lack of fusion
L-PBF	Laser powder bed fusion/fused
MIC	Maximum inscribed circle
O	Overheated
PDF	Probability density function
R	Recommended
SEM	Scanning electron microscope
SIF	Stress intensity factor
U	Underheated
V	Vertical
XCT	X-ray computed tomography

Nomenclature

%El	Percent elongation to failure
$a_{99\%}$	Critical defect of size of 99% probability of occurrence
a_i	Initial crack radius
$\sqrt{area}_{eff}$	$\sqrt{area}$ enveloping the defect and free surface
$\sqrt{area}_f$	Square root of the area of the crack at the final loading cycle
$\sqrt{area}_i$	Square root of the area of the crack at the first loading cycle
$\sqrt{area}_{Murakami}$	Murakami's $\sqrt{area}$
$2N_f$	Reversals to failure
e	Distance from the free surface to the nearest point of the defect
h	Hatch spacing
P	Laser power
R_σ	Stress ratio
S_u	Ultimate tensile strength
S_y	Yield strength
t	Layer thickness
v	Laser speed
Y_i	Reduced variate
δ	Extreme values distribution shape parameter
λ	Extreme values distribution location parameter
σ_a	Stress amplitude
$\rho_{relative}$	Relative density
C	Coefficient of Paris-Erdogan curve
e	Distance from the free surface to the nearest point of the defect
$F_{(max,1spec)}(x)$	Cumulative distribution function for the largest defect size expected in 1 specimen
$F_{(max,100specs)}(x)$	Cumulative distribution function for the largest defect size expected across a set of 100 specimens
m	Exponent of Paris-Erdogan curve
N_f	Cycles to failure
P_f	Failure probability
R_σ	Stress ratio
R_{eff}	Effective stress ratio
s	Standard deviation
Y	Murakami's location dependent factor

1. Introduction

1.1. Background and motivation

Additive manufacturing (AM) is a fabrication process that joins materials layer-by-layer and track-by-track from three-dimensional model data, as opposed to the traditional subtractive processes [1]. AM technology has the potential to revolutionize the manufacturing sector, especially for the fabrication of components with complex geometries (e.g., heat exchanger), components requiring multiple part assemblies (e.g., fuel nozzle), or applications requiring customized design (e.g., implant, brace, etc.). AM techniques are particularly suitable for fabricating intricate parts using materials that are difficult to machine, such as Ti-6Al-4V. However, process-induced volumetric defects are inherent to the additively manufactured (AM) parts in the current state of AM technology, which can initiate fatigue cracks in the machined surface condition. This phenomenon is particularly critical for the defect sensitive materials, such as Ti-6Al-4V.

The fatigue behavior of AM materials with finer microstructure, such as Ti-6Al-4V, is primarily governed by the process-induced volumetric defects in the machined surface condition [2–5]. These process-induced volumetric defects can be categorized into three types: lack of fusion (LoF), keyhole (KH), and gas-entrapped pore (GEP). LoFs are typically formed in the AM parts when there is insufficient energy input during the formation, which can be caused by various reasons, including lower power input, higher scanning speed, larger hatching distance, etc. [6]. On the other hand, KHs can be formed as a result of "pinch-off" from the bottom of the depression in the melt-pool due to excessive energy input during the fabrication, which can be caused by higher laser power, lower scanning speed, etc. [7,8]. GEP can be formed due to the entrapment of the inert gases within the melt-pool due to the combined effect of the Marangoni force, vapor coil induced turbulence, and buoyancy during the fabrication of the parts [9]. In AM, there are infinite possibilities of combinations of feedstocks (e.g., morphology and rheology of powder, powder recycling, etc.), process parameters (such as laser powder, scanning speed, hatching space, etc.), design parameters of the part (i.e., part volume, orientation, sudden change of geometry within the same part, etc.), design of the platform (such as powder delivery mechanism, types of laser, number of lasers, inert gas delivery method, inert gas type, etc.), etc., all of which can influence the defect population and defect characteristics of the AM parts [10–13]. Since fatigue is a localized and permanent structural change [14], the presence of such volumetric defects can significantly impact the fatigue behavior of the AM parts by reducing fatigue life, knocking down the fatigue strength, and causing scatter in the fatigue data [15].

The stress concentration around the volumetric defects varies depending on the morphological features of the defects (such as their size and shape [8,16–18]) and location [4,19]. The effect of crack-initiating volumetric defect size on the fatigue behavior of materials is relatively well studied. The findings suggest the inverse correlation between the fatigue critical defect size and the fatigue life or fatigue limit [20–22]. The location of the volumetric defect with respect to the free surface is another factor that influences the fatigue behavior of the AM metallic parts. Regarding the effect of location, defects located near free surfaces have been shown to be more detrimental than internal ones [22–25]. For modeling the effect of location, Murakami et al. distinguished between surface and internal defects based on the ratio of the defect's distance to the surface to its size along that direction and assigned a coefficient to the stress intensity factor (SIF), which was greater for surface defects and smaller for internal ones [26]. In contrast, the effect of volumetric defects' shape is more complex and thus less understood. While literature generally acknowledges the effect of defect shape, there exists a lack of consensus regarding the difference in fatigue behaviors of different defect types, such as LoF and KH, of the same size [27,28]. A robust defect sensitive model, incorporating the effect of defect morphologies, can be one of the solutions to facilitate broader industrial use of AM parts and establish their trustworthiness.

Contingent to the volumetric defects governing the fatigue behavior and the large scatter of fatigue data of AM parts, using conventional fatigue qualification approaches for AM parts typically leads to either overdesign (resulting in weight penalties) or noncompliance (due to insufficient reliability) [29–31]. Due to the defect accelerated crack initiation, the use of traditional linear elastic fracture mechanics based fatigue life prediction approaches, where fatigue life is calculated by integrating crack growth rate functions, may be a promising option to overcome the challenges faced by conventional qualifying approaches for AM materials. In fact, the “short crack” growth approach has been the foundation of some fatigue life estimation tools, such as NASGRO [32,33] and AFGROW [34,35], etc., which could successfully describe the stress-life diagrams and fatigue responses of materials in the presence of volumetric anomalies. Nevertheless, there are still questions that remain to be answered, such as the different growth rates of internal vs. surface cracks [23,24,36,37].

Although the role of defects in fatigue behavior has been explored and incorporated in modeling, a fundamental question remains unanswered, which is about reliably applying this knowledge to parts fabricated from a different AM platform. AM is undergoing continuous advancement, with established and new original equipment manufacturers (OEMs) contributing to technological advancement, while some companies are exiting the industry. In general, there exist significant differences in processing conditions (such as powder delivery mechanism, build chamber design, gas flow, scanning strategy, layer thickness, etc.) among different platforms by different OEMs, which can significantly influence the thermal history [6] and can affect the microstructure and defect content of the fabricated parts [38]. The optimal process parameters recommended by OEMs for a given material can vary significantly among different platforms, often to the extent that they are not transferable among the platforms due to differences in processing conditions. Hence, the fatigue behavior of the fabricated parts for each platform for a given material needs to be assessed before being adopted for critical load-bearing applications. However, the research programs require significant time and resources to complete, and the speed at which new OEMs and platforms emerge often outpaces research efforts focused on assessing the structural integrity of AM parts. Hence, a critical knowledge gap remains whether each platform should undergo the same extensive experimental campaign to establish defect-fatigue relationships or whether the test data and knowledge gained from one platform can be reliably applied to other platforms.

1.2. Project goal and objectives

The overall goal of this study is to understand the effects of the size, location, and morphology of the process-induced volumetric defects on the uniaxial fatigue behavior of the laser powder bed fused (L-PBF) Ti-6Al-4V. In addition, this study proposes a novel defect sensitive fatigue model capable of predicting fatigue life, incorporating defect size, location, and defect shape. Furthermore, the data generated in this study can help close the Gap FMP1 on "materials properties", which was established as a high priority by the AM standardization road map created by America Makes & ANSI Additive Manufacturing Standardization Collaborative [39]. Ti-6Al-4V, which constitutes more than half of the commercial applications of Ti alloys, was chosen because of its diverse applications in the aerospace, automotive, and biomedical sectors, credited to it's excellent strength-to-weight ratio and biocompatibility [40–42]. AM has been shown to be a suitable method for the fabrication of Ti-6Al-4V parts. The AM Ti-6Al-4V can be used for critical applications if the underlying effect of defect morphology on fatigue behavior can be revealed and incorporated in the development of material design allowables. This study aims to accomplish its goal by addressing several objectives. The objectives of this study are as follows:

1. Investigate the critical features of the volumetric defects (i.e., size, location, and shape) on the fatigue behavior of L-PBF Ti-6Al-4V.
   - **Hypothesis 1a:** Circular volumetric defects are more detrimental to fatigue behavior than the same sized irregular shaped defects.
   - **Hypothesis 1b:** Insufficient energy during fabrication is more detrimental than excessive energy to the fatigue resistance of AM specimens.
2. Estimate fatigue life and design curves using a fracture mechanics based semi-probabilistic approach incorporating defect morphology for L-PBF Ti-6Al-4V.
   - **Hypothesis 2a:** Crack growth behaviors of surface and internal defects are different, and they need to be treated differently for accurate fatigue life prediction.
   - **Hypothesis 2b:** Accounting for the transition of fatigue cracks from the interior to the surface, along with variations in short crack growth rates, leads to more accurate fatigue life predictions.
3. Investigate whether the defect-fatigue relationships established for L-PBF Ti-6Al-4V specimens on one platform can be reliably transferred to specimens fabricated on another platform.
   - **Hypothesis 3:** For a given material, the defect-fatigue relationships and predictive model developed based on data generated on one platform can be used to predict the fatigue behavior of specimens fabricated on another platform, provided that fatigue behavior is governed by the defects.

1.3. Outline of dissertation

This thesis is organized as follows: in Chapter 2, the most influential morphological features of process-induced volumetric defects on the fatigue behavior of L-PBF Ti-6Al-4V were identified. Fatigue test specimens were fabricated employing eight distinct sets of process parameters and three build orientations to induce a wide range of defect morphologies and populations. Force-controlled, fully-reversed, uniaxial fatigue tests were conducted on machined and polished specimens using servo-hydraulic test frames. Crack-initiating defects of all failed specimens were captured through fractography. The influence of these crack-initiating defects' features was analyzed by examining experimental data and finite element analysis. A new defect size parameter, $\sqrt{area}$ of the maximum inscribed circle (MIC), is proposed, which could account for the influence of both defect size and shape on the fatigue behavior.

In Chapter 3, the efficacy of a proposed fracture mechanics based model in predicting the fatigue life of L-PBF Ti-6Al-4V, incorporating the effect of volumetric defects' size and location, was evaluated. The effect of the volumetric defects' location on fatigue behavior was accounted for in modeling by utilizing a proposed crack propagation approach and incorporating the distinct crack growth constants for surface and internal defects. The fatigue design curves estimated using the largest defect size obtained from a probabilistic approach and the proposed crack growth model have been shown to be a better estimate compared to the design curves developed using the conventional fatigue qualification approaches.

In Chapter 4, the transferability of the defect-fatigue relationships of L-PBF Ti-6Al-4V specimens fabricated using two platforms, the EOS M290 and the Renishaw RenAM 500Q, was evaluated. Cylindrical L-PBF Ti-6Al-4V bars (which were machined to test specimens) were fabricated using a wide range of process parameters to induce volumetric defects of varying morphologies and populations. The defect-fatigue relationships established for the specimens fabricated on the EOS M290 platform were validated for those fabricated in the Renishaw RenAM 500Q platform through analytical analysis. In addition, the fatigue design curves, constructed using the short crack growth model with parameters derived from EOS M290 specimens and the largest surface defect sizes obtained from both RenAM 500Q specimens and the probabilistic approach, were compared against the fatigue lives of the RenAM 500Q specimens.

Finally, in Chapter 5, the objectives and hypotheses are revisited to directly connect the findings from the preceding chapters to the overall goal of understanding the effect of volumetric defects' features that are critical to the fatigue behavior of L-PBF Ti-6Al-4V. The outcomes corresponding to each objective are also presented.

1.4. Broader impact

The results of this study can support AM users in advancing damage-tolerant design of fatigue critical components through the application of defect sensitive fracture mechanics approaches. The defect sensitive fatigue modeling proposed herein can significantly reduce labor, cost, time, and energy associated with mechanical testing. Furthermore, the established relationships between defect characteristics and fatigue behavior of L-PBF Ti-6Al-4V can be leveraged to evaluate the fatigue strength and fatigue lives of parts without relying on extensive experimental programs. In addition, the proposed crack growth model can be coupled with non-destructive inspection techniques to develop a framework that can be used to accelerate the industrial adoption of AM technology. Finally, this study contributes valuable material property data, including fatigue and tensile data of L-PBF Ti-6Al-4V fabricated on EOS M290 and Renishaw RenAM 500Q platforms, which will be made accessible to the AM community for continued research and practical implementation.

2. Defect features critical to the fatigue of additively manufactured Ti-6Al-4V

2.1. Introduction

Additive manufacturing, AM, processes, such as laser powder bed fusion (L-PBF) tend to induce volumetric defects in the fabricated parts. In the surface machined condition, these defects can act as stress risers, leading to early crack initiation, especially in materials with finer microstructure such as Ti-6Al-4V [13,16,43–45]. This sensitivity of the material to volumetric defects becomes more pronounced in the high cycle fatigue regime, where crack initiation constitutes a major portion of the total fatigue life [14]. Any changes in the morphological features of the defects, such as their size and shape, which often result from perturbations in local processing conditions [8,16–18] and location [4,19], can influence the stress concentration and the crack initiation, affect fatigue life, and introduce significant scatter.

In the surface machined condition, the effects of critical volumetric defects' size [26,46–50] and location [20,22,51] on the fatigue behavior of materials are both well reported and can be somewhat accounted for using existing defect-sensitive fatigue models [15,20,26,46,50]. Regarding defects' size effect, in a given shape, a larger volumetric defect possesses broader stress concentration zones and can initiate fatigue cracks easier [20–22]. In addition, since the size of a crack initiated from a larger defect is effectively larger (i.e., it consists of those of the initiated crack and the defect itself), the crack experiences a much higher driving force for growth, which significantly reduces the growth life [52]. As a result, an inverse relation exists between the size of fatigue critical defects and the fatigue life or fatigue limit. Murakami et al. have treated volumetric defects as cracks, used the square root area of the convex hull enclosing defects' projection on the loading plane, √area, as crack size [26,47–49], and quantified defects' detrimental effects using the stress intensity factors (SIFs) of the equivalent crack [44,47].

Numerous works applying Murakami's model to various additively manufactured (AM) metallic materials have demonstrated its effectiveness in capturing the size effect, i.e., an inverse relationship exists between the size of the fatigue critical volumetric defects, $\sqrt{area}$, and the fatigue limit [20,53–55].

Regarding the effect of location, surface defects are typically more detrimental than internal ones because the less volumetric constraints near specimens' surfaces permit more plastic deformation and give rise to higher SIFs of cracks; as a result, cracks can both initiate and grow more easily [22–25]. To address this location effect, Murakami et al. differentiated surface defects from internal ones based on the defects' distance to the surface relative to the defect size along the distance's direction and assigned a coefficient to the SIF, which was greater for surface defects and smaller for internal ones [26]. Murakami's treatment of the location effect has also been shown to be adequate, often resulting in conservative fatigue life estimations [53,56,57]. Recent research has suggested that the detrimental effects of defects do not necessarily monotonically reduce when they move from surface to internal [20]. Rather, near-surface defects (i.e., the defect just below the surface but not exposed) can be more detrimental to the component's integrity than internal or surface-exposed defects of the same size. This is because the cracks may rapidly form in the highly stressed region between the free surface and the defect, resulting in a significantly larger surface-exposed defect [20]. Fatigue modeling efforts can somewhat account for this elevated criticality by incorporating a corrected, effective defect size corresponding to either a surface-connected convex hull [51] or a semi-ellipse [20] containing the near-surface defect. Nevertheless, this hypothesized defect-surface interaction mechanism still requires further experimental validation and clarification.

In contrast, the effect of volumetric defects' shape is more complex and less understood. Specifically, although literature generally acknowledges this effect, there has been a lack of consensus on the criticality of one defect shape relative to another and how this effect should be quantified [27,28]. Among three commonly observed types of volumetric defects, i.e., lack of fusions (LoFs), keyholes (KHs), and gas-entrapped pores (GEPs) [58,59], LoFs are generally thin, irregularly shaped, and contain sharp edges, in contrast to KHs and GEPs, which are near-spherical. On one hand, the higher stress concentration factors of LoFs, originating from their thin and sharp features, have been postulated to make them more prone to nucleate cracks and more detrimental to fatigue [60,61]. On the other hand, according to El Haddad [50], sharper notches are associated with steeper stress gradients, and the cracks initiated from such notches can experience an initial reduction in their effective SIF and have a higher likelihood of arrest. In other words, LoFs should be less detrimental than the near-spherical defects of the same size despite their higher stress concentration factors, which has been supported by recent studies examining the behavior of crack-bearing defects [20,21,62].

Given the inverse relationship between the size of the fatigue critical defect and fatigue resistance, the detrimental effects of volumetric defects are implicitly accounted for via their size. Aside from the Murakami's √area [26], literature has quantified the defects' size using elliptical envelopes, which consider an ellipse enclosing the defect's projection [23,63–65], and the actual areas, which consider the actual size of the defect instead of the size of a convex hull surrounding it [4,66–68]. The defect size measured using these approaches are similar for near-spherical defects; however, ambiguity arises for LoFs, with the Murakami's √area and the elliptical envelopes giving greater estimations than the defect's actual projected area, representing different degrees of criticality. In fact, Murakami has pointed out that the correction in √area parameter is necessary when the defect shapes become highly irregular, as the √area parameter was originally developed for casting defects and inclusions, which are of more regular shapes [26,69,70].

This work explicitly examines the critical features of volumetric defects (i.e., the ones that describe the defect's size, location, and shape) on the fatigue behavior of L-PBF Ti-6Al-4V specimens. Ti-6Al-4V was chosen because of its popularity in key engineering sectors and its fatigue behavior's relatively high and consistent sensitivity to volumetric defects owing to its fine and homogeneous microstructure [3,71–74]. Variations in the defect's features were achieved by altering the process parameters used during fabrication. Uniaxial, fully-reversed, force-controlled fatigue tests were performed at different stress amplitudes. Fractography and numerical simulations were used to further examine the role of defect features, especially regarding the defects' shape, on fatigue behavior. Accordingly, a new effective defect size parameter was proposed.

This article is arranged as follows: Section 2.2 briefly describes the experimental procedures followed for fabrication, mechanical testing, and numerical simulations; Section 2.3 presents the experimental results examining the influence of defect size, location, and shape on fatigue behavior; finally, conclusions are presented in Section 2.4.

2.2. Experimental and numerical procedures

2.2.1. Material and fabrication

Ti-6Al-4V cylindrical rods were fabricated using the L-PBF technique employing an EOS M290 machine with a total of eight sets of process parameters and in three part orientations. The build layouts of Ti-6Al-4V cylindrical rods fabricated in this study are shown in Figure A6-1. Plasma-atomized Ti-6Al-4V Grade 5 powder was used for the fabrication of the rods, whose chemical composition provided by the supplier, AP&C, is listed in Table 2-1. Typically, over supply of energy during fabrication of AM parts leads to formation of KHs, while an energy deficit results in LoFs [16,58]. Among the eight sets of process parameters used to fabricate the rods in this study, one set was the manufacturer recommended (R) (listed in Table 2-2); five sets were adjusted in laser power, P, and hatch spacing, h, to induce the condition of underheating (U) during fabrication favoring the formation of LoFs (see the Ua through Ue conditions listed in Table 2-3); the remaining two sets induced overheating (O), favoring the formation of KHs (see the Oa and Ob conditions listed in Table 2-3). The U and R sets were fabricated in vertical (V), diagonal (D), and horizontal (H) orientations since LoFs are typically relatively flat with their longest direction being perpendicular to the build direction and expected to cause mechanical anisotropy. On the other hand, the O sets, inducing mostly KH, were fabricated only in V orientation since KHs are spherical and expected not to exhibit much directionality. The percent change of process parameters and energy density values, along with the orientations of parts fabricated for each processing condition, are included in Table 2-3. Each combination of processing condition and part orientation shown in Table 2-3 constitutes a specimen set, and for each specimen set, a total of 15 rods were fabricated for fatigue testing and 6 for tensile testing.

Before removing the fabricated rods from the build plate, they were stress-relieved together with the build plate in an electric muffle furnace at 704°C for 1 hour with a heating rate of 5°C/minute, and then furnace cooled to room temperature [75,76]. Following stress-relieving, the Ti-6Al-4V rods were detached from the build plate, machined, and polished to tensile and fatigue specimen geometries following ASTM E08 [77] and ASTM E466 [78] standards, respectively. The geometry and dimensions of the tensile and fatigue specimens used in this study are included in Figure A6-2.

Table 2-1. Chemical composition of powder supplied by AP&C used for the fabrication of L-PBF Ti-6Al-4V specimens, as reported by the supplier.

Element	Wt%
Ti	Balance
Al	6.260
V	3.910
Fe	0.210
O	0.140
C	0.010
N	0.010
H	0.002

Table 2-2. The manufacturer recommended process parameters for the fabrication of L-PBF Ti-6Al-4V specimens on an EOS M290 machine.

Laser power, P	280 W
Scanning velocity, v	1200 mm/sec
Layer thickness, t	30 μm
Hatch spacing, h	140 μm
Layer rotation	67°
Stripe width	10 mm

Table 2-3. Process parameter variations and part orientations used for fabricating tensile and fatigue L-PBF Ti-6Al-4V specimens.

Designation of processing condition	Variation in process parameters from manufacturer recommended values (%)			Energy density $E = \frac{P}{vht}$ (J/mm^3)	Orientation of parts fabricated
	P	v	h		
Ua	-20	0	0	44.44	V, D, H
Ub	0	0	20	46.29	V, D, H
Uc	-10	0	0	50.00	V, D, H
Ud	-5	0	0	52.77	V, D, H
Ue	0	0	5	52.91	V, D, H
R	0	0	0	55.55	V, D, H
Oa	30	-20	0	90.28	V
Ob	20	-30	0	95.24	V

2.2.2. Micro/-defect characterization

Microstructural analysis was conducted on the samples excised from the gage section of the machined fatigue specimens in the longitudinal plane (i.e., the plane parallel to the axis of the specimens). The samples were mounted in epoxy resin, ground, and polished to a mirror finish using SiC papers of decreasing grits and 0.05 μm colloidal silica, in accordance with ASTM E3 standard [79]. Back-scattered electron, BSE, images of the polished surfaces were obtained using the electron channeling contrast imaging technique utilizing a Zeiss Crossbeam 550 scanning electron microscope, SEM, employing a 10 kV voltage [80]. As shown in the BSE images in Figure A6-3, the microstructure of L-PBF Ti-6Al-4V specimens was fine lamellar and did not show clear dependence on the process parameters used for fabrication.

Three-dimensional (3D) characterization of volumetric defects for each processing condition was performed via X-ray computed tomography (XCT) scans on the entire gage section of one machined fatigue specimen per processing condition using a Zeiss Xradia 620 Versa system. Following the XCT scans, the 3D reconstructions of the projected XCT images were performed using the Zeiss proprietary software. The defect populations in specimens fabricated with various process parameters, intended to induce different levels of porosity and volumetric defect morphologies, are shown in Figure 2-1. Along with the energy density (E) used for fabrication, relative density, $\rho_{relative}$, of the specimens and the square root of the projected area of the largest defect in the plane perpendicular to the axial direction of the specimens are also included Figure 2-1. In addition, some defect statistics, including defect count per volume, maximum axis of the fitted ellipse of the largest defect, and 90th percentile defect size for each specimen, are shown in Figure 2-2.

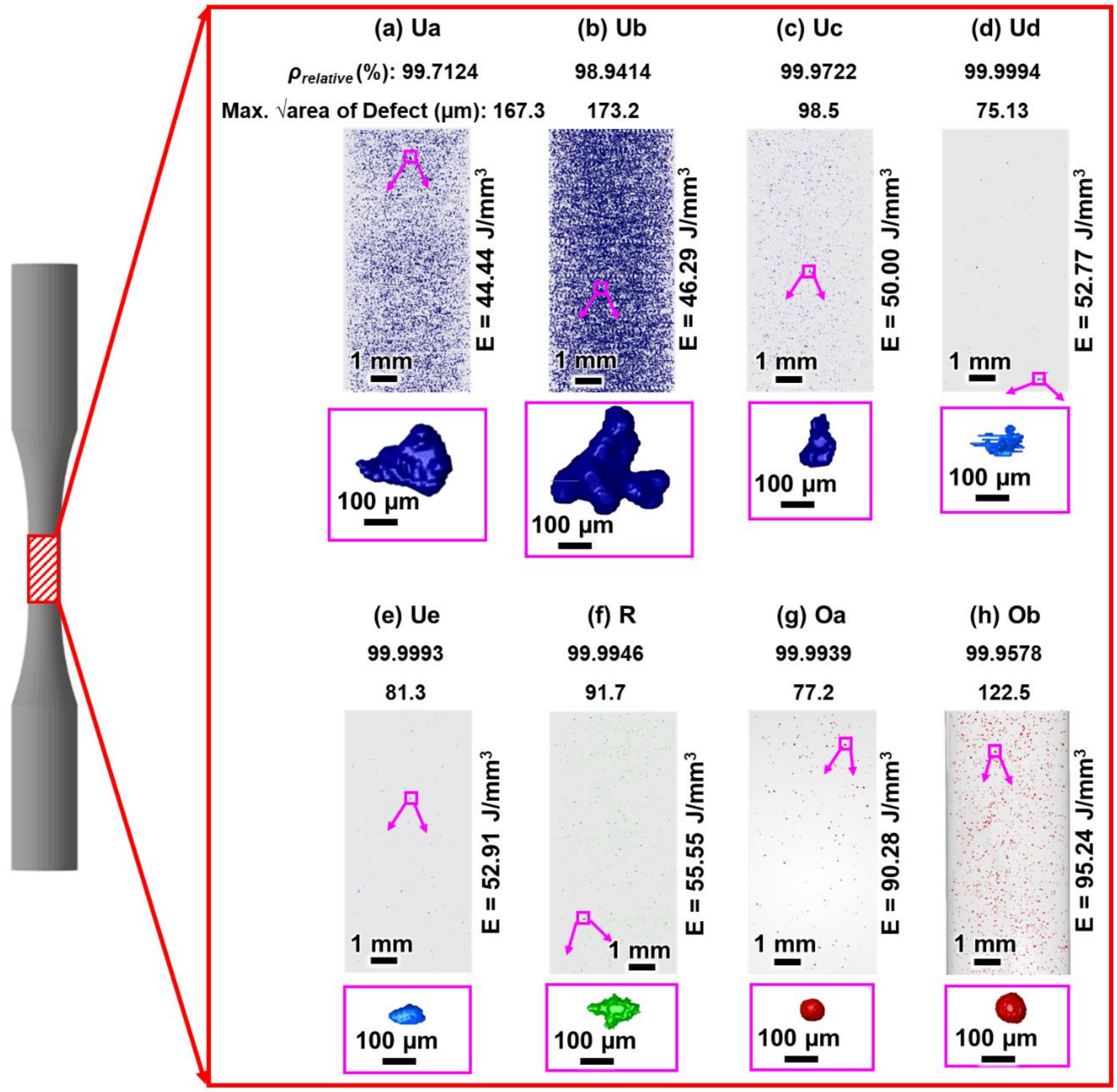

Figure 2-1.Visualization of volumetric defects within the entire gage volume of selected vertically oriented specimens, obtained using XCT. For each specimen, the largest defect was isolated and shown in insets. The maximum √area represents the square root of the projected area of the largest defect in a plane perpendicular to the axial direction of the specimen.

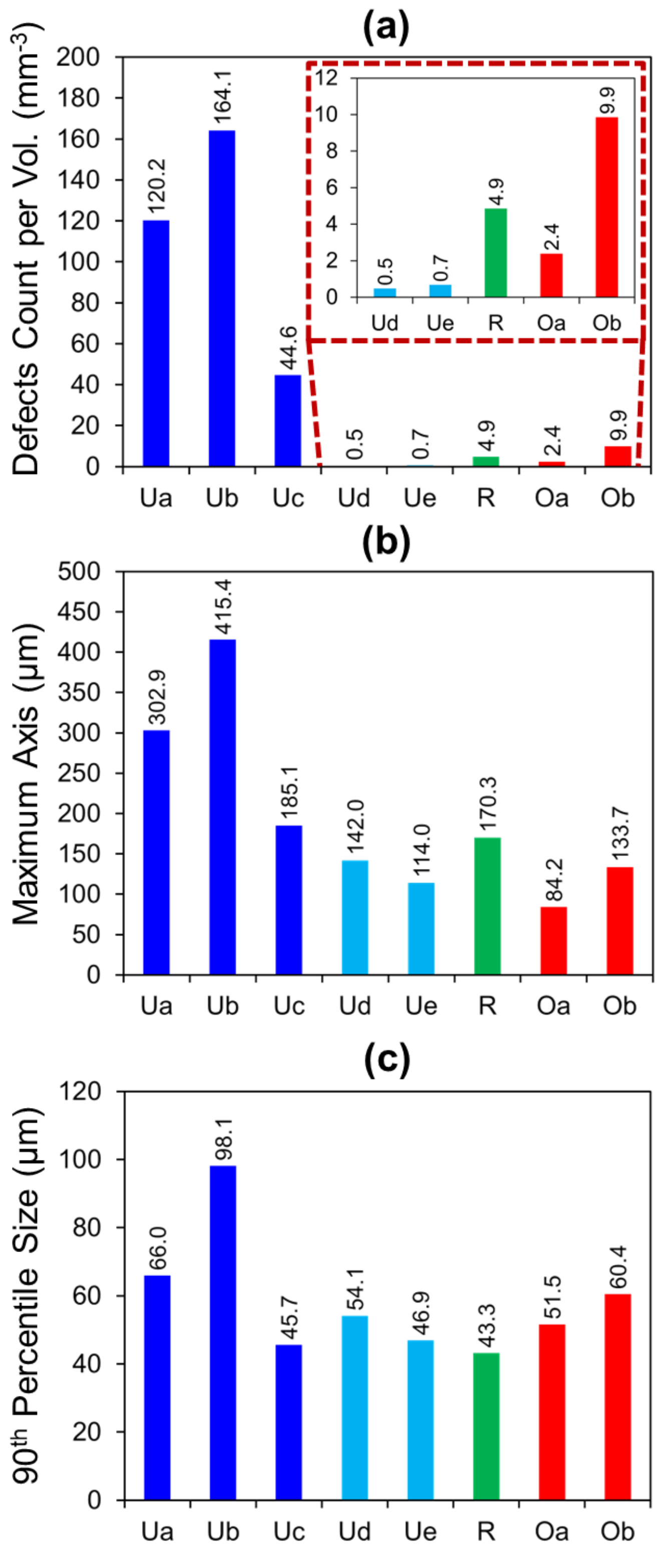

Figure 2-2. Column charts of defect statistics of L-PBF Ti-6Al-4V specimens fabricated using different process parameters: (a) defect count per volume, (b) maximum axis, and (c) 90th percentile size.

The U specimen fabricated by increasing hatch spacing by 20% (i.e., Ub) exhibited the highest defect count per volume and the largest defect size (both maximum axis and 90th percentile size). The U specimens fabricated with energy densities comparable to the R specimen (i.e., Ud and Ue) displayed comparable maximum axis and 90th percentile defect size to those in the R. Closer examination of the larger defects in the Ud, Ue, and R specimens revealed them to be LoFs (see Figure 2-1); the limited process variation of Ud and Ue from R likely did not result in significant changes in the size of these defects. Interestingly, these defect measures, $\sqrt{}$area of the projected area of the largest defect on the plane perpendicular to the axial direction of the specimen, the maximum axis, and 90th percentile defect size of the Ud, Ue, and R specimens were also comparable with those of both O specimens, although the larger defects in O specimens were KHs (see Figure 2-1 and Figure 2-2).

2.2.3. Mechanical testing

Tensile behavior of all specimen sets was examined using quasi-static tensile tests conducted at room temperature using MTS servo-hydraulic test frames according to ASTM E8 standard [77]. The tests were conducted in displacement control mode while maintaining a nominal strain rate of 0.001 mm/mm/sec. Strain experienced by the specimens until the final fracture was captured using a mechanical extensometer. The total elongation at failure was measured by comparing the final and initial lengths between markings on the gage of the specimens. At least five tensile tests were conducted per set to ensure repeatability.

Room temperature fatigue tests were conducted in uniaxial, force-controlled, and fully-reversed (R_{σ}= -1) mode using servo-hydraulic test frames according to ASTM E466 standard [78]. Fatigue tests were initially performed at stress amplitudes, σ_a, of 450, 500, and 600 MPa, and at least 4 specimens per stress amplitude per set were tested (except for the run-outs) to ensure repeatability. The tests which did not fail by 10,000,000 cycles were treated as run-outs. If, for a specific stress level and specimen set, run-outs occurred at least twice and no specimen failure were observed, the stress level was designated as the run-out level for that particular specimen set and no additional tests were performed. Following the completion of fatigue tests at the aforementioned σ_a (i.e., 450, 500, and 600 MPa), additional fatigue testing of the remaining specimens was conducted at 400 MPa to generate more fatigue data. A total of 232 specimens were tested. Fractography was conducted on all failed fatigue specimens to obtain the crack-initiating defect's size and their morphological features using SEM.

2.2.4. Numerical analysis procedure

The SIF of planar cracks, whose shapes were identical to the two-dimensional (2D) morphology of selected few fatigue critical defects obtained from the fracture surfaces, were calculated via linear elastic finite element analysis. For the calculations, an internal crack configuration, where a crack was embedded in a large, cubic body, was modeled in Ansys Workbench. The loads and fixed boundary conditions were applied on the opposite faces of the cubic body on planes parallel to the crack. Ten-node tetrahedral elements were used to mesh the crack contour region and the remaining portion of the cubic body (see Figure A6-8 in Appendix A). Initially, a mesh convergence study was performed using an embedded penny crack for which the SIF values were known, and the same element sizes were used to mesh the cracks whose geometries were modeled after the 2D shapes of fatigue critical defects. Mode I SIFs along the crack front of the cracks were estimated using the contour integral approach implemented in Ansys Workbench.

2.3. Experimental results and discussion

2.3.1. Tensile behavior

The yield strength, S_y, ultimate tensile strength, S_u, and percent elongation to failure, %El, of L-PBF Ti-6Al-4V specimens fabricated using different process parameters in different part orientations are presented in Figure 2-3. As shown in Figure 2-3 (a), the tensile properties of the specimens do not appear to correlate with its defects content. Notably, although the Ub condition induced a substantially higher defect count (Figure 2-2 (a)) and relatively low part density (see Figure 2-1) than others, neither strengths nor %El were negatively impacted. However, the O specimens (i.e., sets Oa and Ob) demonstrated slightly improved tensile strengths (both S_y and S_u). On average, the O specimens exhibited slightly higher S_y (~ 40 MPa) and S_u (~ 40 MPa) than the R specimens.

The marginal improvement in the tensile strengths for the O specimens compared to the R and U ones could be due to the slightly higher levels of interstitial oxygen and/or nitrogen [81,82]. Chemical analysis was performed on selected L-PBF Ti-6Al-4V specimens fabricated using different process parameters to examine it further, and the results are shown in Figure A6-4 in the Appendix A. While the oxygen and nitrogen concentrations were within the limits recommended by ASTM F2924-14 standard [83] for all specimens, the Ob specimen exhibited slightly higher levels of both elements, and the Oa specimen demonstrated a marginally higher level of oxygen content compared to the R specimen. The higher energy density used during the fabrication of the O specimens likely facilitated the dissolution of more interstitial oxygen and nitrogen within the α-laths in Ti-6Al-4V [81,82]. These interstitial elements might have enhanced the tensile strengths by impeding the dislocation motion [81,82].

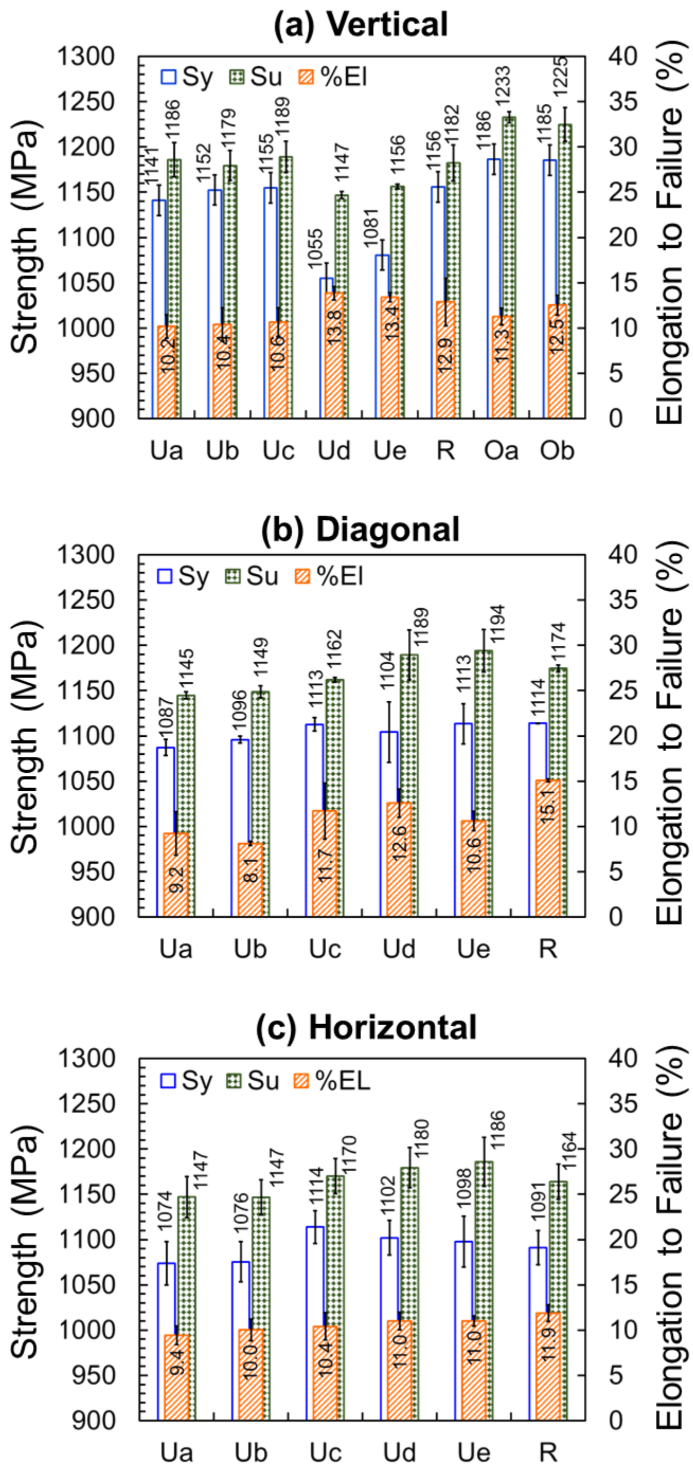

Figure 2-3. Column charts of tensile properties of L-PBF Ti-6Al-4V specimens fabricated using different process parameters for (a) V, (b) D, and (c) H orientations.

Tensile fracture surfaces of specimens fabricated using different process parameters, as shown in Figure A6-5 for selected ones, reveal that differences in volumetric defect content among the specimens did not significantly affect the fracture behavior. All tensile fracture surfaces exhibited similar fracture features, including dimples and shear lips, which are characteristics of ductile fracture.

2.3.2. Fatigue behavior

The stress-life fatigue plots showing σ_a vs. reversals to failure, $2N_f$, of L-PBF Ti-6Al-4V specimens fabricated using different process parameters and part orientations are shown in Figure 2-4. The run-out specimens were indicated by arrows. Overall, the adjustment in processing conditions was effective in resulting in a relatively large variation in fatigue life.

Among V specimens, excluding the O ones (Figure 2-4 (a)), the ordering in fatigue life among different specimen sets appeared to be consistent with the maximum axis and $\sqrt{area}$ of the largest defects (always LoFs, as shown in Figure 2-1) on the plane perpendicular to the axis of the specimen measured from the XCT scans for different processing conditions (see Figure 2-1 and Figure 2-2). Specifically, the XCT scans revealed that the larger defects in Ua and Ub specimens well corresponded to the overall shorter fatigue lives of the Ua V and Ub V specimen sets. In addition, Ud and Ue specimens exhibited the smallest $\sqrt{area}$ values for the largest defects, which explained their longest fatigue lives. The trends observed among the U and R specimen sets in the V orientation were qualitatively similar to those in the D and H orientations. The agreement between fatigue life and the value of the $\sqrt{area}$ of the largest defect among the U and R specimen sets was not always the case for the Oa and Ob specimen sets. For example, like the U and R specimens, the largest defect of Oa specimen having a smaller $\sqrt{area}$ value than Ob corresponded to Oa sets' longer fatigue lives. However, although the $\sqrt{area}$ value for the largest defect of Oa specimen was noticeably smaller than that of the Ud and Ue specimens, the fatigue lives measured for the Oa specimen set were always shorter. This discrepancy could have originated from the largest defects in the O specimens being KHs (Figure 2-1), which present a different extent of detrimental effects to fatigue than the LoFs.

Fractography performed on all failed fatigue specimens confirmed that all but one fatigue crack initiated from GEPs, KHs, or LoFs in all specimens. The only failure that did not initiate from these defect types was one instance within the Ud set, where graphite particles were found at the crack initiation site. In addition, the fatigue critical defects (i.e., the defects responsible for the initiation of fatigue failure) of the U and R specimens sets were mostly LoFs and those for the O sets were all KHs, which was consistent with the types of the largest defect detected for each processing condition via XCT. Selected fractography images for specimens fabricated using different process parameters are shown in Figure 2-5. For U specimens, except for Ud and Ue, all fatigue cracks initiated from LoFs located either on the surface/near-surface or internal region (the classification of defects based on location following the approach of Wu et al. [64], which will be formally discussed in Section 2.3.3.1, see Figure 2-7 (a)). In contrast, fatigue cracks in Ud and Ue specimens predominantly initiated from internal LoFs, with rare occurrences of crack initiations from GEPs/KHs defects. For the R specimens, all fatigue cracks were initiated from LoFs located either on the surface/near-surface or internal region. In the O specimens, all fatigue cracks were initiated from KHs, with only four located at the near-surface, while the rest were internal. In most cases, fatigue cracks were initiated from a single defect (~72%). The majority of the specimens that experienced fatigue crack initiation from multiple defects were from sets with higher defect content (i.e., Ua, Ub, and Uc).

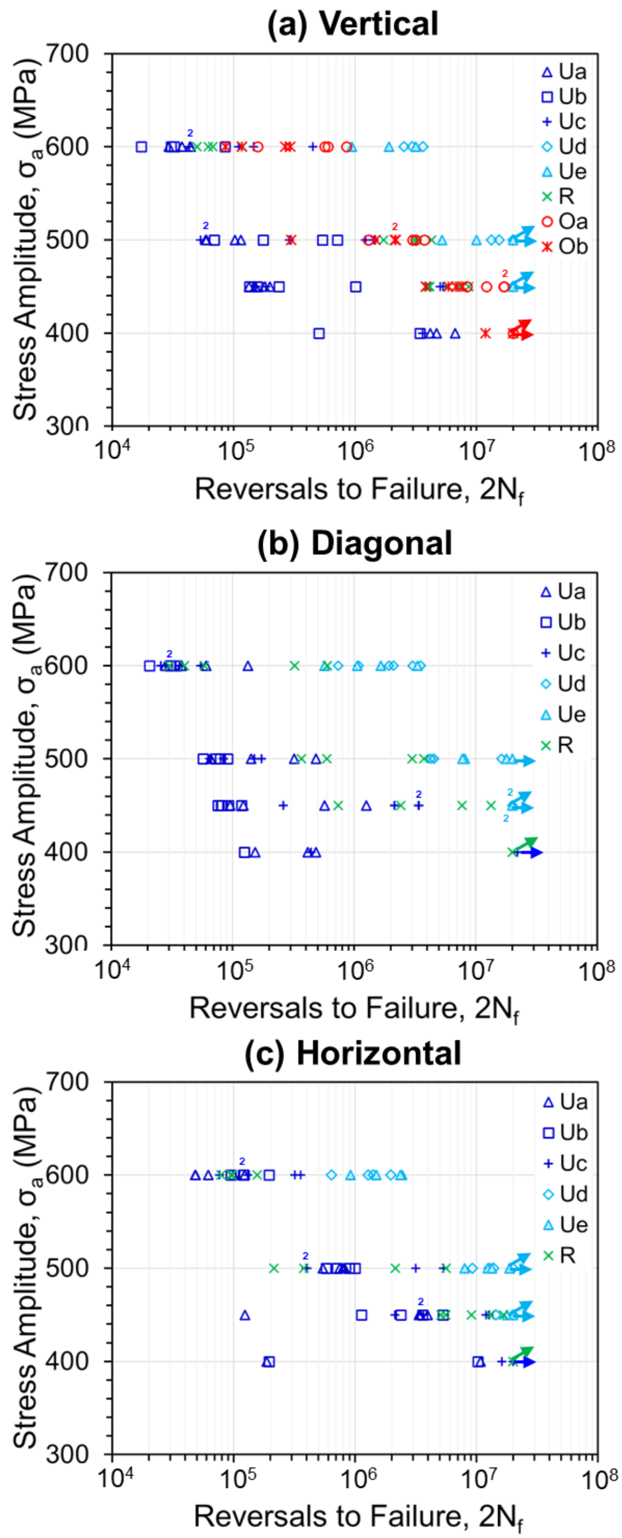

Figure 2-4. Stress-life fatigue plots of L-PBF Ti-6Al-4V specimens fabricated using different process parameters in (a) V, (b) D, and (c) H orientation. The run-out tests are indicated with arrows.

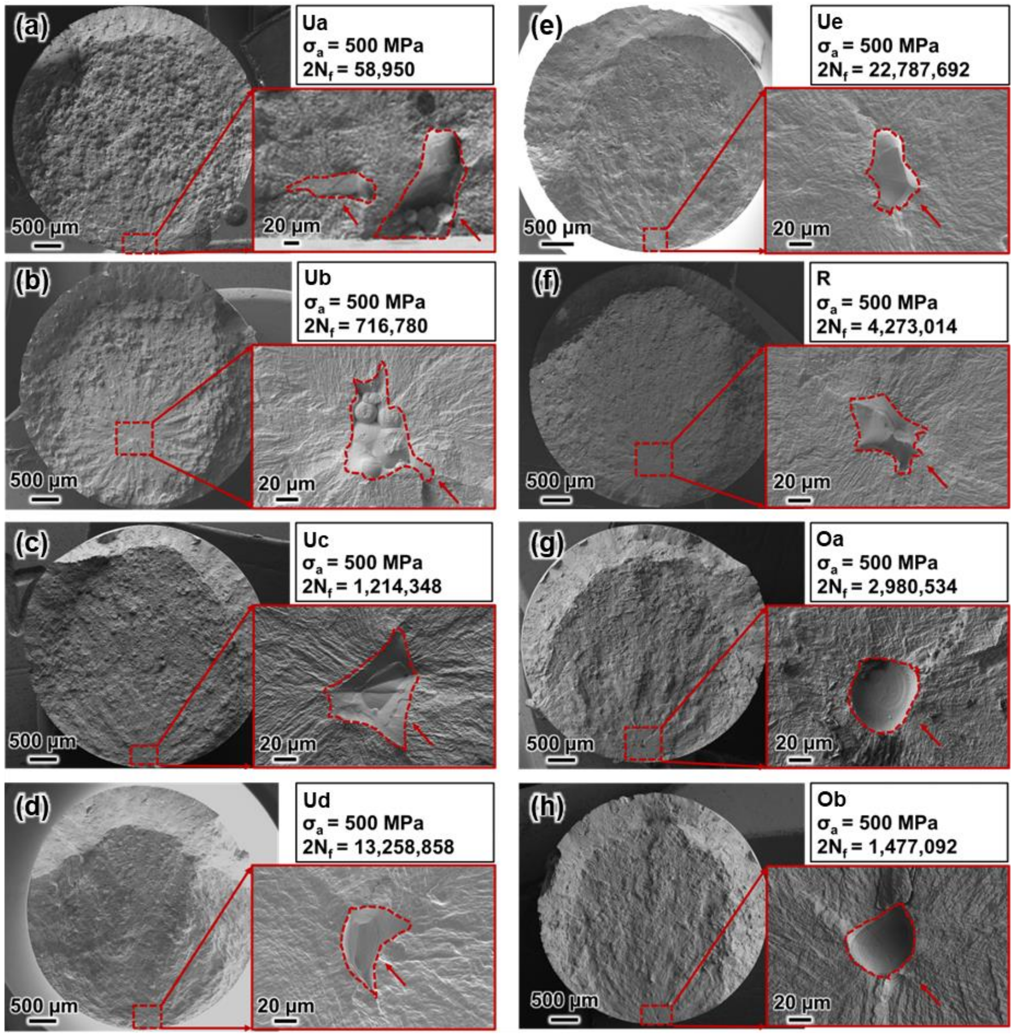

Figure 2-5. Fracture surfaces of selected L-PBF Ti-6Al-4V specimens fabricated using different process parameters. Crack-initiating defects are indicated by red arrows and their $area_{Actual}$ are enveloped with red-dashed lines

2.3.3. Criticality of defect features on the fatigue behavior

2.3.3.1. Effect of size and location of defects on the fatigue behavior

Stress-life bubble plots, in which the size of the markers is proportional to the size of the crack-initiating defects, are shown in Figure 2-6. For each fatigue critical defect, the square root area of both its actual projection in the loading plane and the convex hull construct around its projection was measured as its size (the construction of the convex hull followed Murakami's approach [26], see Section 6.1.6 of the Appendix A for details). These are respectively referred to as $\sqrt{area}_{Actual}$ and $\sqrt{area}_{Murakami}$ in this manuscript. Crack-initiating defects whose shape appeared irregular (i.e., LoF) and circular (i.e., GEP/KH) are plotted in blue and red shades, respectively. As expected, the measured values of $\sqrt{area}_{Murakami}$ were larger than the $\sqrt{area}_{Actual}$, particularly for irregularly shaped defects. As shown in Figure 2-6, although a general trend of larger crack-initiating defects leading to shorter fatigue lives appears to exist, the obscuring presence of outlier suggests that size alone clearly cannot fully explain the observed variations in fatigue lives.

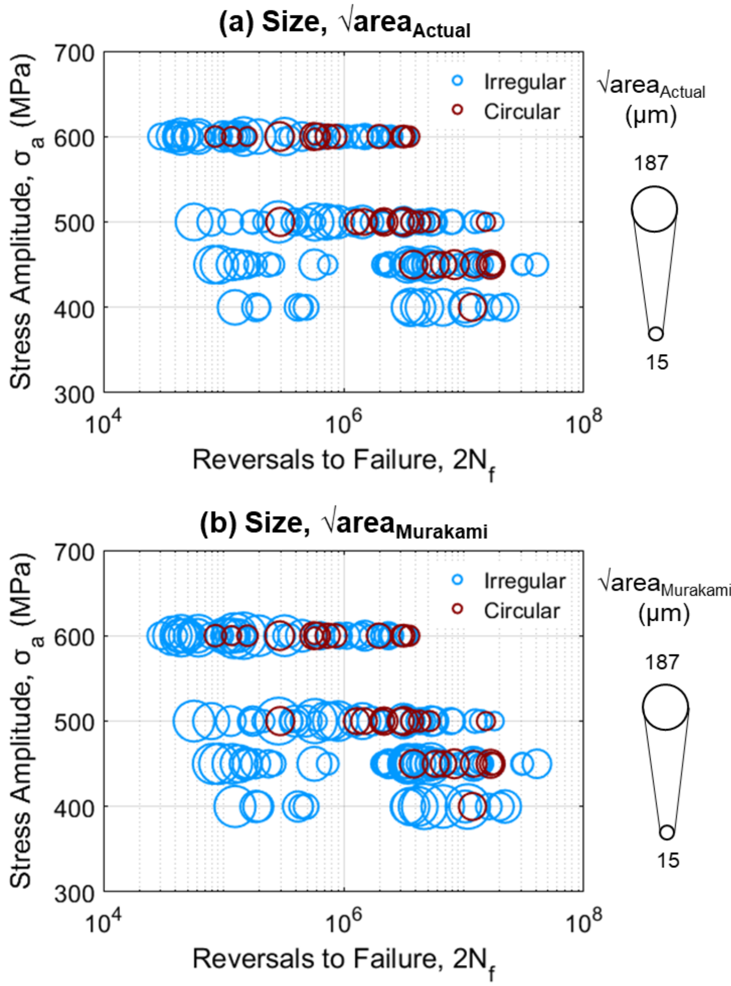

Figure 2-6. Stress-life fatigue plots for all L-PBF Ti-6Al-4V specimens with bubble size representing the crack-initiating defect size measured by: (a) $\sqrt{area_{Actual}}$ and (b) $\sqrt{area_{Murakami}}$. The scale bar for bubble size is shown on the right side of each plot.

To examine the effect of defect location that can synergistically influence the fatigue behavior with defect size, the defects were categorized as either surface or internal ones based on their distance from the surface following the approach by Wu et al. [64] (as shown in Figure 2-7 (a)). Defects were classified as "surface defects" if: (i) they were surface-exposed (i.e., distance from the free surface to the nearest point of the defect, e = 0) or (ii) they were located near-surface where $\sqrt{area_{eff}}$ (i.e., the square root area enveloping the defect and free surface, denoted with red dashed lines in Figure 2-7 (a)) ≥ e. Internal defects are the ones where $\sqrt{area_{eff}} \leq$ e. Stress-life bubble plots displaying the distance of crack-initiating defects from the specimen surface and the $\sqrt{area}_{Murakami}$ of crack-initiating defects at different location categories are shown in Figure 2-7 (b)-(c) and Figure 2-7 (d)-(f), respectively, for all specimens with crack-initiating from a single defect. Since surface-exposed defects (i.e., e = 0) have no distance from the surface, only near-surface defects (i.e., $\sqrt{area}_{eff} \geq e$) were considered for assessing the effect of distance from the surface among the surface defects. This defect classification approach proposed by Wu et al. [64], adapted from Murakami's approach [26,48], classifies more defects close to the free surface as surface defects compared to the original Murakami's approach, thus making it more conservative.

When the near-surface and internal defects were considered separately (see Figure 2-7 (b) and (c)), no clear dependence of fatigue life on the distance of the defect from the free surface was observed. This indicated that the criticality of the defect on the fatigue behavior was not solely dependent on the distance from the free surface. Instead, defects' location (i.e., surface, near-surface, or internal) may augment or diminish the effect of defects' other attributes such as size and shape. This is evident by examining the size effect after categorizing crack-initiating defects by location (i.e., surface-exposed vs. near-surface vs. internal, see Figure 2-7 (d)-(f)). For near-surface (Figure 2-7 (e)) and internal defects (Figure 2-7 (f)), the trend of larger defects being more detrimental became clearer. Comparing Figure 2-7 (d)-(f), although the defect sizes in all three location categories fall within the same range, the overall fatigue lives for near-surface critical defects appear to be the shortest, followed by surface defects and internal ones in order. In other words, defects tended to be more detrimental when they were near-surface, not surface-exposed.

Such a non-monotonic variation in defect criticality as a function of depth can, on the one hand, be ascribed to the highly stressed zone between specimen surfaces and near-surface defects tending to form cracks easier, resulting in significantly larger, surface-exposed cracks [13],. On the other hand, this may also be credited to the compressive residual stresses induced by surface machining. This stress, existing down to a depth of ~50 μm (see Figure A6-7), may have partially alleviated the stress concentrations near the surface-exposed and near-surface defects, retarding fatigue crack initiation. The compressive residual stress near the surface may have also influenced the size effect as perceived from Figure 2-7 (d) and (f). Indeed, compared to internal critical defects (Figure 2-7 (f)), the size effect exhibited by the near-surface defects was less pronounced (Figure 2-7 (e)). For surface-exposed defects (Figure 2-7 (d)), the size effect was virtually non-existent. Due to the finite depth of the compressive residual stress (~50 μm), portions of many surface-exposed defects (whose $\sqrt{area}_{Murakami}$ were well over 50 μm) resided outside its influence and experienced minimal retarding effects on crack initiation, potentially disrupting the typical size effect. Similar disruption was expected for some near-surface defects, in which case regions of defects located further inside experienced higher stress concentration than those between the defect and the free surface, where accelerated crack initiation was expected.

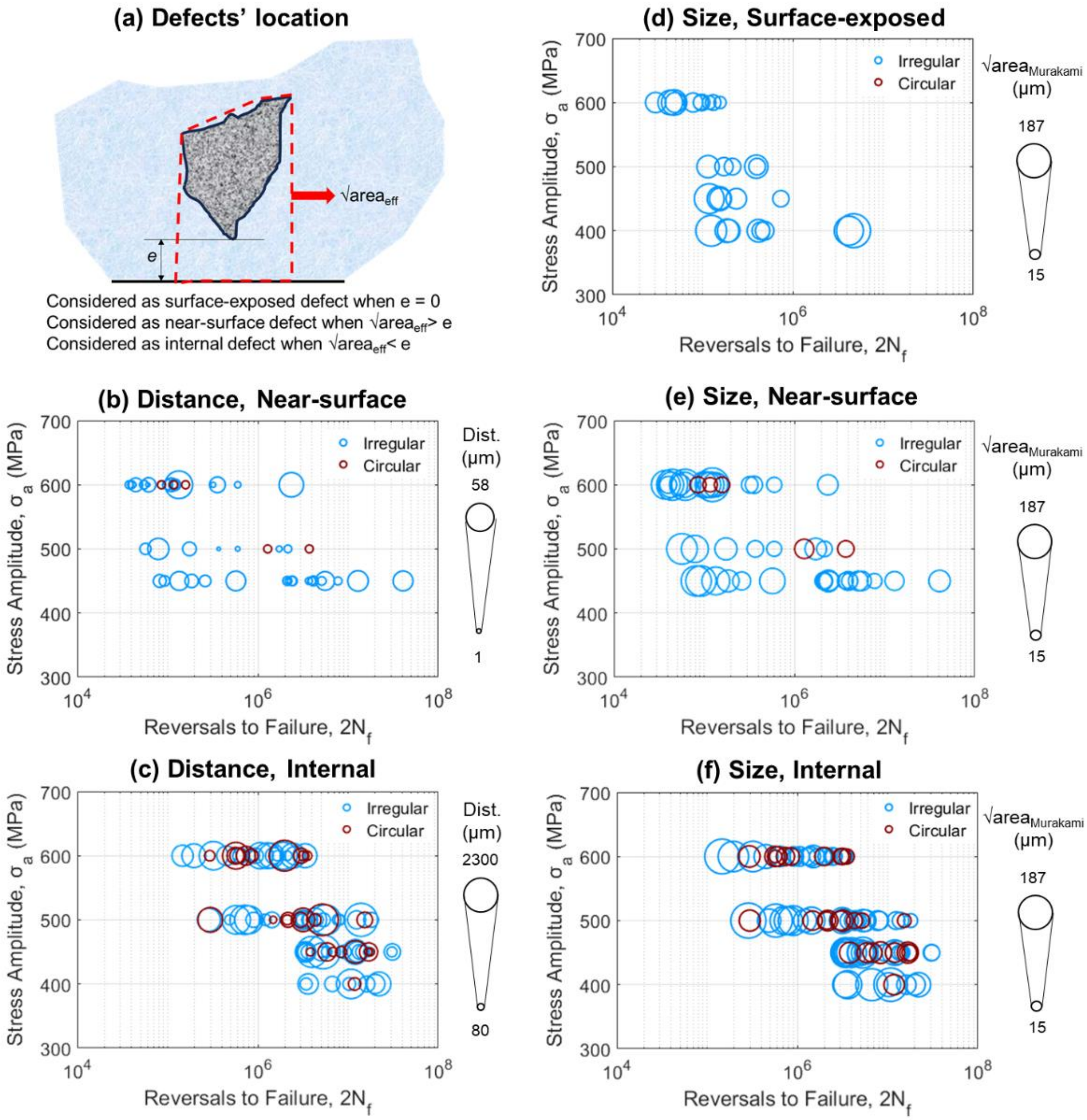

Figure 2-7. (a) Criteria used for classifying defects into surface-exposed, near-surface, and internal defects. Stress-life fatigue plots showing with bubble size representing the distance of crack-initiating defects from the specimen surface for (b) near-surface and (c) internal defects, and crack-initiating defect size for (d) surface-exposed, (e) near-surface, and (f) internal defects. The scale bar of bubbles is shown on the right side of each plot.

For internal defects, where the size effect was the most prominent, discrepancies were still observed in the defect size between irregular and circular defects. Despite similar fatigue lives (see Figure 2-7 (f)), the size of irregular defects appears to be larger than the circular ones, suggesting that they may be less detrimental or their size might have been overestimated. This discrepancy highlights a potential limitation in size measurement methods via the simple construction of convex hulls, which were developed primarily for more regularly shaped defects in conventional manufactured parts such as casting [26,48]. These methods might not be suitable for irregularly shaped AM defects, especially when the defect geometry is highly irregular or jagged. The impact of defect shape on fatigue behavior will be discussed further in Section 2.3.3.2.

2.3.3.2. Effect of shape of the defects on the fatigue behavior

A comparison of circular and irregular defects with similar fatigue lives from near-surface and internal location showed that the size of circular defects was smaller than the irregular ones, when measured by $\sqrt{area}_{Murakami}$, as shown in Figure 2-7 (e) and (f). This suggests that, regardless of their location, defect shape plays a critical role in fatigue behavior. Since no circular defects were observed among surface-exposed defects, surface-exposed defects were excluded from the analysis of the effect of defect shape on fatigue behavior. A popular shape descriptor, circularity, was computed for the fatigue critical defects from the fractographs to examine any potential dependence of fatigue life on defect shape. The circularity was calculated using ImageJ software as follows [84]:

$$Circularity = \frac{4\pi \times \sqrt{area_{Actual}}}{Perimeter^2} \tag{2.1}$$

where perimeter is the length of the outside boundary of the selection of $area_{Actual}$.

The stress-life data in Figure 2-7 (d)-(f) are replotted in Figure 2-8, with the marker size now representing the circularity of the crack-initiating defects. However, just as revealed for the distance effect in Figure 2-7 (b) and (c), circularity does not present a strong and clear influence on fatigue life. It was therefore suspected that, again, like the location effect, the effect of defect shape may manifest by augmenting or diminishing defects' size effect. To explore this further, three pairs of internal, fatigue critical defects are presented in Figure 2-9 (a)-(b), (c)-(d), and (e)-(f). Internal defects were selected to exclude any potential influence from the specimen's free surface. Within each pair, the corresponding fatigue lives were similar, but defect shapes varied from irregular to near-circular, and the measured $\sqrt{area_{Actual}}$ also differed significantly. The differences underscored the influence of defect shape on fatigue behavior.

Linear elastic finite element analyses were performed to calculate the SIF of planar cracks whose shapes were extracted from the 2D profiles of the defects on the fractographs, following the methodology outlined in Section 2.2.4. The distribution of normalized SIF along the crack fronts is presented in Figure 2-9 (g)-(l). The normalization was calculated as:

$$\text{Normalized SIF} = \frac{SIF}{0.5 \times \sigma_a \sqrt{\pi \sqrt{area_{Murakami}}}} \tag{2.2}$$

where $0.5 \times \sigma_a \sqrt{\pi \sqrt{area_{Murakami}}}$ was the SIF calculated according to Murakami et al. [26] for internal defects. For near-circular cracks, the entire crack front experienced relatively uniform SIF values close to the maximum. In contrast, for irregular cracks, only a small fraction of the crack front experienced SIF values near the maximum, particularly at the concave contours near the interior region, as shown in Figure 2-9 (g)-(l). In fact, the maximum values of SIF appeared to occur at locations where the crack contours connected with their maximum inscribed circles, MIC (see the blue dashed lines in Figure 2-9 (a)-(f)). Similar trends were observed in several other crack shapes examined in this study (see Figure A6-9), highlighting the significance of the interior region in crack initiation. The higher SIF in the interior regions of the modeled planar cracks suggested that the fatigue cracks were more likely to initiate from the interior of the irregular defects. Indeed, in-situ studies examining the crack initiation from defects have revealed that, for irregular defects, cracks typically initiate from the interior region and require a significant number of cycles before forming a convex hull shape [22].

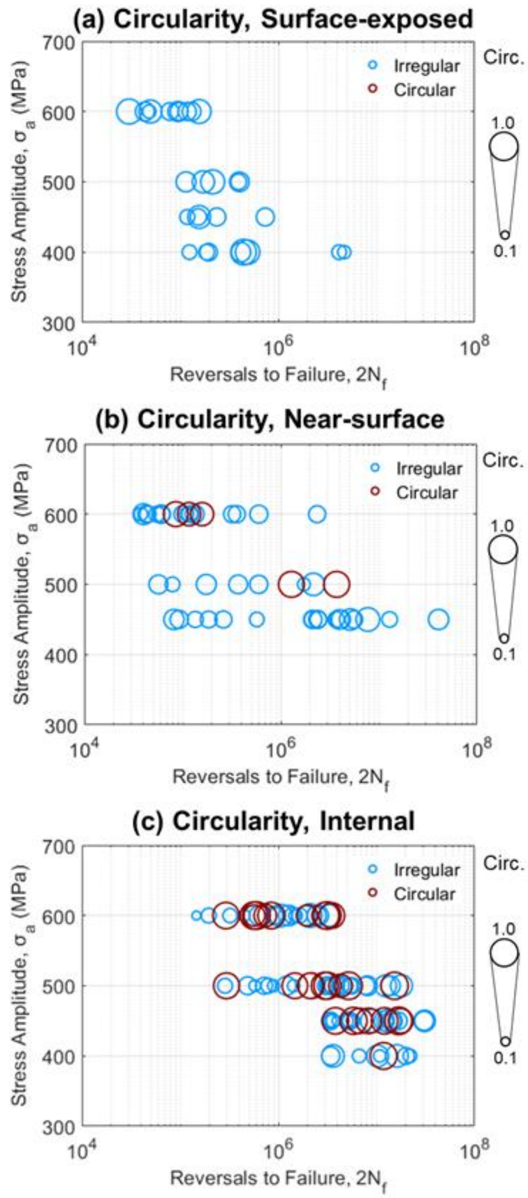

Figure 2-8. Stress-life fatigue plots for L-PBF Ti-6Al-4V specimens with bubble size representing the circularity of crack-initiating defect for (a) surface-exposed, (b) near-surface, and (c) internal defects. The scale bar of bubbles is shown on the right side of each plot.

The normalized SIFs along the crack front are presented again with respect to the distance along the crack front in Figure 2-9 (m)-(r). The magenta lines in the figure represent the SIF calculated based on $\sqrt{}area_{Murakami}$ of the cracks/defects according to Murakami et al. [26]. As shown in Figure 2-9 (m), (o), and (q), for irregularly shaped cracks, only small fractions (<5%) of the crack front experienced SIFs exceeding the values estimated by defect-sensitive models using the $\sqrt{}area_{Murakami}$ parameter (such as Murakami's model where maximum $SIF = 0.65 \times \sigma_a\sqrt{\pi\sqrt{area_{Murakami}}}$ for surface defects and maximum $SIF = 0.5 \times \sigma_a\sqrt{\pi\sqrt{area_{Murakami}}}$ for internal defects [26]). In contrast, for circular defects, a substantial portion (> 60%) of the crack front experienced SIFs similar to the values estimated based on the $\sqrt{}area_{Murakami}$ (Figure 2-9 (n), (p), and (r)). This contrast suggested that the SIF estimated by current defect-sensitive fatigue models for irregular defects can be more conservative than that estimated for circular defects. Specifically, in Ti-6Al-4V, defects are typically surrounded by randomly oriented grains; there is a higher probability of finding favorably oriented grains for fatigue crack initiation when the highly stressed regions of defects are larger or when larger portions of the crack front are experiencing higher SIFs. Murakami et al. also emphasized the need for corrections to the $\sqrt{}area_{Murakami}$ parameter for cracks that were irregular, slender, deep, or feature a concave crack front [26,49,85].

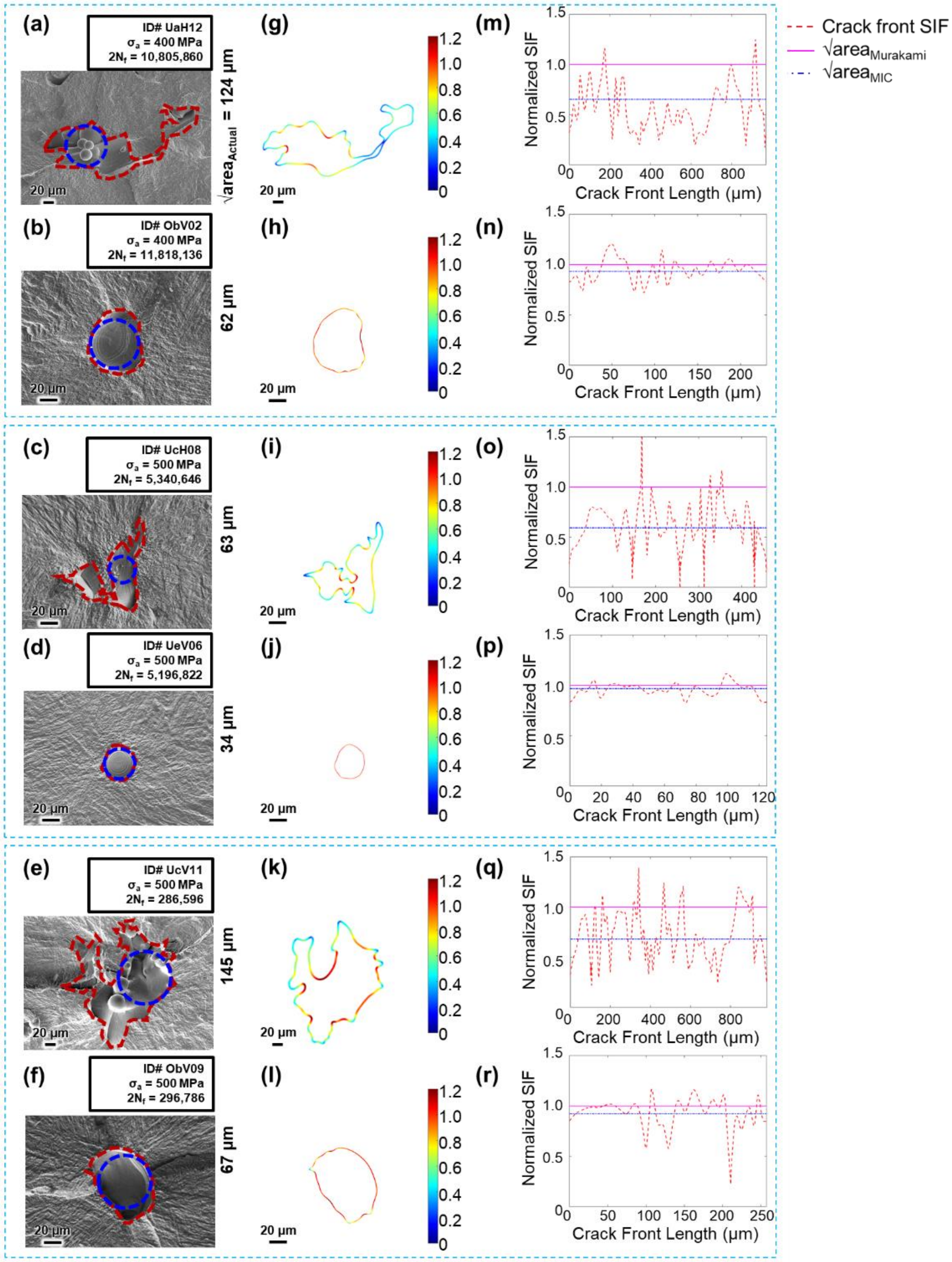

Figure 2-9. Comparison of pairs of defects having different morphologies but similar fatigue lives. Panels in the first column are fractographs showing pairs of irregular ((a), (c), and (e)) and circular ((b), (d), and (f)) defects. The red-dashed envelopes in the first column mark the boundary of defects, and the blue-dashed circles indicate the MIC of the defect. The second column visualizes the distribution of normalized SIF on planar cracks whose shapes are identical to the 2D profiles of the respective defects. The third column presents the normalized SIFs as a function of distance along the crack front. Reference lines of SIFs estimated based on $\sqrt{\text{area}}_{\text{Murakami}}$ and $\sqrt{\text{area}}_{\text{MIC}}$ are also included.

Noting the characteristics of modeled planar cracks that peak SIF occurs in the interior regions (i.e., near the MIC as shown in Figure 2-9 (g)-(l)), a new parameter is proposed in this study to represent volumetric defects' size based on the MIC size, i.e., $\sqrt{area_{MIC}}$. As shown in Figure 2-9 (g)-(l), $\sqrt{area_{MIC}}$ was comparable to the existing $\sqrt{area}$ parameters for circular defects, whereas, for irregular defects, the $\sqrt{area_{MIC}}$ was considerably smaller. Additionally, the $\sqrt{area_{MIC}}$ decreased with increasing irregularity, suggesting that it could capture the fact that irregular defects tended to correspond to similar fatigue lives as circular ones of the same $\sqrt{area_{Actual}}$. The SIFs calculated using $\sqrt{area_{MIC}}$ (i.e., $SIF = 0.5 \times \sigma_a \sqrt{\pi \sqrt{area_{MIC}}}$), as shown by the blue dot-dashed lines in Figure 2-9 (m)-(r), appear to be typical of the SIF curves of the planar cracks regardless of the defect shape.

The relevance of various $\sqrt{area}$ parameters of the fatigue critical defects to fatigue lives was further investigated using the largest extreme value distribution (LEVD) [70,71,86]. In this study, the probability density functions (PDF) of the LEVD were calculated using the non-parametric Moments method [87,88] in terms of reduced variate, Y_i, as:

$$Y_i = -\ln\left(-\ln\left(i/N + 1\right)\right) \tag{2.3}$$

where i and N are the rank and total number of crack-initiating defects, respectively.

The probability plots in terms of Y_i are shown in Figure 2-10 for both irregular and circular defects, estimated using three different size measures: $\sqrt{area_{Actual}}$, $\sqrt{area_{Murakami}}$, and $\sqrt{area_{MIC}}$. In addition, Figure 2-11 shows the probability density of $2N_f$ for both irregular and circular defects. The probability density plots with respect to different size measures and $2N_f$ are also shown in Figure A6-10 and Figure A6-11, respectively. No significant difference in the distribution of $2N_f$ between fatigue failures caused by irregular and circular defects is observed in Figure 2-11 (and

Figure A6-11), suggesting that if a defect size measure is suitable, the defect size distributions for both defect types should also be identical. While the defect size distributions for $\sqrt{area}_{Actual}$ and $\sqrt{area}_{Murakami}$ showed a significant difference between circular and irregular defects (see Figure 2-10 (a)-(d)), the distribution based on $\sqrt{area}_{MIC}$ exhibited minimal variation (see Figure 2-10 (e)-(f)). Consequently, the $\sqrt{area}_{MIC}$ could be used as an alternative parameter for defect size measurement for both surface and internal defects, accounting for defects' shape.

The potential application of the proposed $\sqrt{area}_{MIC}$ parameter is not limited to the correlation between defect features measured from fractgraphy with fatigue behavior as exemplified above. $\sqrt{area}_{MIC}$ also has the potential to be used with nondestructive examination techniques, such as XCT, as a more robust approach to identify fatigue critical defects in a part and assess its probability of failure under intended service loads. Common defect size measures, such as $\sqrt{area}_{Actual}$ and $\sqrt{area}_{Murakami}$, are sensitive to the resolution of XCT scans and can become inaccurate for irregular defects, as they contain fine features that may be lost at reduced resolutions [89–91]. In contrast, scan resolution is less likely to impact $\sqrt{area}_{MIC}$, since the MIC typically corresponds to the bulkier regions of defects that can be easily captured.

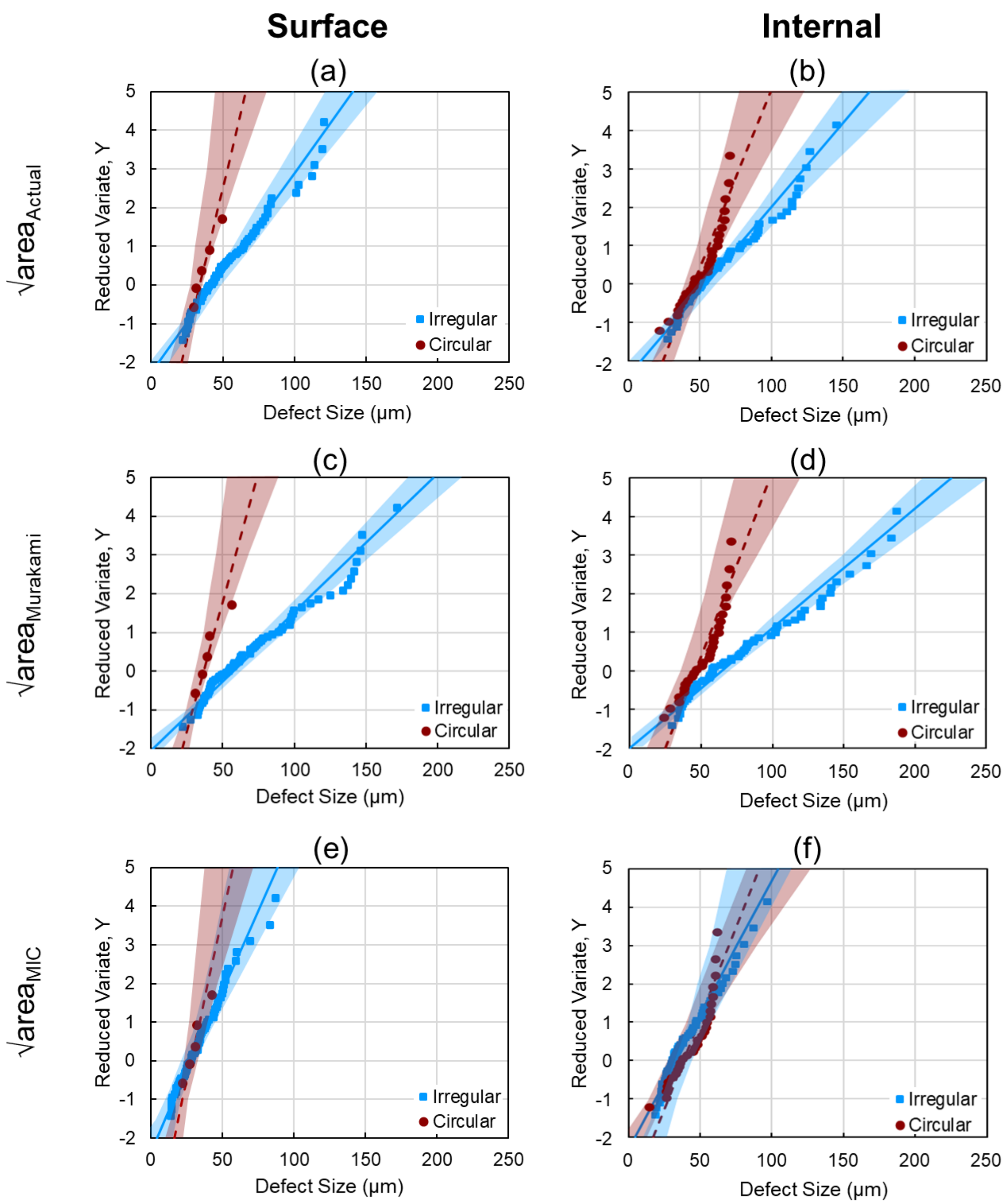

Figure 2-10. Reduced variate with respect to crack-initiating defect size measured using different defect size parameters: (a)-(b) $\sqrt{area}_{Actual}$, (c)-(d) $\sqrt{area}_{Murakami}$, and (e)-(f) $\sqrt{area}_{MIC}$. Surface defects include both surface-exposed and near-surface ones.

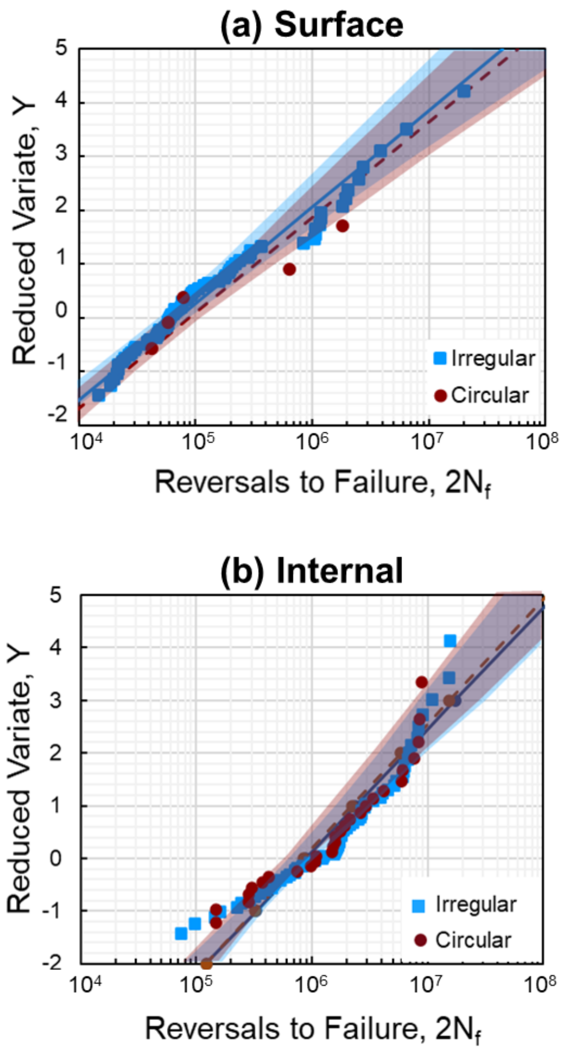

Figure 2-11. Reduced variate of *$2N_f$* distribution for (a) surface and (b) internal crack-initiating defects of Ti-6Al-4V specimens. Surface defects include both surface-exposed and near-surface ones.

2.4. Conclusions

This study investigated the effect of volumetric defect's size, location, and shape on the fatigue behavior of L-PBF Ti-6Al-4V specimens. Volumetric defects of various morphological features were induced into the specimens by varying the process parameters during fabrication. Following fatigue tests, careful fractography was performed for the examination of various features of fatigue critical defects. By treating 2D defect profiles extracted from fractographs as planar cracks, linear elastic finite element analysis was performed to examine how the defect shape influenced the distribution of stress intensity factor along the crack front. The following conclusions were drawn:

- Defect location significantly influenced the fatigue behavior of AM specimens, with surface defects being more critical than internal ones. Fatigue critical defects that were near-surface generally corresponded to the shortest fatigue lives, followed by surface-exposed and internal defects.
- The effect of defects' size on fatigue life was obscured by their shape and location. After isolating and excluding these factors, a reasonable correlation between defect size and fatigue life was observed.
- Among internal volumetric defects that resulted in similar fatigue lives, the irregular ones were found to be larger than their circular counterparts when measured using existing defect size measurement approaches. This implied that the defect size estimated with the existing approaches could not adequately represent the severity of defects by addressing their shape.
- Linear elastic finite element analyses of planar cracks suggested that, unlike circular cracks, only a small fraction of irregular cracks' front, i.e., near their maximum inscribed circles, experienced high stress intensity factor values. This implied that irregular defects were less severe for fatigue crack initiation compared to circular defects of the same size and location.
- The proposed defect size parameter, $\sqrt{area_{MIC}}$, could account for the effect of defect shape. SIF calculated using $\sqrt{area_{MIC}}$ appeared to be more representative of planar crack's true SIF, regardless of their shape. The identical distributions of $\sqrt{area_{MIC}}$ and fatigue lives for circular and irregular defects suggested that $\sqrt{area_{MIC}}$ could be used as an alternative defect size parameter.

The application of the proposed $\sqrt{area_{MIC}}$ parameter can be extended to the nondestructive examination techniques, such as XCT, to identify fatigue critical defects and their impact on the fatigue performance of the part. In particular, since the MIC typically corresponds to the bulkier regions of defects, the scan resolution will be most likely less impactful on measuring the accurate $\sqrt{area_{MIC}}$. Finally, the proposed approach should be evaluated for different defect sensitive materials containing a wide range of defect shapes to assess its robustness.

3. A fracture mechanics based semi-probabilistic fatigue lifing approach for additively manufactured Ti-6Al-4V

3.1. Introduction

Adoption of additive manufacturing (AM) in key industries, such as aerospace, for safety-critical part fabrication has been limited primarily due to the additively manufactured (AM) materials' considerably scattered and often inferior fatigue properties, making the establishment of reliable fatigue design allowables challenging [92]. This is rooted in the presence of volumetric defects inherent in AM parts [93], which can act as stress risers and, in surface machined condition, lead to early crack initiation, especially in materials with fine microstructure such as Ti-6Al-4V [2–5]. The severity of stress concentration varies with the morphological features of these defects—such as their size and shape—which are sensitive to the perturbations in local thermal history [6,94]. Accounting for the resulting wide fatigue variability through traditional, statistics based qualification approaches, without addressing the failure mechanism, can lead to either significant overdesign (due to exceedingly low allowable to ensure reliability) or noncompliance (due to insufficient reliability in pursuit of acceptable allowable) [29–31].

Traditional fatigue qualification relies on established methods for predicting the fatigue life (and lower bound for fatigue life) of a component under cyclic loading, often using stress-life (S-N) curves that express the 'nucleation time' for smooth specimens made of wrought materials [14]. For materials with low volumetric defect densities, fatigue design curves can be statistically determined from test data as a conservative locus corresponding to a low failure probability [95]. The low failure probabilities required for safety-critical parts (failure probabilities of the order of 10^{-5} for the entire life [96]) are then obtained by applying a safety design factor to material design curves to obtain the 'fatigue allowables' [97–100]. Another practice in the aerospace field for 'safe life' assessment is to derive, from the experimental S-N data, a fatigue life curve corresponding to 10^{-3} failure probability, P_f, for assessment against a 99.99%ile of the nominal service stresses (since actual service stresses always tend to deviate from the nominal value at receding probabilities) [101,102]. However, with the presence of significant scatter in fatigue data, the statistically determined design allowables can be significantly lower than the mean, which can lead to overly conservative part designs. As such, developing strategies to explicitly consider the failure mechanisms (i.e., the incorporation of effect of defects for materials such as Ti-6Al-4V) into fatigue design is necessary, which is a practice currently outside the scope of conventional qualification methodologies. The stochastic nature of defect distribution and the role of defect morphology on fatigue behavior call for a defect-tolerant and probabilistic qualification approach to enable the part qualification for safety-critical applications.

Defect-tolerant design philosophy focuses on predicting the cyclic life span of components with existing flaws and defects, utilizing crack growth-based approaches and treating these flaws/defects as initial cracks. It is especially suitable for AM metallic materials, where the ubiquitous presence of volumetric defects accelerates fatigue crack initiation and the life fraction for crack growth is accentuated, and, as such, holds promise to resolve the challenges faced by the conventional qualification for AM materials. Nevertheless, the small crack growth regime requires special treatment since the small cracks initiated from the defects exhibit lower threshold stress intensity factors, crack closure levels, and crack growth rates [103]. By considering initial defect size, attempts to apply numerous models based on the concepts of 'short crack' threshold (Murakami [48,49], El-Haddad [50], R-curve [104]) for fatigue strength and growth (Murakami-Endo [105], NASGRO equation [32,33], Shiozawa's model [106]) to describe S-N plots and the fatigue response of AM parts in the presence of defects have been made with various degrees of success [20,44,47,107–110]. Nevertheless, the incorporation of defect's other morphological aspects, such the shape and location, in these models remains largely unaddressed.

This study examines the efficacy of traditional and defect-tolerant approaches for the construction of material design curves for laser powder bed fused (L-PBF) Ti-6Al-4V parts. Experimentally observed fatigue data of L-PBF Ti-6Al-4V [93], where fatigue cracks initiated from volumetric defects with variations in the size, shape, and location was utilized for the examination. A novel lifing approach is proposed, which emphasizes on the growth life of short cracks initiating from the volumetric defects, incorporates the effects of defect shape and location, and utilizes the crack growth constants corresponding to the short crack regime. The limitations of traditional methods for fatigue design curve construction were identified, and an alternative semi-probabilistic framework based on fracture mechanics and compliant with current regulatory requirements is proposed.

3.2. Methodology

3.2.1. Fatigue data

Fatigue data used for modeling in this manuscript were collected from the authors' previous study [93]. In that study, L-PBF Ti-6Al-4V rods were fabricated in varied process parameters to induce underheated, recommended, and overheated processing conditions to achieve a reasonable variation in the morphologies of the volumetric defects [8,111–113]. The rods were stress-relieved at 704°C for 1 hour [74,75], followed by furnace cooling, and machined to the geometry of fatigue specimens according to the ASTM E466 standard [114]. The final geometry of the fatigue specimens is included in Figure A6-12 in the Appendix B. After machining, the normal components of residual stress (RS) acting along the loading direction were measured at different depths from the free surface of the fatigue specimens, following the SAE HS 784 standard [115], reported in Ref. [93], and also included in Section 6.1.2 of Appendix A.

Room temperature fatigue tests were conducted in uniaxial, force-controlled, fully-reversed (stress ratio, $R_\sigma = -1$) mode, following ASTM E466 standard [114], at stress amplitudes, σ_a, of 400, 450, 500, 600 MPa. The specimens that did not fail by 2×10^7 reversals were considered run-outs. Fractography was conducted on all failed fatigue specimens to obtain the fatigue critical defects' size and their morphological features using a scanning electron microscope. All failed specimens in this study experienced fatigue failure due to crack initiation from volumetric defects. The S-N fatigue plots for different processing conditions are shown in Figure 3-1. In Figure 3-1, the fatigue critical defects located at/near the free surface are indicated by triangles, whereas the internal ones are indicated by squares. Run-out specimens are indicated with arrows. Classification of defects based on their location (i.e., surface vs. internal) and size is discussed in Section 2.2.2. As shown in Figure 3-1, underheated specimens exhibited greater scatter in fatigue lives than the overheated and recommended ones, due to larger variations in the crack-initiating defects' sizes and their morphological features.

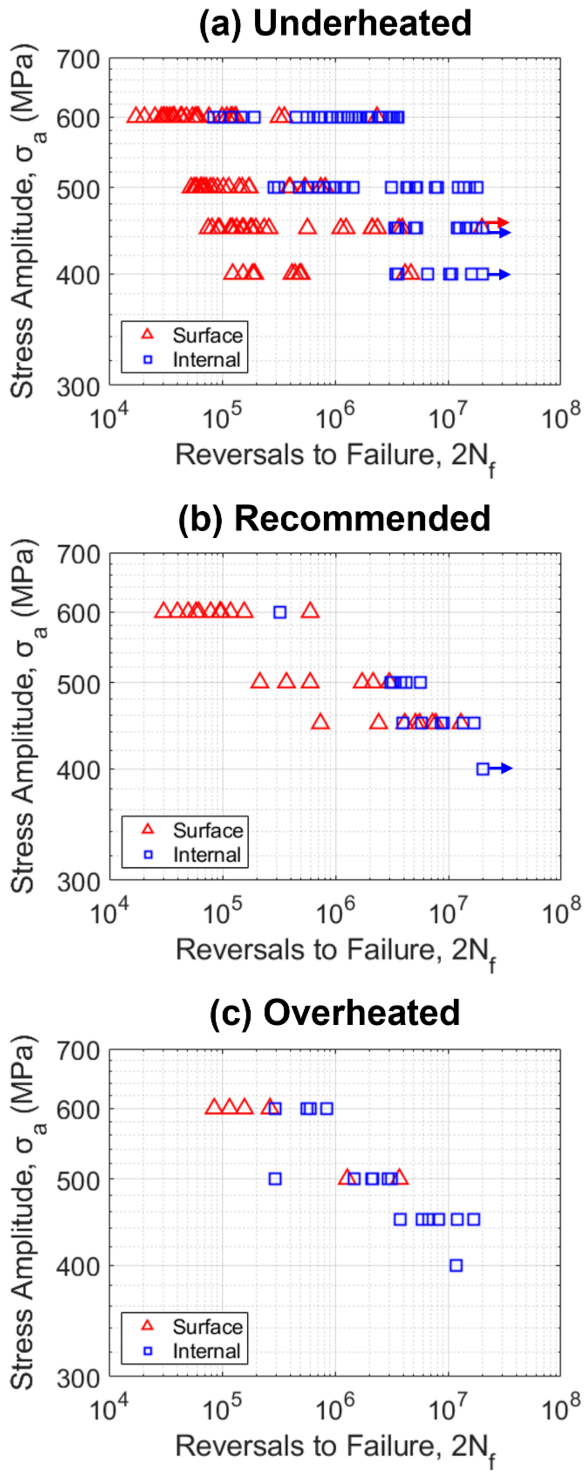

Figure 3-1. S-N fatigue plots of L-PBF Ti-6Al-4V specimens fabricated in different processing conditions: (a) underheated, (a) recommended, and (c) overheated. Arrows indicate run-out fatigue tests.

3.2.2. Defect size measurement and location classification approaches

Two defect size measurement approaches, as shown in schematic illustrations for both single and multiple crack-initiating cases in Figure 3-2 (a)-(b), are used in this study. They are $\sqrt{area}_{Murakami}$, which is the square root of the area of a convex hull surrounding the defect's projection measured according to Murakami's approach [26], and $\sqrt{area}_{MIC}$, which is the square root of the area of the maximum inscribed circle (MIC) within the defect's projection [93]. In the previous study [93], it was demonstrated that the $\sqrt{area}_{MIC}$ accounted for the combined effect of internal defect's size and shape on fatigue behavior, while $\sqrt{area}_{Murakami}$ was appropriate for surface defects.

To account for defect's location, following the classification criteria introduced by Wu et al. [64], defects were categorized as either surface or internal based on their location relative to the free surface (Figure 3-2 (c)). The criteria classified a defect as a 'surface defect' if either of the following conditions was met: (1) the distance from the free surface to the nearest point of the defect, e, was zero (i.e., the defect was surface-exposed), or (2) the square root area of the convex hull enveloping both the defect and the free surface, $\sqrt{area}_{eff}$ (indicated by the red-dashed line in Figure 3-2 (c)), was greater than e. Conversely, the defect was classified as 'internal' otherwise. The internal defects whose $e \geq 500$ μm were further classified as 'deep-internal' defects. The number of specimens failing from surface-exposed, near-surface, internal (excluding deep-internal), and deep-internal defects is included in Table 3-1. Note that only the specimens with single crack-initiating defects (a total of 165 specimens) are included in Table 3-1. Some representative fracture surfaces of different failure origins are shown in Figure 3-3.

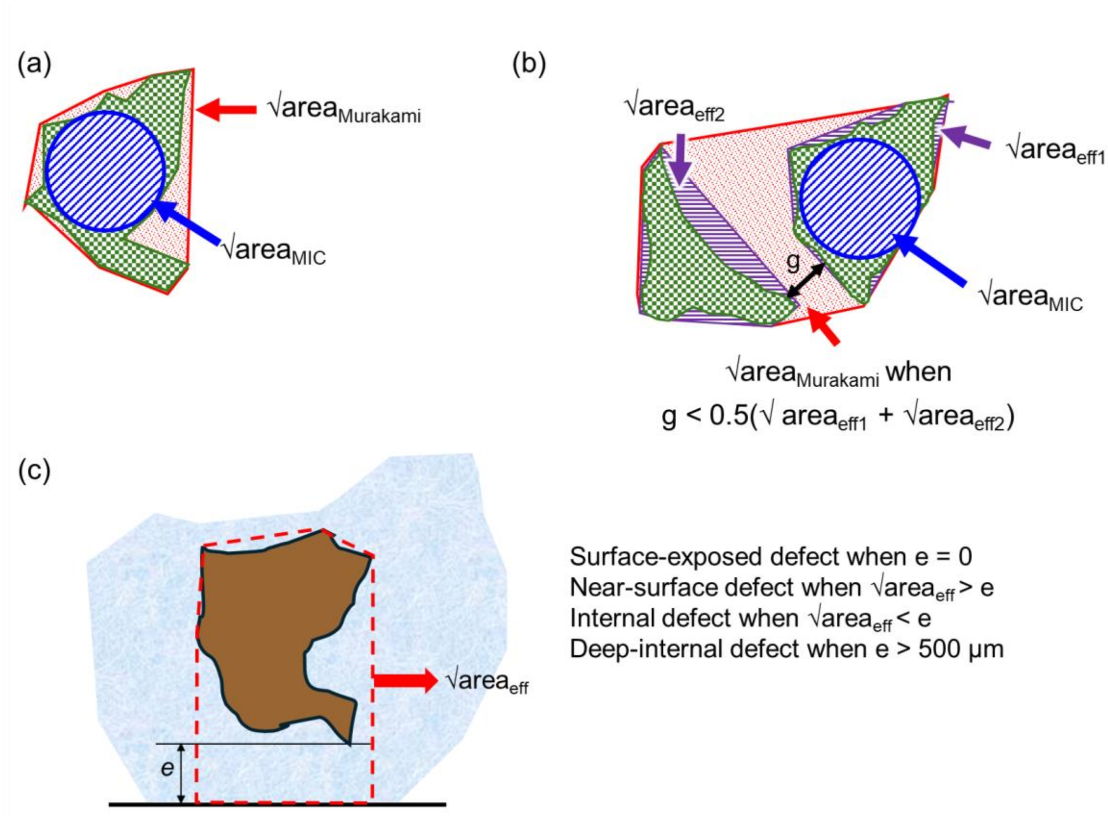

Figure 3-2. Description of different size measurements for crack-initiating defects with (a) single- and (b) multi-initiation cases, and (c) classification of locations of defects.

Table 3-1.Number of specimens with crack-initiating defects from different locations.

Crack-initiating defects' location	**No. of specimens**
Surface-exposed	26
Near-surface	46
Internal (excluding deep-internal)	56
Deep-internal	37

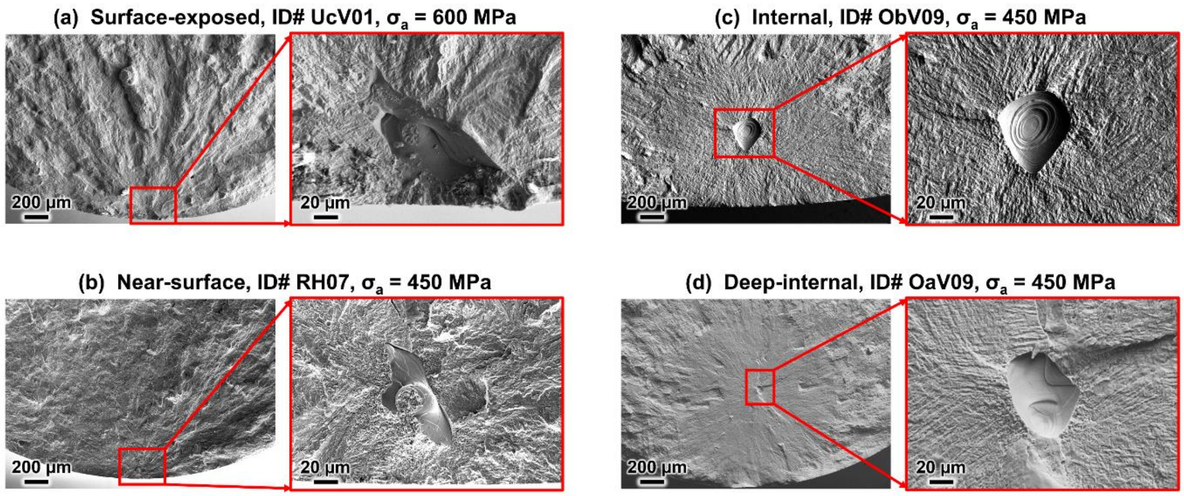

Figure 3-3. Fracture surfaces of L-PBF Ti-6Al-4V specimens for (a) surface-exposed, (b) near-surface, (c) internal, and (d) deep-internal crack-initiating defects.

3.2.3. S-N plot and fatigue allowables

The data from the different processing conditions demonstrate the material fatigue variability in the presence of the variability of the manufacturing process conditions [4,10,93] and the data can be analyzed to obtain a prospective S-N plot. The stress values in the S-N data were corrected with the RS at the crack-initiating defect's centroid based on the RS measurements presented in Ref. [93] and Section 6.2.2 of Appendix B. Specifically, the RS was superimposed with the applied stresses, and the effective stress ratio, R_{eff}, was calculated, according to the procedure outlined in the Ref. [14]. Afterwards, the effective σ_a for $R_\sigma = -1$ was calculated using R_{eff} based on the Walker equation [14], as discussed in Section 6.2.3 of Appendix B. The RS-corrected S-N data were then interpolated with an equation of the type [116]:

$$N_f = A\sigma_a{}^{-n}, \tag{3.1}$$

where N_f is cycles to failure, A and n are coefficient and exponent of the fitted curve.

The fatigue data, including run-outs, were fitted with Eq. (3.1) using the maximum likelihood estimation (MLE) method [117]. It was assumed that the N_f data follow a log-normal distribution, which was equivalent to a Gaussian distribution for $\log_{10}N_f$, where the mean, μ, has been defined by Eq. (3.1) and the standard deviation, s, is independent of σ_a. The fitted S-N curve, corresponding to the failure probability, P_f, of 50%, along with the complete fatigue dataset are shown in Figure 3-4 and the MLE parameters are reported in Table 3-2.

Table 3-2. Parameters for the S-N plot.

$\mathbf{log_{10}(\boldsymbol{A})}$	20.8201
$\boldsymbol{n}$	5.5890
$\boldsymbol{s}$	0.7360

According to United States Federal Aviation Administration (FAA) regulations [118], the material fatigue design curve for a primary non-redundant component is the failure curve with 99% survival probability (i.e., P_f = 1%) with 95% confidence (i.e., this corresponds to A-basis allowable for Metallic Materials Properties Development and Standardization [95]). In this study, the FAA design curve has been adopted, which can be calculated as:

$$\log_{10}\left(N_{f,design}\right) = \mu - 2.326s, \tag{3.2}$$

which corresponds to the 1%ile of the standard normal distribution. Substituting the log transformation of Eq. (3.1) into Eq. (3.2) provides:

$$\log_{10}\left(N_{f,design}\right) = \log_{10}(A) - n\sigma_a - 2.326s. \tag{3.3}$$

The P_f = 1% line, estimated using Eq. (3.3), along with its 90% two-tail confidence band are shown in Figure 3-4. Details about the calculation of the confidence band through the local Fisher information matrix of MLE can be found in Ref. [117].

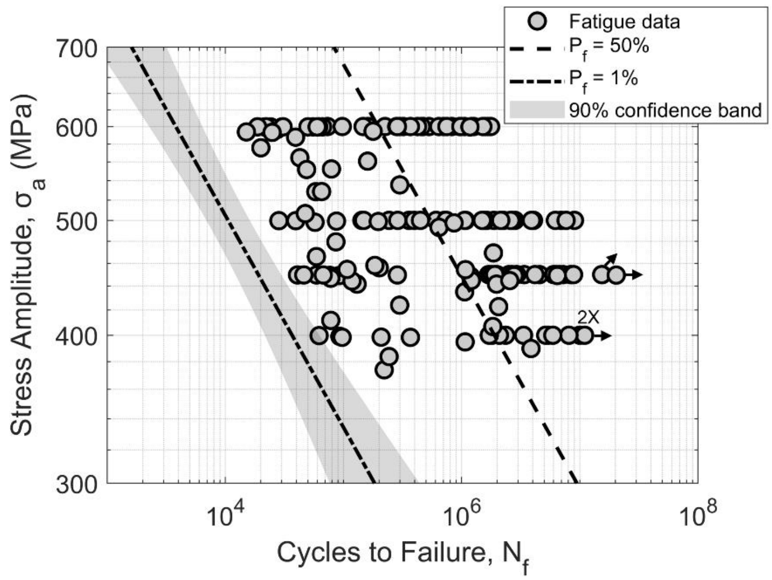

Figure 3-4. S-N plot with lines corresponding to $P_f = 50\%$ and $P_f = 1\%$ with its 90% confidence band. Arrows indicate run-out fatigue tests, and the 90% confidence band is shown by the filled grey area.

The $P_f = 1\%$ line appeared to provide extremely short fatigue lives (2×10^3 - 8×10^4 cycles), compared with average fatigue lives (2×10^5 - 2×10^6 cycles) for σ_a within the interval of 650-350 MPa. This overly conservative estimation of fatigue lives was a result of the significant scatter in the fatigue data (s = 0.73), which was due to the wide variations in the crack-initiating defect features [93]. Traditional qualification procedures, which do not consider the distinct physical mechanisms of fatigue failures driven by specific material anomalies, are inherently limited in their scope to account for such variability in both defect morphology and the resulting fatigue behavior. Therefore, implementing a defect-tolerant approach, based on fracture mechanics principles and considering a defect size at a desired probability of occurrence, would provide a more appropriate estimation of the design curve.

3.3. Analysis of experimental results

3.3.1. Defect location dependence

The S-N data, initially presented in Figure 3-4, are classified based on the crack-initiating defects' location and are separately presented in Figure 3-5 for surface and internal defects, along with the same fitted $P_f = 1\%$ and $P_f = 50\%$ lines from Figure 3-4. From Figure 3-5 (a), it is evident that all the failures originated from surface-exposed defects, even when accounting for the potential presence of negative RS, consistently appearing on the lower 50% of the fatigue lives (fatigue life < $P_f = 50\%$ line) across the entire S-N plot. This indicates significantly reduced fatigue resistance when crack initiation occurs from surface defects. On the other hand, when examining the specimens which failed due to internal defects, their lives are clustered within the upper 50% of fatigue lives, as shown in Figure 3-5 (b). Moreover, deep-internal defects (i.e., internal defects with $e \geq 500$ µm) do not show a significant difference in their fatigue lives with respect to the other internal defects. The present observations about considerably longer lives for internal defects are consistent with recent studies on AM materials, which have presented similar evidence for Ti-6Al-4V [119] and Scalmalloy [120].

These observations of defect locations affecting the fatigue lives confirm that it is important to prospectively determine and consider the difference in growth rates of cracks initiating from surface and internal defects. It is also demonstrated that the lower bound of the overall fatigue lives is controlled by surface-exposed defects, and therefore, when developing fatigue design curves using the defect-tolerant approach, the crack-initiating defect located at the free surface of a part should be considered.

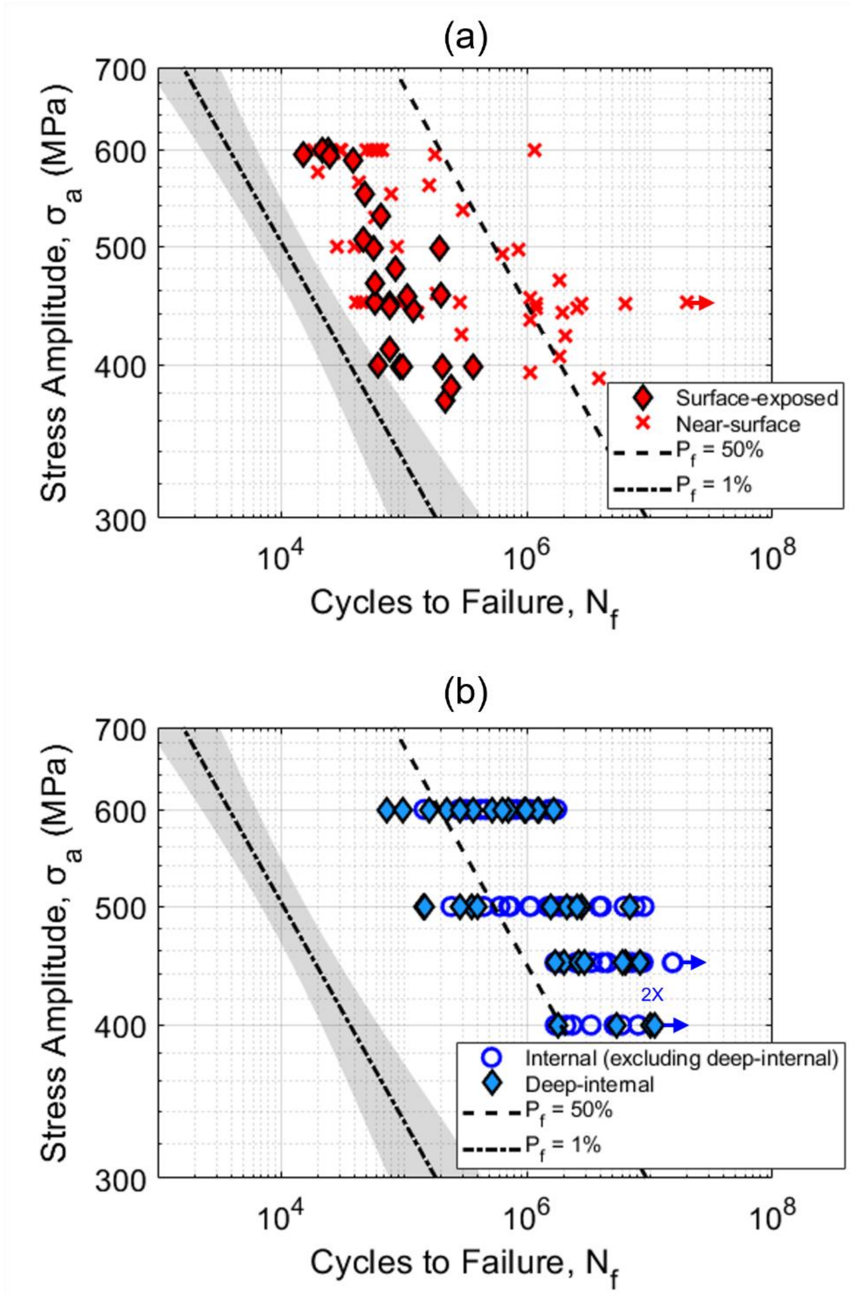

Figure 3-5. Dependence of fatigue response on defect location: specimens failed due to (a) surface and (b) internal defects. Arrows indicate run-out fatigue tests. Grey shades indicate 90% confidence band of the line for $P_f = 1\%$.

3.3.2. Analysis with Shiozawa diagram

The Shiozawa's equation [121] was originally derived from the Paris-Erdogan equation for fatigue crack growth [122] for evaluating the growth rates of cracks initiating from casting defects. It was derived under the assumption that, for cracks initiating from defects, the crack growth phase dominated the total fatigue life, and the growth rates could be expressed using the Paris-Erdogan equation [122,123] as:

$$\frac{da}{dN} = C(\Delta K)^m, \tag{3.4}$$

where C and m are the coefficient and exponent [54,55], respectively. Integrating Eq. (3.4), from an initial crack size, $\sqrt{area_i}$, under the hypothesis that the $\sqrt{area_i}$ was considerably smaller than the final crack size, $\sqrt{area_f}$ at failure, Shiozawa proposed the following relationship:

$$\Delta K_{initial} = \left[\frac{C(m-2)}{2}\right]^{-\frac{1}{m}} \left(\frac{N_f}{\sqrt{area_i}}\right)^{-\frac{1}{m}} = K' \left(\frac{N_f}{\sqrt{area_i}}\right)^{-d\prime}, \tag{3.5}$$

$$K' = \left[\frac{C(m-2)}{2}\right]^{-\frac{1}{m}},$$

$$d' = \frac{1}{m},$$

where the term $N_f/\sqrt{area_i}$ is referred to as defect-related fatigue life and $\Delta K_{initial}$ is stress intensity factor (SIF) range corresponding to the initial crack size. K' and d' are the coefficient and exponent. Equation (3.5) represents a linear relationship between $\Delta K_{initial}$ and $N_f/\sqrt{area_i}$ in a log-log plot (named as Shiozawa diagram). $\Delta K_{initial}$ can be calculated as:

$$\Delta K_{initial} = Y\Delta\sigma\sqrt{\pi\sqrt{area_i}}, \tag{3.6}$$

where $\Delta\sigma$ is the stress range, and Y is the location dependent factor, which is 0.65 for surface cracks and 0.5 for internal cracks according to Ref. [26].

It was shown that the Shiozawa diagram can accurately describe the fatigue crack growth behavior of materials in the presence of defects (in castings and AM materials) [107,121,124]; however, no distinction was made between the surface and internal defects in those studies. Based on the dependence of the crack-initiating defect's location on fatigue lives discussed in Section 3.3.1 and the evidence from literature regarding the slower growth rates of internal cracks than surface ones [36,125,126], Shiozawa diagrams are constructed separately for surface and internal defects in this study. The Shiozawa diagrams, presented in Figure 3-6, demonstrate that the trend in data for surface and internal defects are distinct. To examine this trend further, the data of surface-exposed and deep-internal defects are fitted with function given by Eq. (3.5), as shown in Figure 3-6, which was labelled as 50% interpolation line since the fitted line represents the average crack growth behavior. Surface-exposed defects among all surface defects are selected for fitting since they exhibited the shortest fatigue lives among different defect locations [58–60]. In the case of internal defects, only the ones with $e \geq 500$ μm (i.e., deep-internal defects) have been considered for the fitting, because they satisfy the hypothesis at the basis of Shiozawa's equation (which, in fact, has been proposed for failures of internal defects in superlong fatigue [121]). In addition, since for these defects most of their life is spent in the propagation of the so-called fish-eye [26], e can be taken as the final crack size.

The distinct growth behavior of surface-exposed and deep-internal defects can also be noticed from the 50% interpolation lines plotted in Figure 3-6 (a)-(b). From Figure 3-6 (a), it is confirmed that for a given $\Delta K_{initial}$ (a given combination of $\Delta\sigma$ and $\sqrt{area_i}$), the surface-exposed defects have the shortest $N_f/\sqrt{area_i}$, while the near-surface defects have longer $N_f/\sqrt{area_i}$. For the same $\Delta K_{initial}$ levels, the internal defects (shown in Figure 3-6 (b)) have considerably longer

$N_f/\sqrt{area_i}$ than the surface-exposed defects (compare with Figure 3-6 (a)), indicating that cracks initiated from them experienced substantially lower growth rates.

Using the s of $N_f/\sqrt{area_i}$ data and a confidence level of 80%, the lower (10%) and upper (90%) scatter band of the interpolation line are constructed, corresponding to -1.282s and +1.282s, respectively, and are also shown in Figure 3-6. The line corresponding to the 10% scatter line denotes a 90% exceedance, i.e., 90% of defects are expected to exhibit a crack growth rate slower (i.e., longer defect-related fatigue life, $N_f/\sqrt{area_i}$) than the one indicated by this line. Paris-Erdogan constants, calculated using the K' and d' corresponding to the 50% interpolation and 10% scatter lines, are presented in Table 3-3.

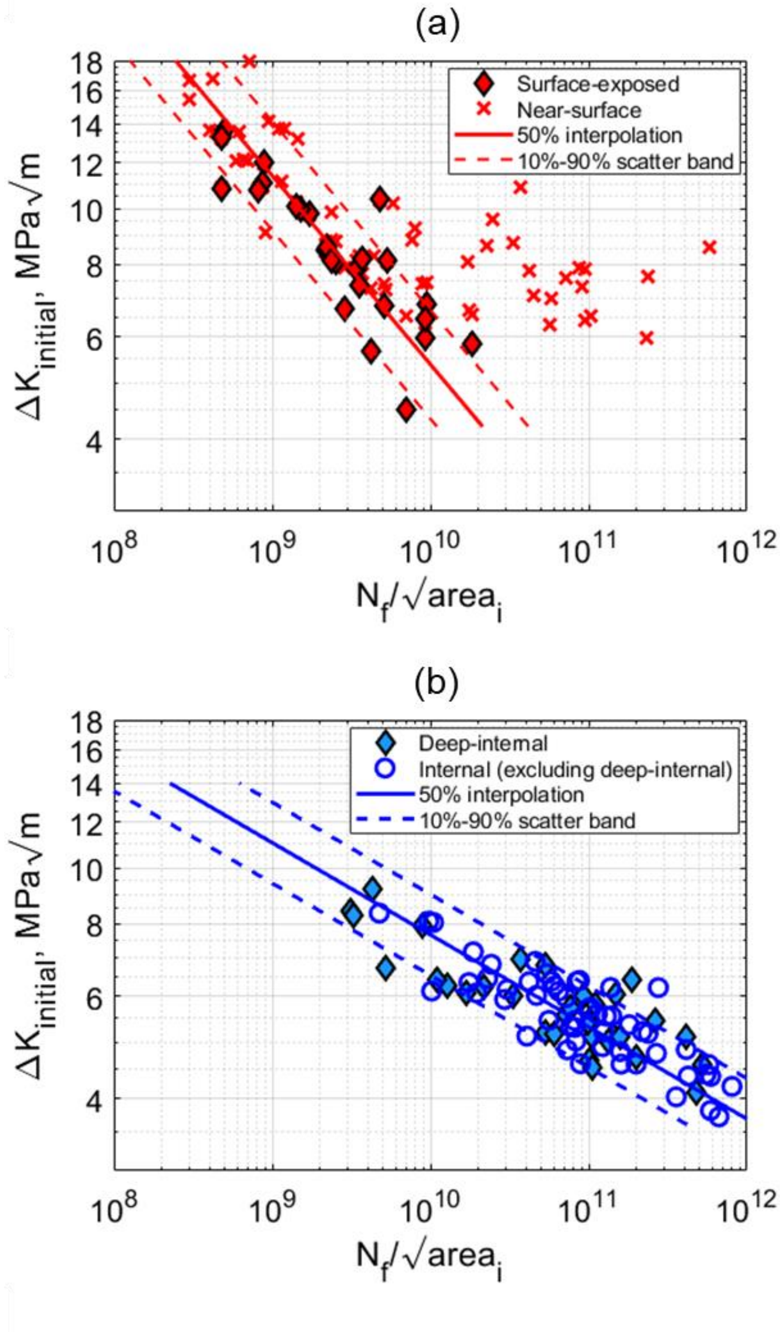

Figure 3-6. Shiozawa diagrams for (a) surface defects (the interpolation and scatter band lines are calculated based on surface-exposed ones); (b) internal defects (the interpolation and scatter band lines are calculated based on deep-internal ones).

The distinct growth rates of surface-exposed and deep-internal cracks are also supported by the results of dedicated experiments in Ref. [126,127] that have clearly shown that the absence of environmental effects slows the crack growth rate. Other support to the different growth rate for internal defects come from the many evidences about a different S-N diagram for superlong fatigue failures originated by internal defects [128–131].

It is also worth mentioning that this result also explains the reason for near-surface defects having slightly longer $N_f/\sqrt{area_i}$ than the surface-exposed ones, since a portion of their growth is spent in the absence of air [127,132,133]. The cracks nucleating from internal defects, in their initial phases of life (i.e., before reaching the free surface), have considerably slower growth rates than the ones nucleating from surface-exposed defects. The methodology for life prediction incorporating the difference in growth behavior will be detailed in the following section.

Table 3-3. Paris-Erdogan constants obtained from Shiozawa plots for L-PBF Ti-6Al-4V.

	Surface		**Internal**	
	C $\left(\frac{\mathrm{m/cycle}}{(\mathrm{MPa}\sqrt{\mathrm{m}})^{\mathrm{m}}}\right)$	m	C $\left(\frac{\mathrm{m/cycle}}{(\mathrm{MPa}\sqrt{\mathrm{m}})^{\mathrm{m}}}\right)$	m
Average constants (obtained from 50% interpolation line)	2.13×10^{-12}	3.07	1.28×10^{-16}	6.29
Conservative constants (obtained from 10% scatter line)	4.14×10^{-12}	3.07	3.51×10^{-16}	6.29

3.4. Fatigue life estimation

3.4.1. Proposed crack growth-based lifing approach

Fatigue crack growth rate curves for cracks initiating from surface and internal defects, derived using the Paris-Erdogan equation and material constants listed in Table 3-3, are shown in Figure 3-7. Cracks initiated from surface-exposed defects and the ones from defects located underneath grow following the growth rate curves shown using the red and blue lines, respectively, in Figure 3-7 [68,69]. The cracks initiated from internal defects, once opened to the free surface, should grow at the surface crack growth rates. The following methodology is employed to describe crack growth in the different stages.

For surface crack growth modeling, the shape of crack is assumed to be semi-circular and an equivalent initial crack radius, a_i, is used as the crack size. The methodology used for modeling surface and internal crack growth is illustrated in Figure 3-8 (a). The SIFs at the deepest point on the crack front, estimated using the closed form equations for semi-elliptical cracks in a solid cylinder [134,135], are used in this approach. Fatigue lives are estimated using the Paris-Erdogan equation [122,123] as:

$$N_f = \int_{a_i}^{a_f} \frac{da}{C(\Delta K)^m}, \tag{3.7}$$

where the Paris-Erdogan constants C and m are obtained from Shiozawa curves and are given in Table 3-3. Numerical integrations are performed using Eq. (3.7), following the incremental crack extension methodology [136], until the final crack radius, a_f, reached 2 mm.

Cracks initiated from defects located underneath the free surfaces grow towards the surface and interior simultaneously, as illustrated in Figure 3-8 (b) using blue curves. The growth rates of these cracks are higher toward the surface and lower when they grow toward the interior regions [51,137]. For these defects (including internal and near-surface ones), a_i is estimated by assuming the shape of the crack as circle. Closed form SIF equations for embedded cracks in a round bar are used [138]. Different SIFs are considered for the point closer to the free surface and the point towards the interior ($\Delta K_a > \Delta K_b$) to mimic the difference in crack growth rates towards either direction, as shown in Figure 3-8 (c). The number of cycles elapsed until the crack reached the surface is estimated, using the Paris-Erdogan constants for internal cracks (see Table 3-3). Once the internal crack (blue dashed line) approaches the free surface, it transitions into a surface crack (red solid line), as illustrated in Figure 3-8 (d). The growth following surface crack transition is characterized by the surface crack growth rates, as shown by red lines in Figure 3-8 (b). The crack growth continued until the final crack size reached 2 mm. The number of cycles that elapsed after the surface crack transition until 2 mm is estimated. The sum of the number of cycles spent during a crack's growth through all relevant phases is considered as the fatigue life, i.e., N_f.

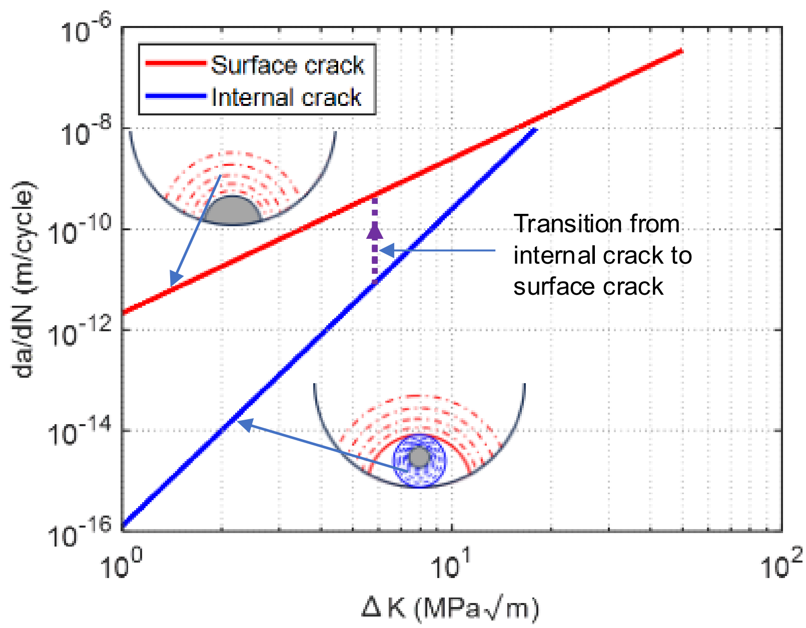

Figure 3-7. Crack growth curves used in modeling for surface and internal cracks.

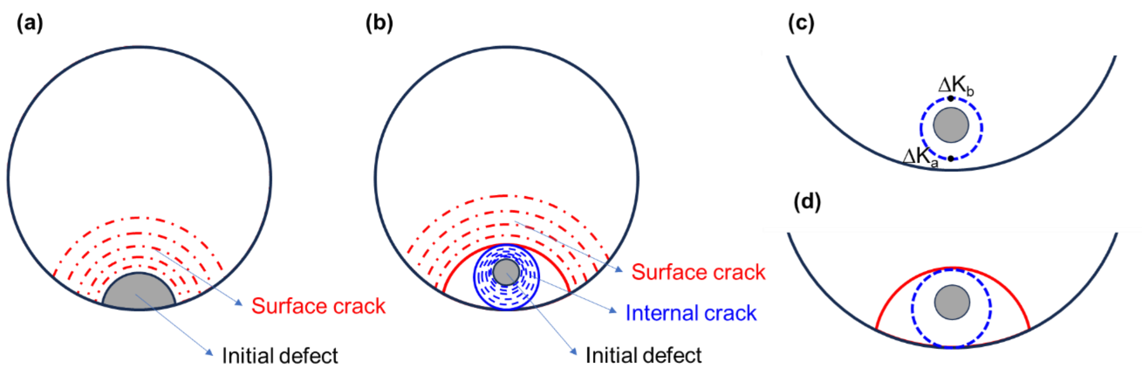

Figure 3-8. (a) Procedure used for surface crack growth modeling, (b) procedure used for modeling an internal crack growth and the transition of an internal crack into a surface crack, (c) procedure followed for modeling growing cracks at different rates towards and away from the free surface, and (d) procedure followed for modeling transitioning the internal crack to a surface crack.

3.4.2. Comparison with experiments

Estimated reversals to failure, $2N_f$, following the proposed methodology, are plotted against the experimentally observed $2N_f$, as shown in Figure 3-9. For the estimation, the initial defect size measured using $\sqrt{area}_{Murakami}$ is used for surface-exposed and near-surface defects, whereas the size measured using $\sqrt{area}_{MIC}$ is used for internal defects. Fatigue lives are estimated using the average Paris-Erdogan constants (obtained from the 50% interpolation line discussed in Section 3.3.2) and the conservative constants (obtained from the lower 10% scatter line), as shown in Figure 3-9. It is evident from Figure 3-9 (a)-(b) that the use of Paris-Erdogan constants derived from a lower 10% line provides conservative fatigue life estimations, which are well suited for industries seeking to minimize the probability of failure. Fatigue life estimation of one specimen (shown with black arrows in Figure 3-9 (a)-(b)) was always non-conservative, irrespective of the Paris-Erdogan constants used; and fractography of that fatigue specimen revealed multiple coexisting crack planes from one fatigue critical defect which indicated an accelerated, simultaneous initiation of multiple cracks.

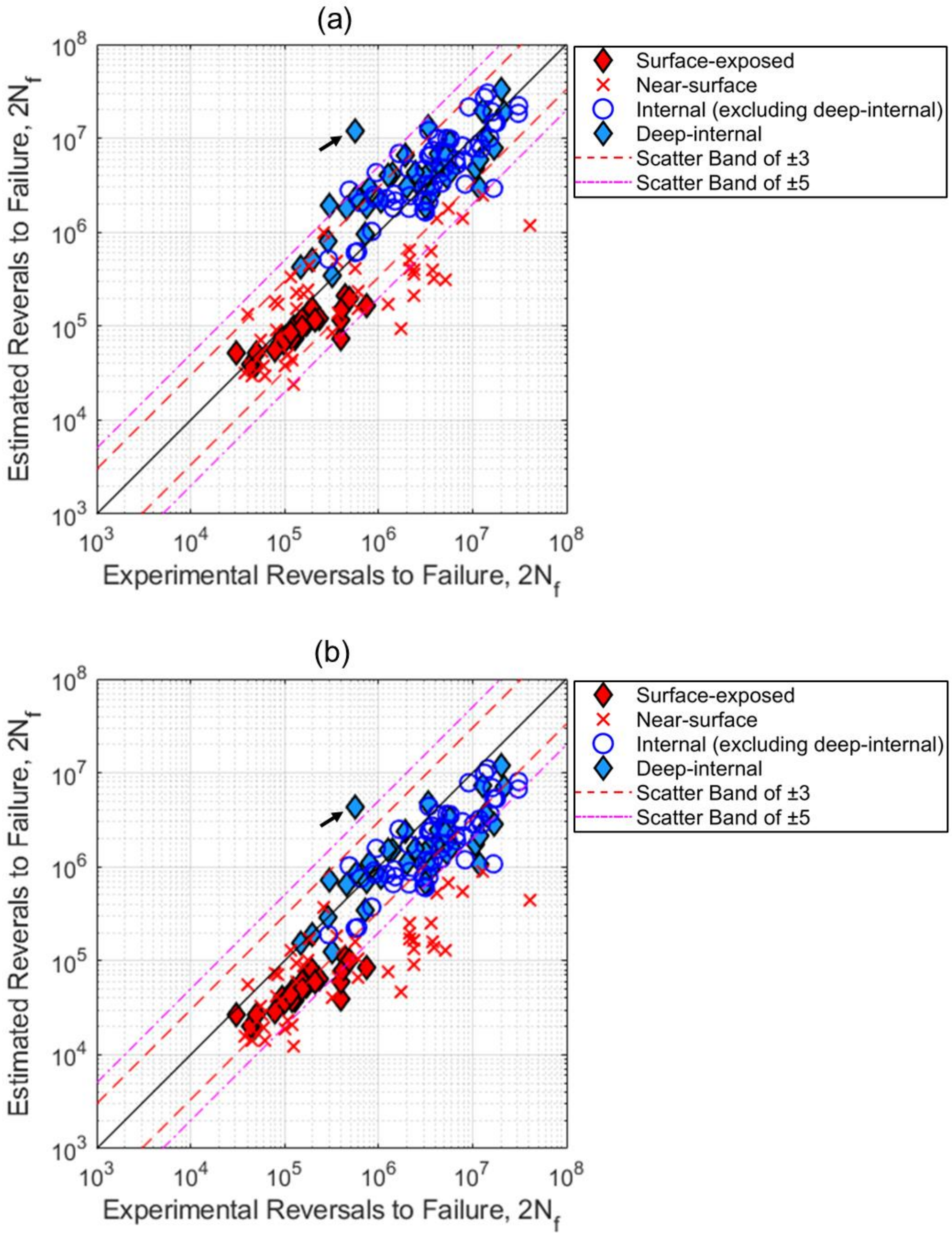

Figure 3-9. Crack growth approach estimated vs. experimentally observed $2N_f$ of L-PBF Ti-6Al-4V using (a) average Paris-Erdogan constants and (b) conservative Paris-Erdogan constants.

3.5. Fracture mechanics based approach for derivation of design curve

3.5.1. Defect-based fatigue allowables

The crack growth-based lifing approach discussed in the previous section can be used as the basis for a defect-based definition of a design curve fulfilling the requirements of the FAA regulations. Since the fatigue failure in L-PBF Ti-6Al-4V is controlled by the crack propagation from defects, the fatigue life corresponding to $P_f = 1\%$, i.e., $N_{1\%}$, can be determined using the crack growth approach. This means determining $N_{1\%}$ corresponds to the crack growth life from a critical defect of size of 99% probability of occurrence, $a_{99\%}$, (i.e., the defect size which has 1% probability of being exceeded). Mathematically, which may be expressed as:

$$N_{1\%} = N_f(a_{99\%}): P_f = 1\%, \tag{3.8}$$

where $N_{1\%} = N_f(a_{99\%})$ is a lifetime function, which can be estimated from Eq. (3.7) for an initial crack size $a_{99\%}$. Considering that Eq. (3.7) can be approximated to a line on $\log_{10}(a)$ - $\log_{10}(N_f)$ (according to the Shiozawa's hypothesis that $a_f >> a_i$), this concept can be visualized in Figure 3-10 (a), where the $N_{1\%} = N_f(a_{99\%})$ is linear on a log-log scale, for a given $\Delta\sigma$.

The results presented in Section 3.3 shows that the growth rates of cracks initiated from surface-exposed defects are considerably higher than the internal defects, which lead to the shortest fatigue lives, as shown in Figure 3-5. Therefore, a conservative approach for establishing a fatigue design curve based on the effective fatigue damage is to consider a life estimate based on the most detrimental fatigue mechanism, i.e., the growth of a crack initiated from surface-exposed defects of size $a_{99\%}$.

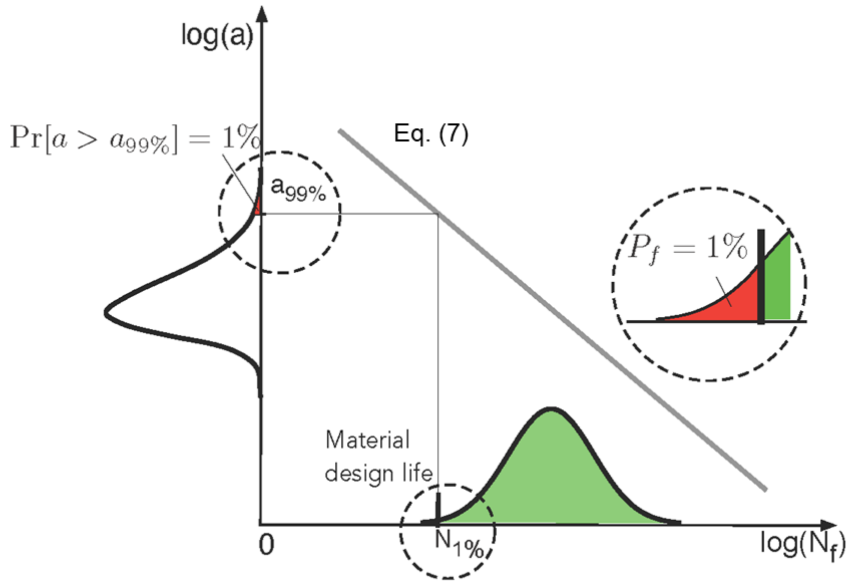

Figure 3-10. Concepts for the determination of a material design curve where life for $P_f = 1\%$ corresponds to fatigue crack initiation/growth from a defect of size $a_{99\%}$.

3.5.2. Semi-probabilistic approach

Since the defects randomly occur in the volume of specimens, their occurrence can be described using 'extreme value statistics'. The distribution of defects can be described with a largest extreme value distribution (LEVD) or Gumbel distribution, whose cumulative distribution function for the largest defect size, x, expected in 1 specimen, $F_{(max,1spec)}(x)$, is of the form [139]:

$$F_{max,1spec}(x) = \exp\left[\exp\left(-\frac{x-\lambda}{\delta}\right)\right], \tag{3.9}$$

where λ and δ are the location (which is also its modal value) and scale parameters of the Gumbel distribution, respectively. It was shown in Ref. [93] that the size of surface defects could be described by LEVD parameters. The parameters λ and δ of the Gumbel distribution, describing the surface defect data, are estimated with the Moments method [86,140], yielding: $\hat{\lambda} = 55.22$ µm and $\hat{\delta} = 27.72$ µm.

As introduced in Section 3.5.1, the defect for $P_f = 1\%$ corresponds to the defect size with a return period T = 100 (i.e., the defect size that is expected to be exceeded once every 100 specimens, i.e., $a_{99\%}$ [69]. The estimate of $a_{99\%}$ can be calculated as:

$$\hat{x}(T) = \hat{\lambda} + \hat{\delta}.(-\log_{10}(-\log_{10}(1 - 1/T))), \tag{3.10}$$

and its 90% confidence band can be estimated following ASTM E2283-03 [88]. This $a_{99\%}$ defect size corresponding to the return period T = 100 in one specimen is the modal value (most probable value) of the distribution of the largest defect found in each of a set of one hundred specimens, as illustrated in Figure 3-11. The cumulative distribution function for x expected across a set of 100 specimens, $F_{(max,100\ spec)}(x)$, is of the form:

$$F_{max,100\ spec}(x) = \left[F_{max,1\ spec}(x, \lambda, \delta)\right]^{100}. \tag{3.11}$$

Equation (3.11) is again another LEVD [69]. For this distribution, the modal value and the 5% and 95%iles (together with their confidence bands that can be calculated by Eq. (3.11) and expressions for confidence bands in ASTM E2283-03 [88]) are shown in Table 3-4.

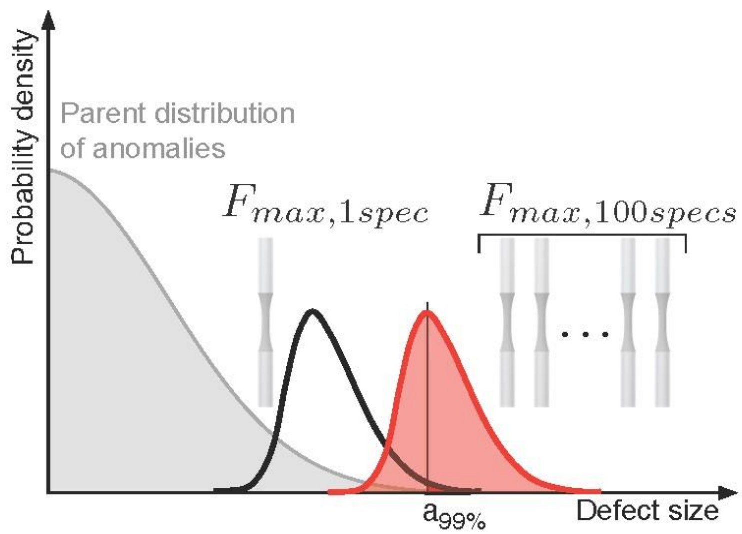

Figure 3-11. Schematic illustration of the probability density of defect with size $a_{99\%}$ (red bell curve) expected to be exceeded once in a batch of 100 specimens.

Table 3-4. Characteristic values of the largest surface defect whose size $a_{99\%}$ is with a probability of exceedance of 1% (defect with return period T = 100 specimens) with their 90% confidence bands.

5%ile	**Modal value**	**95%ile**
152. 5 ± 21.0	182.7 ± 27.0	265.2 ± 43.5

The lower bound of fatigue life (the life for a target P_f = 1%) could be estimated by integrating Eq. (3.7) for the estimated $a_{99\%}$ defect size with T = 100 and the conservative Paris-Erdogan constants corresponding to surface cracks. The reason for this choice is that this set of constants provide conservative life estimates, and therefore, the adoption of this conservative crack growth constants allows to avoid the burden of a fully probabilistic Monte Carlo simulation [141–143]. The fatigue design curves, estimated following the crack growth model, using the defect size obtained from the semi-probabilistic approach and the characteristic values of Table 3-4, are shown in Figure 3-12. The design curve estimated based on the largest surface defect for T = 100 aligns closer to the experimental fatigue data than the traditional fatigue design curve based on P_f

= 1%. This T = 100 design curve, being steeper than the P_f = 1% curve, also suggests that fatigue lives do not increase as significantly with decreasing σ_a as indicated by the traditional design curve. Hence, the T = 100 design curve provides a more appropriate basis for the conservative design of L-PBF Ti-6Al-4V.

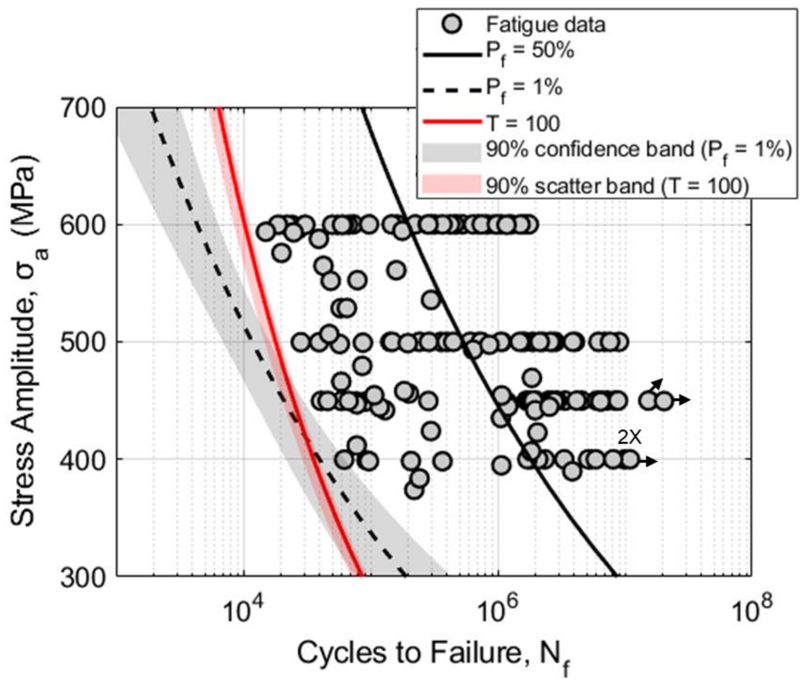

Figure 3-12. S-N fatigue plot of L-PBF Ti-6Al-4V with P_f = 50%, P_f = 1%, and fatigue design curve based on the largest surface defect for T = 100. Arrows indicate run-out fatigue tests.

3.5.3. Discussion

The approach adopted in the analysis stems from the understanding that the variability in fatigue properties is due to diverse processing conditions. It is worth mentioning that the resulting scatter of the experimental fatigue lives with s = 0.73 is extremely larger than the typical variability recommended by fatigue assessment standards. For instance, welded structures, that is historically known to exhibit a large scatter of fatigue properties, have a typical fatigue scatter s = 0.20 [144,145]. In the presence of a significantly larger scatter for the Ti-6Al-4V dataset, as shown in Figure 3-12, it becomes evident that a traditional fatigue design curve derived from the entire dataset is excessively conservative. This is because the variability in the fatigue data is primarily due to the variability in defect size (here considered by the LEVD for most detrimental defects) and the presence of two different growth rates for surface-exposed and internal defects [146].

From this point of view, the defect-tolerant approach highlighted in this research clearly offers a more refined and appropriate strategy as it provides a conservative lower bound fatigue design curve closer to experimental outcomes. This method, by incorporating the influence of defect size and location on crack growth behavior, accurately estimated fatigue life.

3.6. Conclusions

This study performed fracture mechanics based fatigue life estimation and estimated fatigue design curves for defect laden laser powder bed fused Ti-6Al-4V. The effect of defect size, shape, and location on fatigue behavior was accounted for in this approach, utilizing a proposed crack growth-based lifing approach. The following conclusions were drawn:

- The fatigue design curves estimated using the conventional approaches were excessively conservative for the investigated material, and potentially for other defect-sensitive materials.
- The cracks initiated from surface and internal defects experienced different crack growth rates, due to which surface defects resulted in considerably shorter fatigue lives. This suggested the need to quantitatively account for distinct growth rates in modeling and prediction.

- The proposed crack growth-based lifing approach, incorporating the effect of defect size, shape, and location on fatigue behavior, accurately estimated fatigue lives. The estimated fatigue lives of both surface and internal defects using average Paris-Erdogan constants were within the scatter bands of ±5 with respect to the experimentally observed fatigue lives.
- The fatigue design curves estimated using the proposed crack growth approach and the largest possible defect size for a given failure probability were shown to be superior to account for the significant scatter in the fatigue behavior than the existing design curve estimation methodologies, which were overly conservative.

4. Transferability of defect-fatigue relationships across laser powder bed fusion platforms

4.1. Introduction

Additive manufacturing's (AM's) tendency of generating volumetric defects in parts is among the reasons for many industries' hesitancy in the adoption of the technology. This is especially the case for Ti-6Al-4V parts in the aviation industry [147–149], where the intricate geometries could benefit from the net-shaping capabilities of AM, since the material exhibits heightened sensitivity to these defects (in surface machined part condition) under cyclic loading and suffers debits in fatigue resistance [93,150,151]. The formation of volumetric defects is governed by the thermal history experienced by the part during fabrication, which is influenced by various factors, such as processing conditions and design factors, including part geometry, build orientation, and even the part's location on the build platform [4,152–155]. Careful characterization of the defect characteristics, fatigue behavior, and the defect-fatigue relationships is therefore necessary before adopting AM parts in fatigue-critical applications [47,53,69,93,156].

To complicate the matter, different AM machines, even the ones belonging to the same general family of technology (e.g., laser powder bed fusion (L-PBF)), tend to induce volumetric defects of different characteristics in parts, which also exhibit different dependence on minor adjustments in process parameters. This is due to the machines having distinct designs in powder delivery mechanisms, build chamber configurations, gas flow dynamics, and scanning strategies, to name a few [157]. The complex interplay of processing conditions and platform designs creates uncertainty in defects' morphological and spatial distributions, leading to considerable variations in the fatigue performance of identical parts fabricated on different AM platforms, whether from different OEMs or even different models by the same OEM. Such variations necessitate the evaluation of fatigue behavior of parts fabricated by each platform. However, generating statistically significant fatigue data for one AM platform already represents a substantial time and capital investment, accounting for such inter-platform variations relying on data generation alone can become prohibitively expensive. The challenge is amplified by the fast-paced evolution of AM technology, where new platforms constantly emerge and some existing ones are discontinued faster than the research needed to establish defect-fatigue relationships. A salient question arises: how should the dilemma between the daunting effort in the fatigue characterization for each AM machine and the rapid iteration of AM machines into the market be resolved?

A potential solution may lie in the establishment of transferability of the defect-fatigue relationships from one platform to another. If a material fabricated on different platforms can be demonstrated to obey the same or a similar defect-fatigue relationship, then the qualification of parts fabricated on a new platform can proceed with only the characterization for microstructure and defect content as well as limited fatigue testing, if necessary. This would drastically reduce the need for redundant, extensive experimental campaigns for material qualification for every new platform. However, studies systematically investigating this transferability have been lacking.

This study addresses this knowledge gap by examining the applicability of defect-fatigue relationships derived from Ti-6Al-4V specimens fabricated on one L-PBF platform to reliably predict the fatigue behavior of specimens fabricated on another. Fatigue data used in this study include the ones generated from an EOS M290 machine as part of a prior works [93,156] and the newly generated data from a Renishaw RenAM 500Q machine with specimens of identical geometry produced under comparable processing conditions. The Kitagawa-Takahashi diagram constructed from the EOS M290 data was first compared with fatigue data from the RenAM 500Q platform. Furthermore, Paris-Erdogan crack growth constants obtained from EOS M290 data were used to predict the fatigue lives of RenAM 500Q specimens. Finally, lower bound fatigue design curves developed from both platforms were compared to further confirm their cross-platform transferability.

4.2. Experimental procedures

4.2.1. Material and fabrication

Ti-6Al-4V cylindrical rods were fabricated using the L-PBF technique on a Renishaw RenAM 500Q Flex machine (designated as Platform 2) using plasma-atomized Ti-6Al-4V Grade 5 powder supplied by AP&C. To obtain a considerable variation in the defect characteristics, besides the manufacturer-recommended process parameters (referred to as R), rods were also fabricated using four other process parameters by altering the laser power, P, and scan speed, v (see Table 3-1). The specific adjustments applied to P and v, relative to the R values, were similar to those used in the authors' earlier study involving EOS M290 (designated as Platform 1), but at a reduced scope [93]. The Platform 1 study consisted of a total of eight processing conditions, whereas the Platform 2 study utilized five processing conditions corresponding to a subset of the ones for Platform 1. The processing conditions used for Platform 1 and the designation of corresponding processing conditions from Platform 2 have been listed in Table 3-2. From Table 3-1 and Table 3-2, it can be observed that the process parameters used for R processing conditions differ significantly between the two platforms.

Among the five processing conditions used in Platform 2, two were chosen to result in insufficient energy input to introduce lack of fusions (LoFs) and were designated as underheated (U) conditions in this study. Two processing conditions utilized excessive energy input to introduce keyholes (KHs) and were designated as overheated (O) conditions. In addition, the cylindrical rods (which were machined to test specimens) with U and R processing conditions were fabricated in vertical (V) and diagonal (D) orientations to capture any directional influence of the irregularly shaped LoFs under cyclic loading. The O rods were fabricated only in V orientation, as the KHs were spherical and not expected to exhibit any directionality under cyclic loading. A total of eight specimen sets, each set defined by a unique combination of processing condition and part orientation, were fabricated on Platform 2 for fatigue and tensile testing.

Following the fabrication, the Ti-6Al-4V cylindrical rods underwent stress-relieving at 704°C for 1 hour in an electric muffle furnace before detaching from the build platform. The rods were then machined and polished to the final geometries of fatigue and tensile specimens, according to the ASTM E466 [158] and ASTM E8 [77] standards, respectively. The final geometry and dimensions of the fatigue specimens are shown in Figure 4-1. Each fatigue and tensile specimens set comprised 10 and 3 specimens, respectively. Details on tensile specimen geometry and tensile testing procedures are provided in Section 6.3.1 of Appendix C.

Table 4-1. Process parameters used for the fabrication of L-PBF Ti-6Al-4V specimens on Platform 2 in this study.

Designation of processing conditions	Parameter variation (%)	Power P (W)	Scanning speed v (mm/s)	Hatching distance h (μm)	Energy density E (J/mm^3)	Orientation of the specimens
U1	$P^{-10}v^{0}h^{0}$	153	1050	65	74.7	V, D
U2	$P^{-5}v^{0}h^{0}$	161.5	1050	65	78.8	V, D
R	$P^{0}v^{0}h^{0}$	170	1050	65	83.0	V, D
O1	$P^{+30}v^{-20}h^{0}$	221	840	65	134.9	V
O2	$P^{+20}v^{-30}h^{0}$	204	735	65	142.3	V

Table 4-2. Process parameters used for the fabrication of L-PBF Ti-6Al-4V specimens on Platform 1.

Desig. of process. conditions	Corres. process. conditions in Platform 2	Parameter variation (%)	Power P (W)	Scanning speed v (mm/s)	Hatching distance h (μm)	Energy density E (J/mm^3)	Orientation of the specimens
Ua	-	$P^{-20}v^{0}h^{0}$	224	1200	140	44.4	V, D, H*
Ub	-	$P^{0}v^{0}h^{+20}$	280	1200	168	46.3	V, D, H
Uc	U1	$P^{-10}v^{0}h^{0}$	252	1200	140	50.0	V, D, H
Ud	U2	$P^{-5}v^{0}h^{0}$	266	1200	140	52.8	V, D, H
Ue	-	$P^{0}v^{0}h^{+5}$	280	1200	147	52.9	V, D, H
R	R	$P^{0}v^{0}h^{0}$	280	1200	140	55.5	V, D, H
Oa	O1	$P^{+30}v^{-20}h^{0}$	364	960	140	90.3	V
Ob	O2	$P^{+20}v^{-30}h^{0}$	336	840	140	95.2	V

*H: Horizontal.

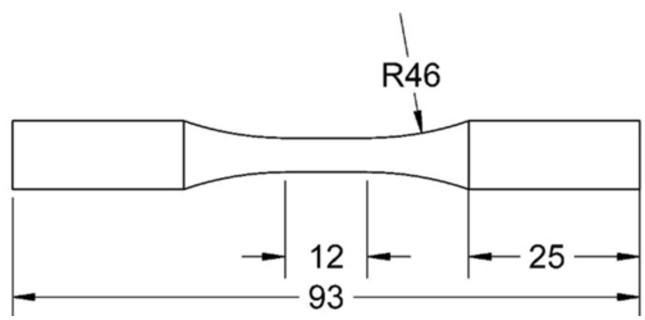

Figure 4-1. Geometry and dimensions of L-PBF Ti-6Al-4V fatigue specimen used in this study. All the dimensions are in mm.

4.2.2. Defect and microstructure characterization

The entire gage section of one fatigue specimen from each set was scanned using a Zeiss Xradia 620 Versa X-ray computed tomography (XCT) machine using a voxel size of 5.5 μm for obtaining the characteristics of volumetric defects. The XCT scanning was conducted with voltage of 140 kV and power of 21 W. After the XCT scans, the projection images were reconstructed and post-processed using Zeiss proprietary and Dragonfly software.

Microstructural analysis was performed on the longitudinal planes (i.e., the plane parallel to the axial direction of the specimens) of selected fatigue specimens at their gage. Prior to the microstructural analysis, samples were extracted from the fatigue specimens, then mounted in epoxy resin, ground, and polished with sandpapers of progressively finer grits to achieve a mirror finish. The microstructural analysis was conducted using a Zeiss Crossbeam 550 scanning electron microscope (SEM). Detailed microstructural information of the polished samples was collected using the electron channeling contrast imaging technique.

4.2.3. Fatigue testing and fractography

Uniaxial, force-controlled, fully-reversed fatigue tests (i.e., a stress ratio of -1) were performed, according to the ASTM E466 standard [78], using an MTS servo-hydraulic test system. The tests were conducted with three different stress amplitudes, σ_a, of 450 MPa, 500 MPa, and 600 MPa, at a frequency of 10 Hz. At least three fatigue tests were performed for each processing condition at every stress level. Specimens that exceeded fatigue lives of 10^7 cycles were considered as run-outs. Fractography of all failed specimens was conducted using the SEM to obtain the size, location, and other morphological features of the crack-initiating defects. Based on the location and size of crack-initiating defects, they were classified as surface and internal defects following the criteria proposed by Wu et al. [64] (Figure 4-2 (a)). Crack-initiating defects were classified as surface defects if either of the two conditions was met: (i) the defects were surface-exposed (i.e., the distance between the defect edge and free surface, e, is zero), or (ii) the defects were near-surface (i.e., the area enveloping the defect and free surface, $\sqrt{area_{eff}}$, is less than e). Defects were considered internal when $\sqrt{area_{eff}}$ > e. Surface defects' sizes were measured using the approach proposed by Murakami [26,48,49] (referred to as $\sqrt{area}_{Murakami}$ in this manuscript), while internal defects' size was measured using the square root of the area of the maximum inscribed circle (MIC), $\sqrt{area}_{MIC}$, as shown in Figure 4-2.

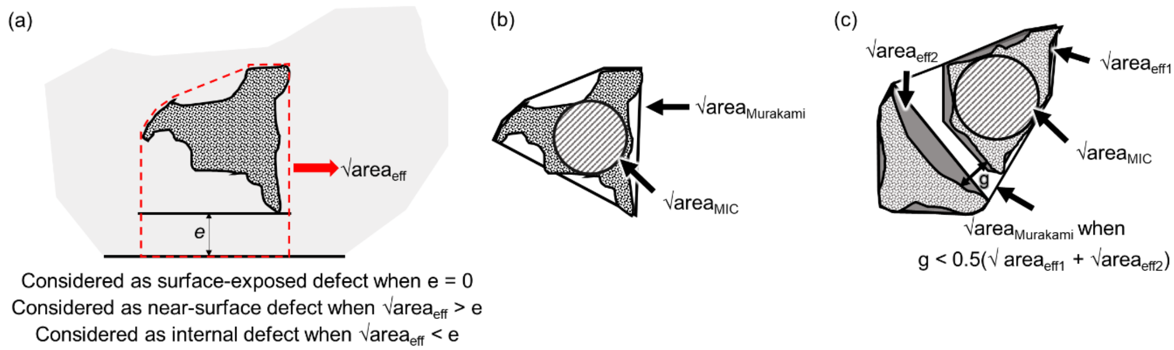

Figure 4-2. (a) Classification of crack-initiating defects based on distance from the free surface. Defect size measurements using different approaches for the cases of crack initiation from (b) a single and (c) more than one defects.

4.3. Experimental results

4.3.1. Defect and microstructure characteristics

Three-dimensional (3D) visualization of the XCT scans on specimens fabricated in both Platform 1 and Platform 2 for corresponding process parameter sets is presented in Figure 4-3. Defect characteristics such as the relative density, $\rho_{relative}$, and largest defect size (in terms of the square root of the projected area of the defect on the plane perpendicular to the loading axis, $\sqrt{area}$), along with energy density, E, are also shown in Figure 4-3. The images of the largest defect from each scan are shown in individual insets. Additional defect statistics such as the defect count per volume, maximum axis [58], and 90th percentile size (in terms of maximum axis), are presented in Figure 4-4 for comparison between platforms. As seen in Figure 4-3 and Figure 4-4, although both platforms exhibited similar tendencies of forming defects with respect to the change in energy input (i.e., U condition encouraging LoFs vs. O condition encouraging KHs), the overall defect counts of the respective conditions still differed between the platforms. This difference might be due to the differences in processing conditions other than the adjusted key process variables (i.e., build chamber design, gas flow, scanning strategy, layer thickness, etc.) between the two platforms.

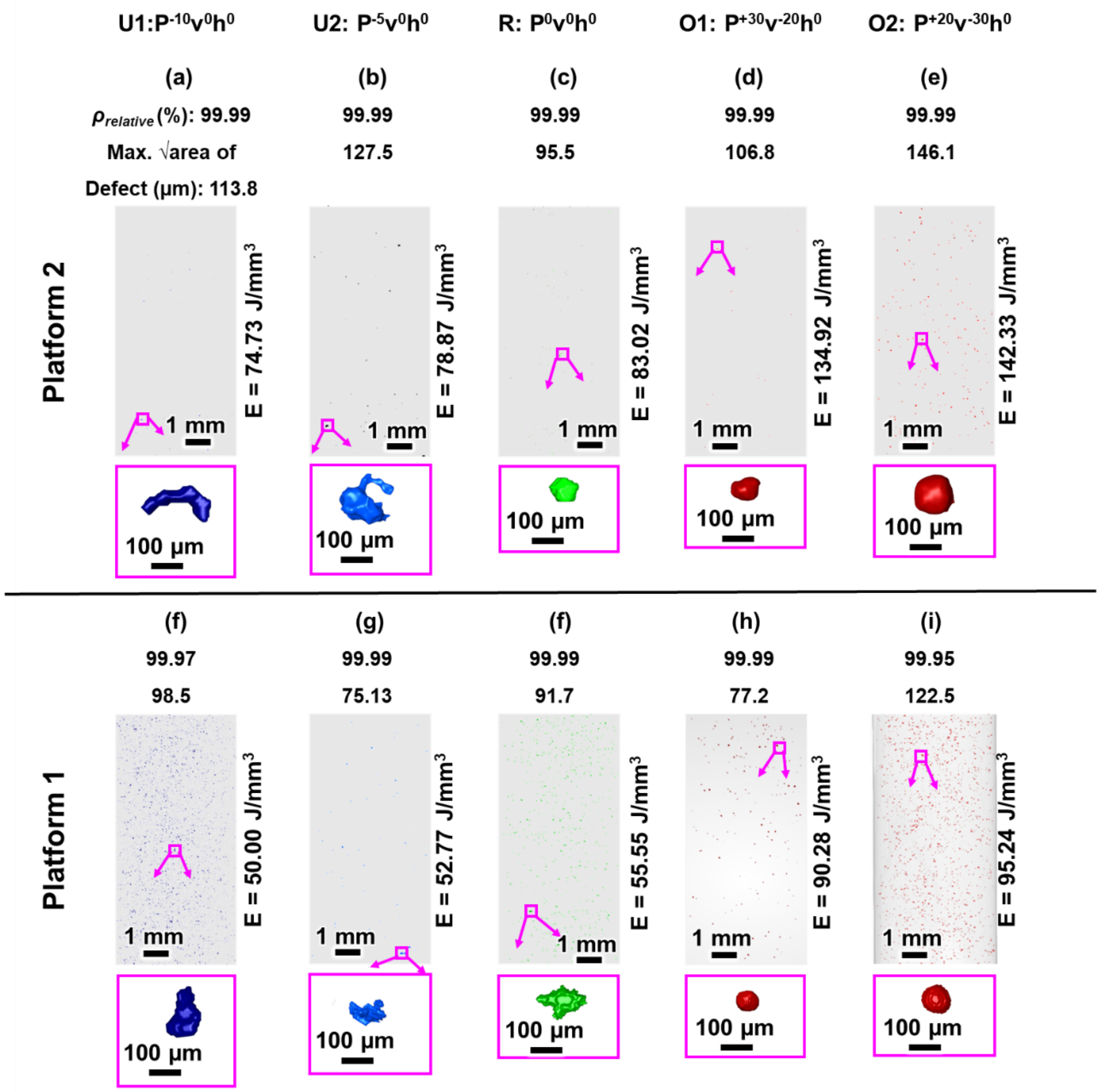

Figure 4-3. Comparison of 3D scanned volumes of L-PBF Ti-6Al-4V specimens fabricated using different processing conditions on both platforms.

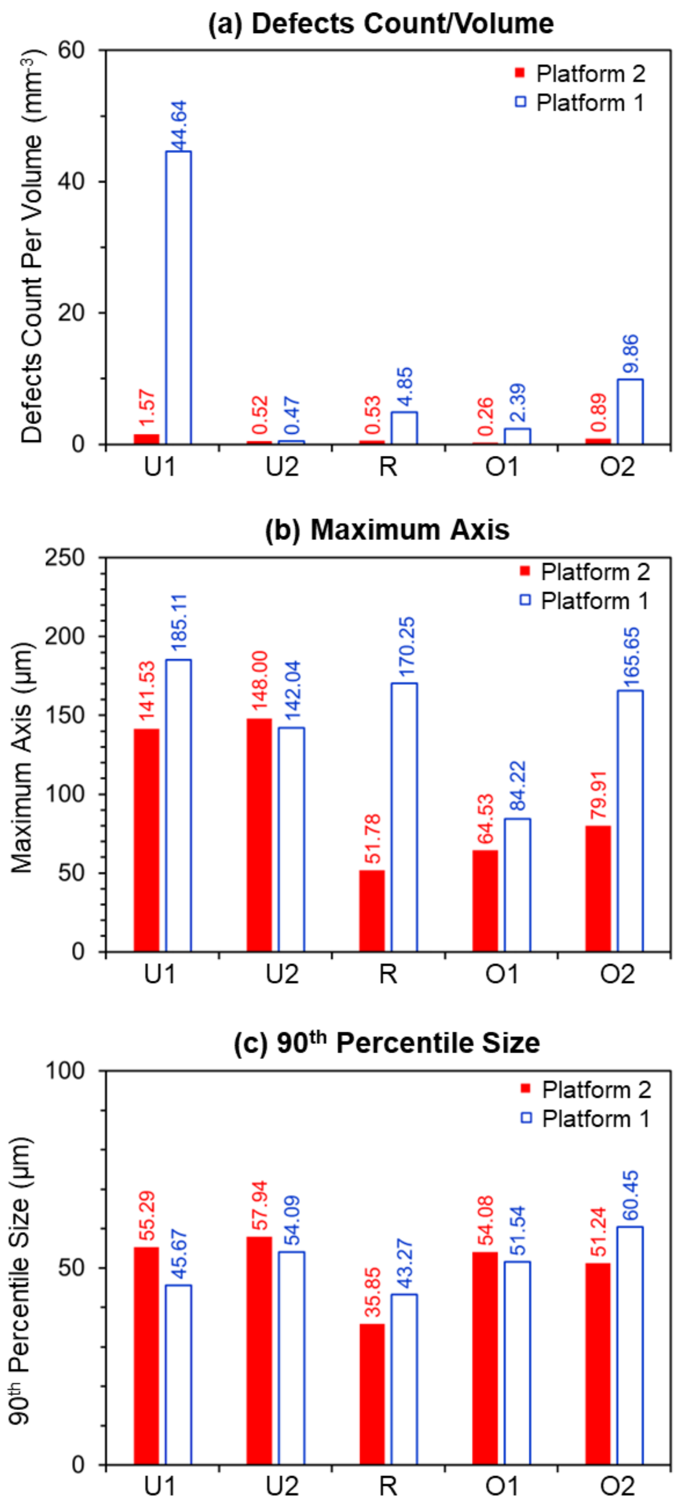

Figure 4-4. Comparison of defect statistics of specimens fabricated on two platforms using different processing conditions: (a) defects count per volume, (b) maximum axis, and (c) 90th percentile size.

Back-scattered electron (BSE) micrographs of L-PBF Ti-6Al-4V specimens, fabricated on both platforms, in longitudinal planes are shown in Figure 4-5. For samples from a given platform, the width of α-laths appeared to be similar, suggesting changes in process parameters did not significantly affect the microstructure. The majority of the α-laths in the samples from Platform 1 appeared to be very fine with a few coarse ones visible. In contrast, the α-laths in the samples from Platform 2 were more uniform in size, with thicknesses residing within the range of the fine and coarse α-laths in Platform 1 samples. Despite exhibiting minor microstructural differences, the tensile strengths of specimens from both platforms were comparable (Figure A6-15 in Appendix C) and exceeded the minimum tensile strengths specified by the ASTM F2924 standard [83] and Metallic Materials Properties Development and Standardization [95]. Moreover, fatigue cracks in almost all cases (300 out of 304 specimens tested, combining both platforms) initiated from volumetric defects, indicating a dominating role of volumetric defects on the fatigue behavior of Ti-6Al-6V specimens.

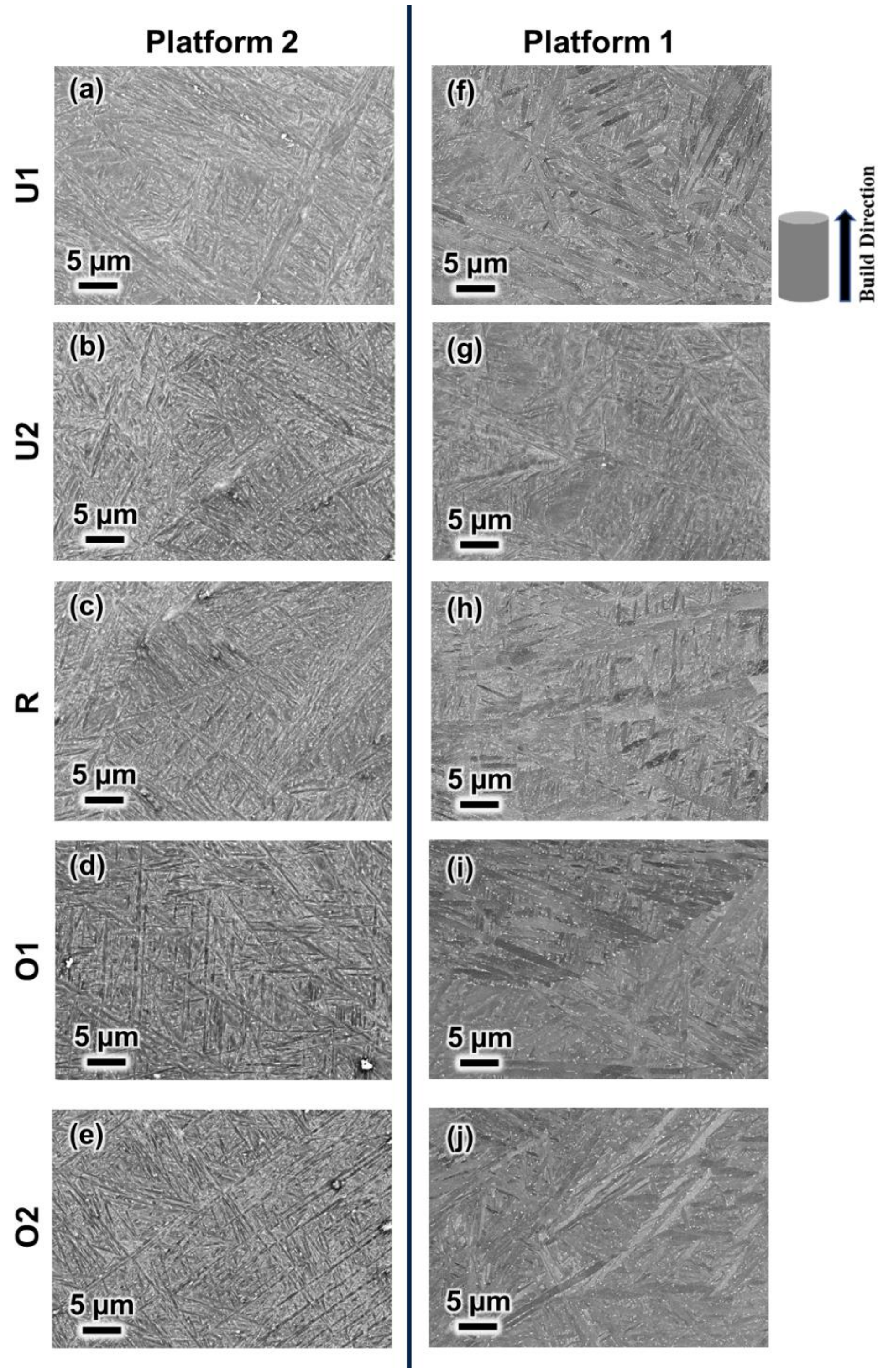

Figure 4-5. BSE micrographs of specimens fabricated using different processing conditions on both platforms.

4.3.2. Fatigue behavior

The stress-life fatigue plot of L-PBF Ti-6Al-4V specimens fabricated on Platform 2 is presented in Figure 4-6. Platform 2 specimens fabricated in both V and D orientations were plotted altogether since the stress-life behavior did not vary with the specimen orientation, as shown in Figure 4-6. The same trend had also been reported for L-PBF Ti-6Al-4V specimens fabricated on Platform 1 [93]. The blue dashed line in Figure 4-6, representing an envelope of fatigue data from Platform 1, encloses almost all data points from Platform 2, suggesting their overall stress-life behaviors could be identical due to the similar processing conditions. One data point from Platform 2, which appeared outside the envelope, was a case of fatigue crack initiation from multiple defects, resulting in a shorter fatigue life.

For Platform 2 specimens, the R specimens had the longest fatigue lives on average, whereas the U specimens had the shortest. This fatigue life ordering among different specimen sets appears to be in line with the maximum axis and √area of the largest defects for the respective processing conditions reported in Figure 4-3 (a)-(e) and Figure 4-4. For instance, among the largest defects of different conditions from Platform 2, the R condition had the smallest maximum axis and √area, whereas the U conditions had the largest maximum axis and √area. Among the processing conditions, the scatter in the fatigue lives in U conditions appeared to be higher compared to the R and O ones.

Fractography performed on all failed Platform 2 fatigue specimens using the SEM (selected fracture surfaces have been shown in Figure A6-17 in Appendix C) revealed that the vast majority of fatigue cracks (69 out of 72 specimens) were initiated from process-induced volumetric defects, either LoF or KH. In three cases, where fatigue cracks did not initiate from the volumetric defects, the presence of graphite particles was identified at the crack initiation sites using energy dispersive spectroscopy.

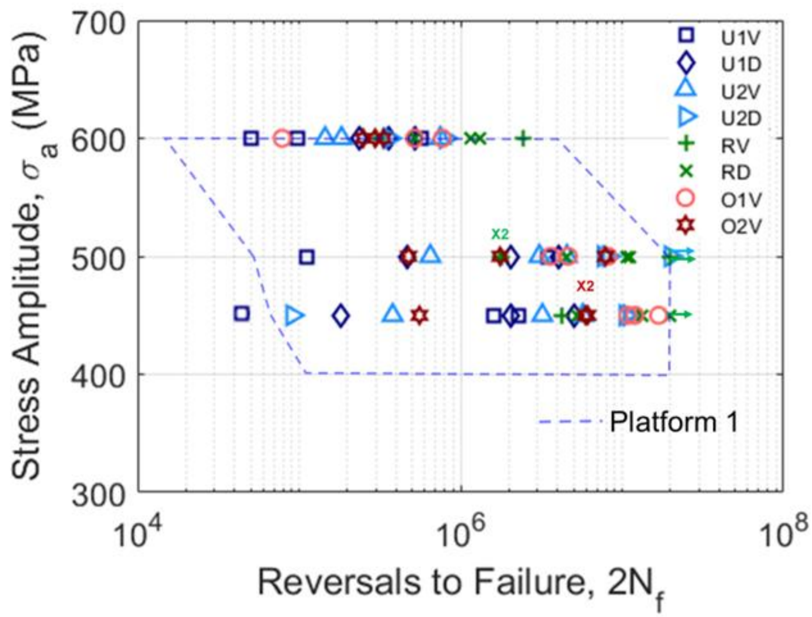

Figure 4-6. Stress-life fatigue plot of L-PBF Ti-Al-4V fabricated using different processing conditions. Fatigue data of different sets from Platform 2 are indicated by different markers, whereas the envelope of fatigue data from Platform 1[93] is shown using a blue dashed line.

4.3.3. Defect features critical to fatigue behavior

The variation in fatigue lives of Platform 2 specimens, presented in Section 4.3.2, was examined further utilizing the crack-initiating defects' morphological features obtained through fractography. Utilizing the defect size and distance from the free surfaces, crack-initiating defects from Platform 2 were classified into surface and internal ones, following the methodology discussed in Section 4.2.3. The stress-life bubble plots of both platforms, in which the size of the markers is proportional to the size of the crack-initiating defects, are presented in Figure 4-7 for each location. In previous studies [93,156], it was determined that among different defect size measures (Figure 4-2), $\sqrt{area}_{Murakami}$ was the appropriate for capturing the size effect of the surface defects, while $\sqrt{area_{MIC}}$ was effective for capturing both size and shape effect for internal defects. Accordingly, $\sqrt{area_{Murakami}}$ and $\sqrt{area_{MIC}}$ of surface and internal defects, respectively, are visualized in Figure 4-7 (a)-(b).

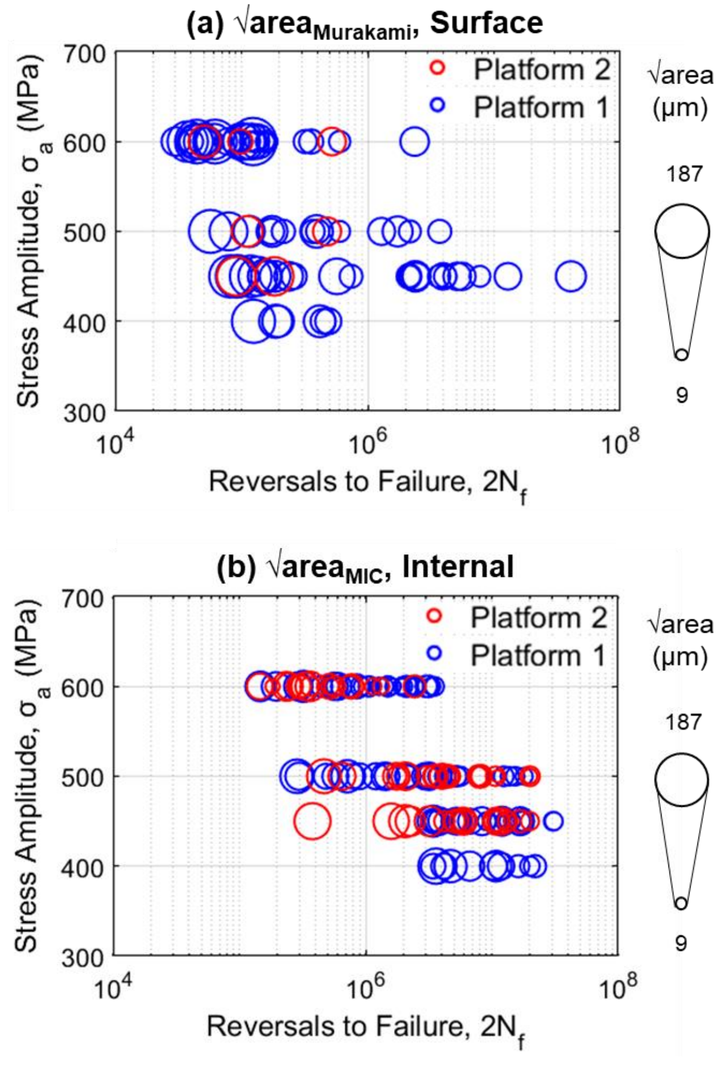

Figure 4-7. Stress-life fatigue plots of L-PBF Ti-6Al-4V specimens from both platforms showing the crack-initiating defect size for (a) surface and (b) internal defects.

Crack-initiating defect size influences the fatigue behavior of specimens from both platforms, as illustrated in Figure 4-7 (a)-(b). Specifically, larger crack-initiating defects generally resulted in shorter fatigue lives for both platforms. This trend was more pronounced for internal defects than surface defects. Only seven Platform 2 specimens failed due to crack initiations from surface defects (Figure 4-7 (a)), which made it challenging to observe the associated size effect.

In addition, the applicability of $\sqrt{area}_{MIC}$ as a size measure to internal crack-initiating defects for the Platform 2 specimens was further evaluated using the largest extreme value distribution (LEVD) [69,70,86]. The non-parametric Moments method [86,87] was applied to calculate the cumulative probability of the LEVD, formulated in terms of the reduced variate, Y_i, as:

$$Y_i = -\ln\left(-\ln\left(i/N+1\right)\right), \tag{4.1}$$

where i is the rank, and N is the total number of crack-initiating defects.

The probability plots of Y_i for $\sqrt{area}$ of internal crack-initiating defects and reversals to failure, $2N_f$, of specimens from both platforms are shown in Figure 4-8 (a) and Figure 4-8 (b)-(d), respectively. Surface defects were excluded in this analysis since there were not sufficient specimens that failed due to crack initiation from surface defects. When plotting the probability plots in terms of $\sqrt{area}_{MIC}$ (Figure 4-8 (a)), the crack-initiating defects were ranked based on the size (from smallest to largest), and when plotting the probability plots in terms of $2N_f$ (Figure 4-8 (b)-(d)), the crack-initiating defects were ranked based on $2N_f$ for each stress level (from shortest to longest $2N_f$). The plots indicated no significant difference in the distribution of both the $\sqrt{area}$ of crack-initiating defects and $2N_f$ between specimens from the two platforms, suggesting the distributions of defect size and fatigue life from one platform could be used to represent those from another platform with reasonable accuracy.

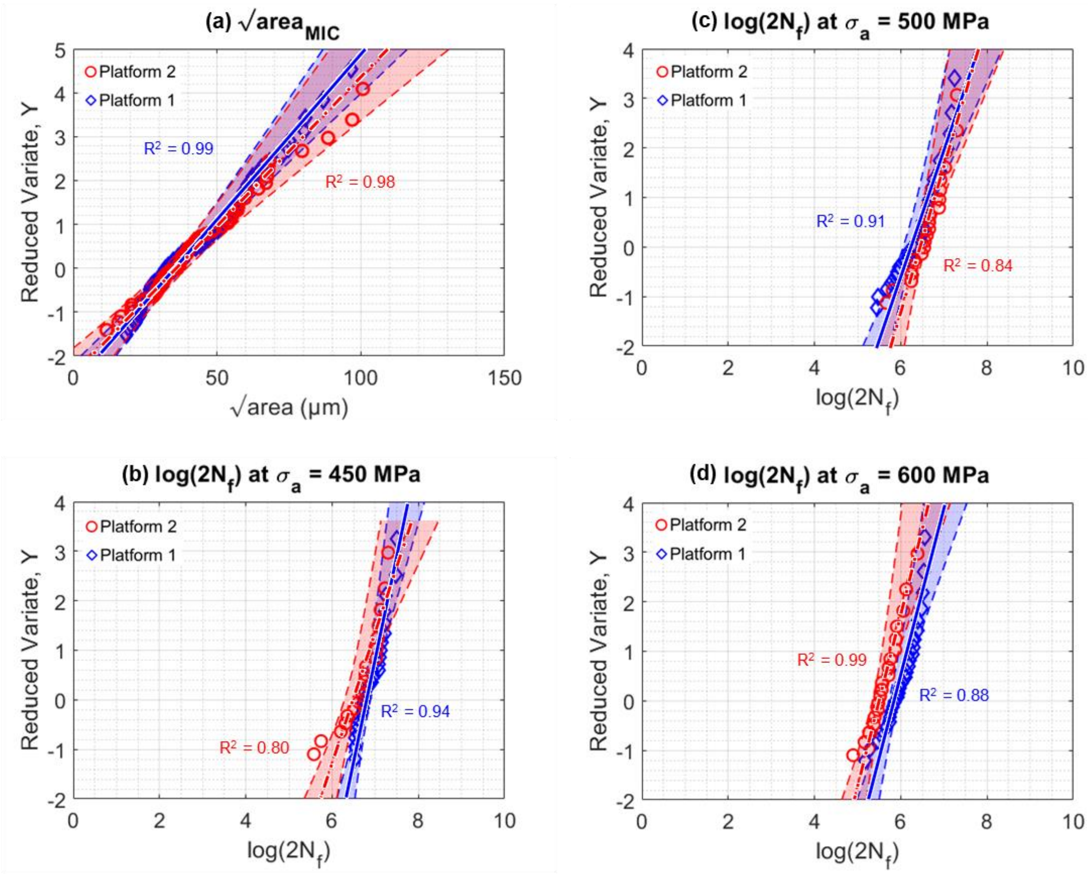

Figure 4-8. Probability plots showing the reduced variate for (a) internal crack-initiating defects' size and (b)-(d) the corresponding $\log(2N_f)$ at 450, 500, and 600 MPa, comparing both platforms. Shades indicate 95% confidence band.

4.4. Transferability of defect-fatigue relationships between platforms

4.4.1. Fatigue strength

The fatigue limit of a material in the presence of a crack or defect can be estimated using the Kitagawa-Takahashi (K-T) diagram, which is based on fracture mechanics principles [159–162]. This diagram expresses the fatigue limit as a function of crack-initiating defect size and thereby allows determination of a maximum safe operating σ_a for a component with a known defect size. To examine its cross-platform transferability, the fatigue limit curve for the K-T diagram was constructed using fatigue data of Platform 1 specimens and then cross-examined by Platform 2 fatigue data in terms of stress range, $\Delta\sigma$, and crack-initiating defect size, $\sqrt{area}$ (of a proper measure according to defects' location), as shown in Figure 4-9. This fatigue limit curve is referred to as the reference curve in the remainder of this article. The reference curve was constructed following the approach proposed by Shao et al. [20], utilizing the crack-initiating internal KH defects' size, their fatigue lives, and the tested stress levels of Platform 1 specimens. First, a log-linear relationship was identified between the fatigue-critical internal KH defects' size (i.e., $\sqrt{area}_{MIC}$, which ranged from 15 to 62 µm) and the cycles to failure, N_f, at each stress level. Next, σ_a-N_f curves were constructed for different defect sizes from 10 µm (smallest critical volumetric defect reported for L-PBF Ti-6Al-4V [53]) to 60 µm with 2 µm increments, through extrapolation or interpolation of the Nf-√areaMIC relationships. From the σa-Nf curves, σa corresponds to Nf = 107 cycles for each defect size was estimated and Δσ-√areaMIC curve, i.e., the reference curve, was then constructed (blue dashed line in Figure 4-9).

The cross-examination of the reference curve from Platform 1, which was constructed based on the internal defects, with the Platform 2 fatigue data, required the data to be processed so that the effect of defect location could be incorporated. This was because of fatigue failures observed for Platform 2 were from both internal and surface defects, and the growth rate of cracks initiated from surface defects being greater than those from the internal ones [23,24,37,156]. Accordingly, the surface defects' size in Platform 2 fatigue data were converted to internal equivalents following the procedure below.

Following Murakami's treatment of defects as cracks, the equivalent size of the surface defects was obtained by equating the stress intensity factor (SIF) range, ΔK, equations of surface and internal defects [26] as follows:

$$(\Delta K)_{surface} = (\Delta K)_{internal},$$

$$0.65 \cdot \Delta\sigma \sqrt{\pi\left(\sqrt{area}\right)_{surface}} = 0.5 \cdot \Delta\sigma \sqrt{\pi\left(\sqrt{area}\right)_{internal}},$$

$$\left(\sqrt{area}\right)_{surface} = \sqrt{area}_{Murakami}, \tag{4.2}$$

$$\left(\sqrt{area}\right)_{internal} = \sqrt{area}_{MIC},$$

where 0.65 and 0.5 are Murakami's location parameter [26], for surface and internal defects, respectively. The relationship between the size of internal and surface defects can be obtained after equating their ΔK as:

$$\left(\sqrt{area}\right)_{surface} = \left(\frac{0.65}{0.5}\right)^2 \left(\sqrt{area}\right)_{internal}. \tag{4.3}$$

Hence, an equivalent defect size corresponding to the defect's $\sqrt{area}$, $(\sqrt{area})_{eq}$, can be estimated as:

$$(\sqrt{area})_{eq} = \begin{cases} 1.69 \cdot \left(\sqrt{area}\right)_{surface} = 1.69 \cdot \sqrt{area}_{Murakami} \\ (\sqrt{area})_{internal} = \sqrt{area}_{MIC} \end{cases}. \tag{4.4}$$

Essentially, for internal fatigue-critical defects, their equivalent size was unchanged; only the size of the surface defects was converted.

The use of $(\sqrt{area})_{eq}$ could facilitate the direct comparison between the reference curve and the crack-initiating defect size irrespective of the location. Together with the reference curve from Platform 1, $\Delta\sigma$ vs. $(\sqrt{area})_{eq}$ data for Platform 2 are shown using markers in Figure 4-9. By convention of the K-T diagram, the region below/inside the reference curve is the "safe" region, and above/outside the curve is the "failed" region. The run-out data points from Platform 2 (shown using the green markers) were appearing in/near the "safe" region. While the majority of failed data points had appeared in the "failed" region, some failed data corresponding to the internal defects were found in the “safe” region. These corresponded to internal defects of highly elongated or branched shapes, which likely led to an underestimation of the defect size when measured using $\sqrt{area}_{MIC}$. Hence, the reference curve constructed using internal defects’ data from Platform 1 seemed to be applicable to the majority of the surface and internal defects’ data of Platform 2 specimens.

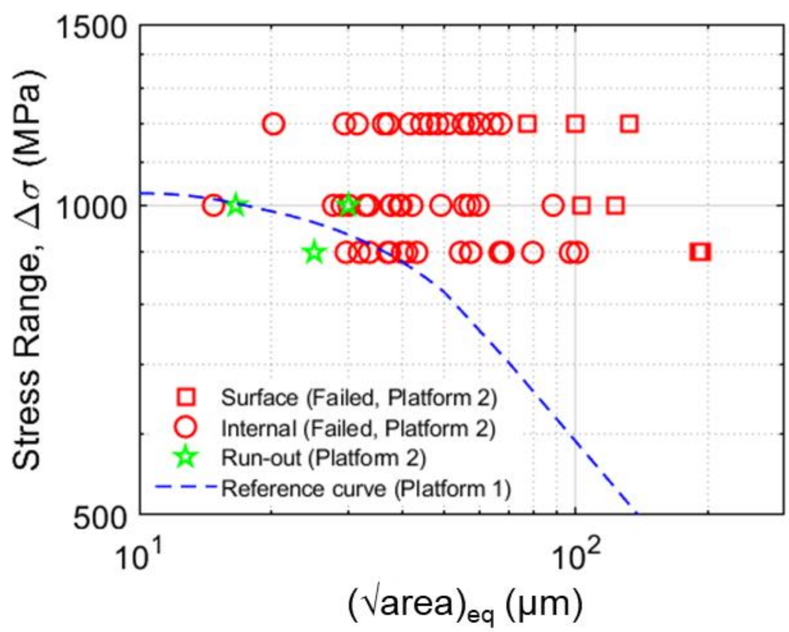

Figure 4-9. K-T diagram illustrating the variation of fatigue strength with crack-initiating defect size for L-PBF Ti-6Al-4V specimens, considering run-out at 10^7 cycles. The blue dashed line is a reference curve based on Platform 1 data and the data points are from Platform 2.

4.4.2. Shiozawa approach

For materials with fatigue cracks initiating from volumetric defects, Shiozawa equation [121,124] is widely used to describe the relationship between the driving force of crack-initiating defects (i.e., $\Delta K_{initial}$) and the corresponding defect-related lifetime (i.e., $N_f/\sqrt{area}$). Shiozawa equation is originally derived from the Paris-Erdogan equation [122,123] as:

$$\frac{da}{dN} = C(\Delta K)^m, \tag{4.5}$$

where C and m are the coefficient and the exponent, respectively [122,136]. Treating the fatigue-critical defect as an initial crack and integrating Eq. (4.5) from the initial crack size, $\sqrt{area_i}$, (which can be either $\sqrt{area_{Murakami}}$ or $\sqrt{area_{MIC}}$ depending on the defect's location) to the final crack size, $\sqrt{area_f}$, the Shiozawa equation (Eq. (4.6)) can be obtained as:

$$\Delta K_{initial} = \left[\frac{C(m-2)}{2}\right]^{-\frac{1}{m}} \left(\frac{N_f}{\sqrt{area_i}}\right)^{-\frac{1}{m}}, \tag{4.6}$$

where $\Delta K_{initial}$ is the initial SIF range at $\sqrt{area_i}$. $\Delta K_{initial}$ can be calculated using Eq. (4.7) as [53]:

$$\Delta K_{initial} = Y\Delta\sigma\sqrt{\pi\sqrt{area}_i}, \tag{4.7}$$

where Y is Murakami's location parameter (0.65 and 0.5 for surface and internal defects, respectively) [26]. A linear relationship between the $\Delta K_{initial}$ and $N_f/\sqrt{area_i}$ in a log-log plot is dictated by Eq. (4.6).

The Shiozawa plots generated using Platform 2 data are presented in Figure 4-10. Separate Shiozawa plots were constructed for surface and internal defects, since the plots generated using the Platform 1 data (reported in Ref. [156]) revealed that the fatigue cracks initiated from the surface and internal defects exhibited different growth rates, with the internal crack growth rates being slower than the surface ones [44,50,51]. The faster growth rate of cracks initiated from surface defects might be due to the embrittlement of the material at the freshly formed surface cracks resulting from the adsorption of gaseous molecules from the atmosphere or oxidation [24,36,125]. In the authors' prior work, the $\Delta K_{initial}$-$N_f/\sqrt{area_i}$ relationship has been constructed for Platform 1 [156]. To examine the applicability of this relationship on Platform 2, the best fit as well as the 90%, 95%, and 99% exceedance curves based on the Platform 1 data, are also shown in Figure 4-10. Paris-Erdogan constants corresponding to these curves of Platform 1 data, which have been reported in Ref. [156], are listed in Table 4-3. The best fit curves obtained from $\Delta K_{initial}$-$N_f/\sqrt{area_i}$ data essentially correspond to the 50% probability of survival (or 50% exceedance probability). For situations requiring higher reliability, exceedance curves for a given probability of survival can be constructed by offsetting the best fit curve [163]. For instance, an exceedance curve corresponding to a 90% probability indicated that 90% of cracks initiated from volumetric defects were expected to exhibit longer defect-related lifetime, $N_f/\sqrt{area_i}$, than what was represented by the curve.

Due to limited Platform 2 surface defect data (Figure 4-10 (a)), the cross-platform applicability of surface defects' $\Delta K_{initial}$-$N_f/\sqrt{area_i}$ relationship was inconclusive. For internal defects (Figure 4-10 (b)), fatigue data from Platform 2 seemed to spread on both sides of the best fit curve for Platform 1 data. In addition, 84%, 97%, and 100% of internal defects' data from Platform 2 exhibited longer defect-related lifetime than 90%, 95%, and 99% exceedance curves constructed based on the Platform 1 data, respectively (Figure 4-10 (b)). This suggested that the crack growth behavior of both platforms was similar, and the best fit and exceedance curves generated from Platform 1 data could be used for Platform 2 as well.

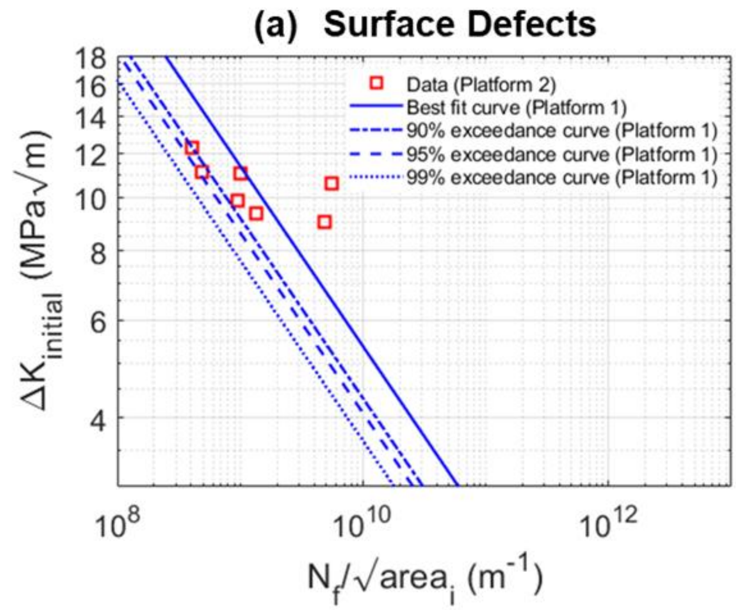

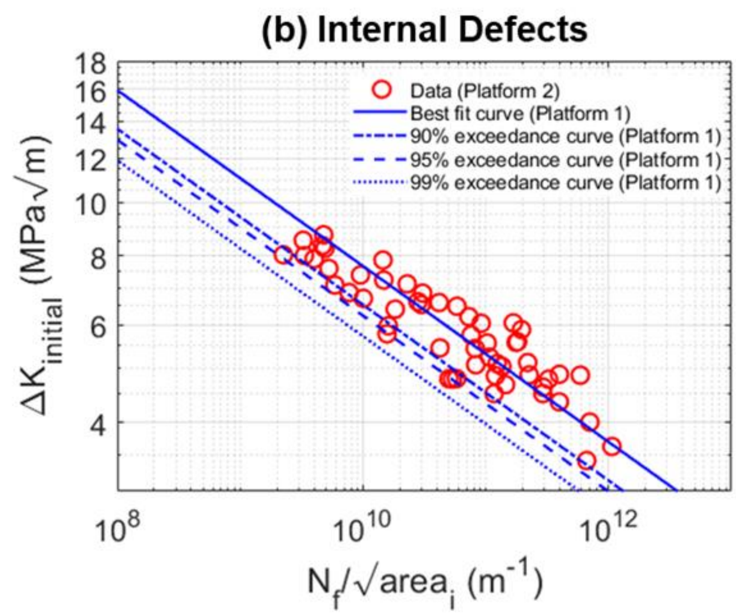

Figure 4-10. $\Delta K_{initial}$ vs. $N_f/\sqrt{area_i}$ plots for L-PBF Ti-6Al-4V specimens, with data points from Platform 2 and exceedance curves from Platform 1 data for (a) surface and (b) internal defects.

Table 4-3. Paris-Erdogan constants obtained from Shiozawa plots, based on Platform 1 data [156].

	Surface		Internal	
	C $\left(\frac{\mathrm{m/cycle}}{\left(\mathrm{MPa}\sqrt{\mathrm{m}}\right)^{\mathrm{m}}}\right)$	m	C $\left(\frac{\mathrm{m/cycle}}{\left(\mathrm{MPa}\sqrt{\mathrm{m}}\right)^{\mathrm{m}}}\right)$	m
Constants obtained from best fit curves	2.13×10^{-12}	3.07	1.28×10^{-16}	6.29
Constants obtained from 90% exceedance curves	4.14×10^{-12}	3.07	3.51×10^{-16}	6.29
Constants obtained from 95% exceedance curves	5.00×10^{-12}	3.07	4.67×10^{-16}	6.29
Constants obtained from 99% exceedance curves	7.12×10^{-12}	3.07	7.99×10^{-16}	6.29

4.4.3. Fatigue life estimation

In this section, fatigue lives of Platform 2 specimens were estimated using the Paris-Erdogan equation [122,123] (Eq. (4.5)) and the crack growth constants correspond to the best fit and 90% exceedance curves of the Shiozawa equation obtained from Platform 1 data (Table 4-3) [156]. For fatigue life estimation, the surface-exposed and embedded (including the near-surface and internal) defects were treated as semicircular and circular initial cracks, respectively; and the life was calculated by numerically integrating the Paris-Erdogan equation [122,123] with respect to the cracks' radii:

$$N_f = \int_{a_i}^{a_f} \frac{da}{C(\Delta K)^m}. \tag{4.8}$$

Where a_i and a_f are the initial and final radii of a fatigue crack. For surface and embedded defects, the a_i was calculated as the equivalent circle radius of their projected area on the loading plane:

$$a_i = \sqrt{\frac{2}{\pi}}\sqrt{area}_{Murakami} \text{ for surface-exposed defects,} \tag{4.9}$$

$$a_i = \sqrt{\frac{1}{\pi}}\sqrt{area}_{MIC} \text{ for embedded defects.} \tag{4.10}$$

Here, the incremental crack extension method was followed for numerical integration until a_f reached 2 mm. For surface-exposed cracks, ΔK during each crack increment was estimated using the analytical equations for semicircular cracks in a solid cylinder [134,135]. For embedded cracks, analytical ΔK equations for circular cracks in a round bar were used [138]. Since the cracks initiating from the surface and internal defects propagated at different crack growth rates (discussed in Section 4.4.2), separate constants were used to model cracks initiated from surface-exposed and embedded defects. Cracks initiated from surface-exposed defects were assumed to grow at surface crack growth rates until failure. On the other hand, a two-stage modeling approach was employed for cracks initiated from embedded defects: they initially propagated at internal crack growth rates until reaching the free surface of the specimens, after which they propagated at surface crack growth rates until failure [22].

Estimated vs. experimentally observed $2N_f$ of specimens from Platform 2, with scatter bands of ±3 and ±5, are shown in Figure 4-11. Note that only fatigue specimens that failed from single crack-initiating defects were included in this estimation exercise. The majority of the estimated versus experimentally observed data points were within the scatter band of ±5 while using the Paris-Erdogan material constants corresponding to the best fit curves (Figure 4-11 (a)), suggesting that the crack growth constants from Platform 1 data were appropriate to estimate the fatigue lives of specimens from Platform 2. The data of internal defects were appearing in both conservative (i.e., estimated $2N_f$ < experimentally observed $2N_f$) and non-conservative (i.e., estimated $2N_f$ > experimentally observed $2N_f$) sides, within the scatter band of ±5 (Figure 4-11 (a)). However, data of all surface defects were appearing in the conservative side, with one data point residing outside of the scatter bands of ±5. The outlier was investigated further and found to be a surface-exposed defect elongated towards the interior. For such defects, using $\sqrt{area}_{Murakami}$

for measuring defect size could overestimate the defect size, which might have contributed to conservative fatigue life estimation [26].

Fatigue life estimation using the material constants corresponding to the 90% exceedance curves demonstrated that the estimated fatigue lives are mostly conservative (Figure 4-11 (b)). Design of safety critical parts could benefit from a conservative approach to account for inherent uncertainty in material properties, thereby mitigating risks and avoiding costly failures. Overall, it could be concluded that the crack growth-based approaches, with the material constants from data of one platform could be used to estimate the fatigue life of specimens from another platform with reasonable accuracy, partially confirming the cross-platform transferability.

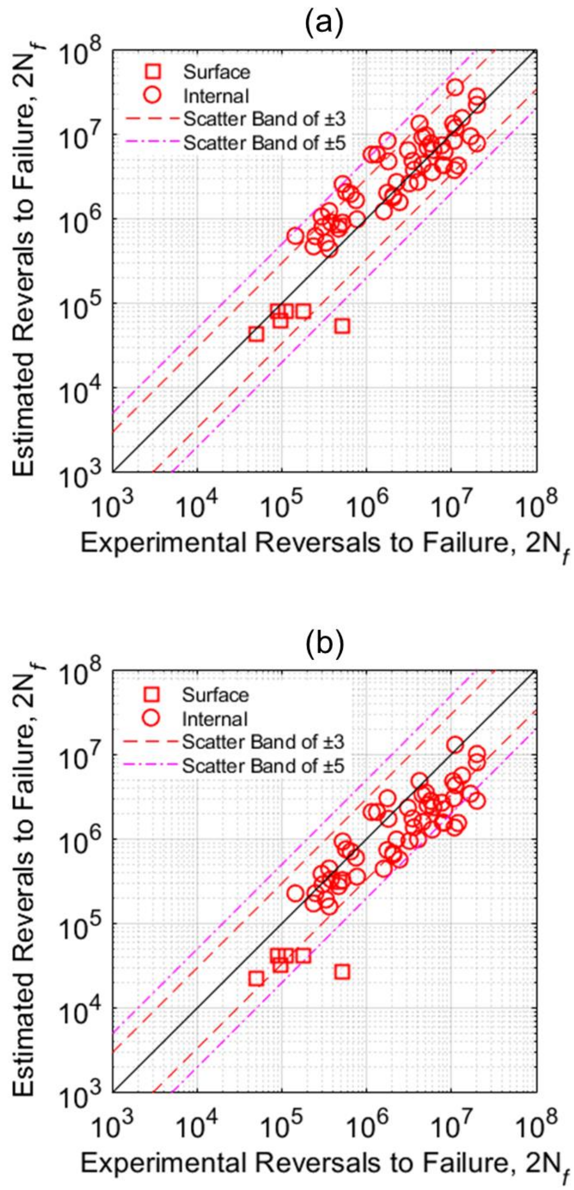

Figure 4-11. Estimated vs. experimentally observed $2N_f$ with scatter bands of ±3 and ±5 for L-PBF Ti-6Al-4V specimens fabricated on Platform 2 with material parameters from (a) best fit and (b) 90% exceedance curves of Platform 1 Shiozawa plots.

Further, a fatigue design curves has been constructed using the Paris-Erdogan material constants corresponding to the best fit curves of Platform 1 Shiozawa plot and largest crack-initiating surface defect observed for Platform 2 ($\sqrt{area}_{Murakami}$ = 115 μm) and shown in Figure 4-12. For comparison, a design curve for Platform 1, i.e., with the largest crack-initiating surface defect observed for that platform ($\sqrt{area}_{Murakami}$ = 172 μm), was also included. No fatigue data point fell to the left of the design curve for Platform 2, indicating that it represented the lowest possible fatigue life at all stress levels. In addition, both design curves captured the lower bound of fatigue lives using only the largest defect size and crack growth parameters from Platform 1. This suggested that a design curve based on the crack growth parameters from one platform could be reliably transferred to fatigue design of AM parts from another platform. With limited information from the platform of interest, such as the extreme defect size it can generate, the design curve could be further improved.

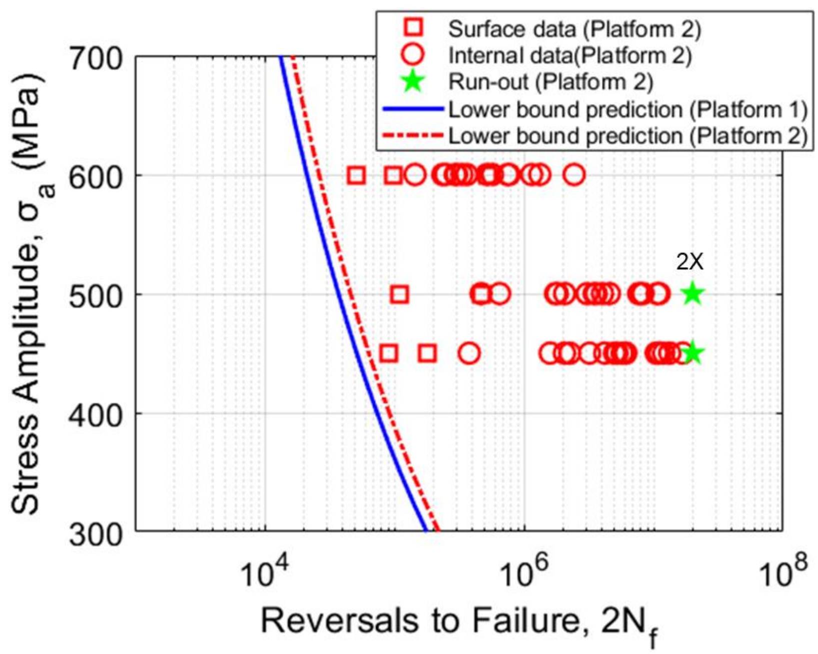

Figure 4-12**.** The lower bound fatigue design curves for L-PBF Ti-6Al-4V specimens based on the largest surface defect from both platforms, along with the experimentally observed data from Platform 2.

4.5. Conclusions

This study investigated the transferability of defect-fatigue relationships for Ti-6Al-4V specimens fabricated using two different laser powder bed fusion (L-PBF) platforms: the EOS M290 (referred to as Platform 1) and the Renishaw RenAM 500Q (Referred to as Platform 2). Specimens from RenAM 500Q platform were produced with similar adjustments in process parameters to those fabricated in the EOS M290 platform (as part of a previous work) to induce a wide range of defect morphologies and populations. The following conclusions were drawn from this study:

- The stress-life data of both platforms overlapped considerably, suggesting similar adjustments in processing conditions can lead to similar fatigue behavior across the L-PBF platforms for Ti-6Al-4V.
- The reference curve of the Kitagawa-Takahashi diagram, derived from the fatigue data generated from Platform 1, could be applied to estimate the fatigue limit of specimens fabricated on Platform 2.
- The fatigue crack growth parameters derived from Shiozawa curves generated from Platform 1 data could be used to accurately estimate the fatigue life of specimens fabricated from Platform 2.
- The lower bound fatigue life prediction curve constructed based on the largest defect and crack growth parameters from Platform 1 data could be reliably applied to the Platform 2 for design purposes.

5. Summary

The overall goal of this dissertation was to understand the effect of size, location, and shape of volumetric defects on fatigue behavior and estimate the fatigue life of L-PBF Ti-6Al-4V. This goal was achieved by completing several objectives in three separate studies, which have been discussed comprehensively in the preceding chapters (Chapters 2-4). A summary of these studies is presented in this chapter.

In chapter 2, the morphological features of process-induced volumetric defects that have the most impact on the fatigue behavior of L-PBF Ti-6Al-4V were identified. A comprehensive range of defect morphologies and populations was ensured using eight distinct process parameter sets and three build orientations during the fabrication of the specimens. The findings indicated that while defect size was the most critical feature influencing fatigue behavior for a given location, it alone could not fully account for variations in fatigue life. The effect of defect size on fatigue life was obscured by the defect's location and shape. After isolating the defects based on locations, near-surface defects were found to be most detrimental to the fatigue behavior, followed by surface-exposed and internal defects. Among internal defects with similar fatigue lives, circular defects were found to be smaller than their irregular counterparts, indicating that the existing defect size measurement did not adequately capture the effect of defect size. Moreover, the linear elastic finite element based analysis also has shown that unlike circular cracks, only a small fraction of irregular cracks' front, i.e., near their MICs experienced higher SIF values. Hence, a new defect size parameter, the $\sqrt{area}$ of the MIC, capturing both the size and shape of the volumetric defects, was introduced. This new defect size parameter exhibited a strong correlation with fatigue life compared to existing measures.

In chapter 3, fracture mechanics based fatigue life modeling for L-PBF Ti-6Al-4V was performed, with emphasis on the effect of volumetric defects' size, location, and shape. The predicted fatigue lives were validated against the experimentally observed fatigue lives. The cracks initiated from surface and internal defects experienced different crack growth rates, where surface defects resulted in significantly shorter fatigue lives due to higher crack growth rates. This suggests the need to quantitatively account for distinct growth rates in modeling and prediction. Hence, the short crack growth fatigue model, a novel fatigue life prediction approach that accounts for crack growth towards both the free surface and the interior, was proposed. This approach considered different SIF values at points of defects closer to the free surface and towards the interior, and could incorporate the change of fatigue crack growth behavior when the cracks initiated from internal defects reached the free surface. A probabilistic approach was utilized to determine the size of the largest possible defect for a given probability of failure. The fatigue design curve estimated with this defect size, using the proposed short crack growth model, has been shown to be a better estimate compared to design curves developed with conventional approaches for fatigue qualification.

In chapter 4, the transferability of defect-fatigue relationships was evaluated for L-PBF Ti-6Al-4V specimens of identical geometry and dimensions fabricated using two platforms: the EOS M290 and the Renishaw RenAM 500Q. Specimens from both platforms were fabricated using similarly varied process parameters to induce a wide range of volumetric defect morphologies and populations. The transferability of defect-fatigue relationships established for the specimens fabricated on the EOS M290 platform was tested and validated with those fabricated on the Renishaw RenAM 500Q platform. The stress-life data from both platforms overlapped, indicating that identical processing conditions can lead to similar defect characteristics and fatigue lives. The reference curve of the Kitagawa-Takahashi diagram generated using the fatigue data of EOS M290 was successfully applied to the fatigue data of RenAM 500Q. Paris-Erdogan constants derived from Shiozawa plots corresponding to the fatigue data from EOS M290 specimens could be successfully applied to the fatigue life prediction of the RenAM 500Q specimens. The validity of fatigue design curves constructed using the short crack growth model with parameters obtained from the EOS M290 platform specimens was verified with the data from the RenAM 500Q. Hence, defect-fatigue relationships obtained from one platform are transferable to another.

6. Appendices

6.1. Appendix A

6.1.1. Build layouts for tensile and fatigue specimens

The build layouts used for fabrication of laser powder bed fused, L-PBF, Ti-6Al-4V cylindrical rods with different part orientations are shown in Figure A6-1.

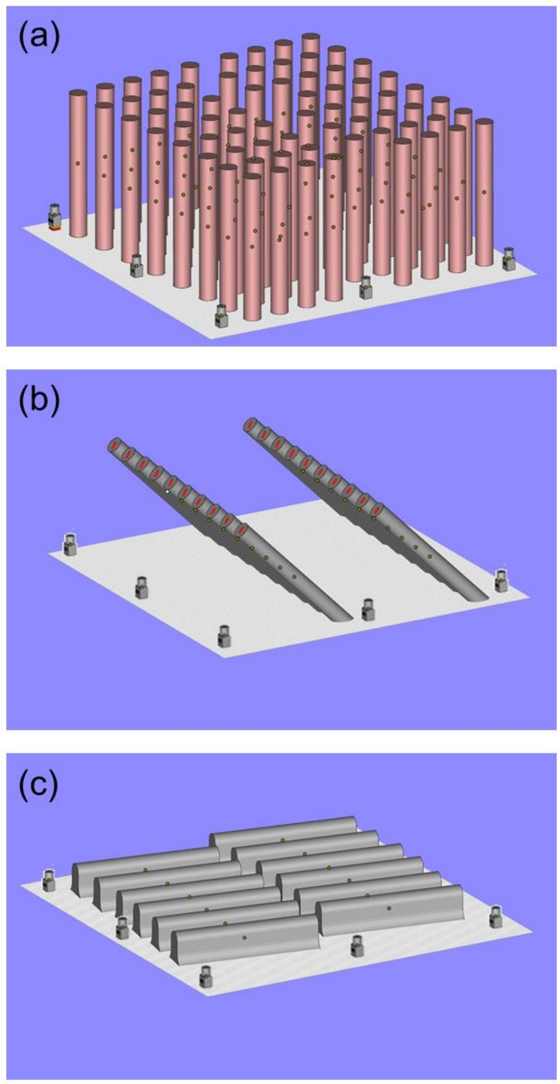

Figure A6-1. Build layout for L-PBF Ti6Al-4V specimens in (a) vertical, (b) diagonal, and (c) horizontal orientations.

6.1.2. Geometry and dimensions of tensile and fatigue specimens

The final geometry and dimensions of the tensile and fatigue L-PBF Ti-6Al-4V specimens are provided in Figure A6-2. These tensile and fatigue specimens were machined from cylindrical rods to final geometries according to ASTM E8 [77] and ASTM E466 [78] standards, respectively, and polished to a mirror finish before testing

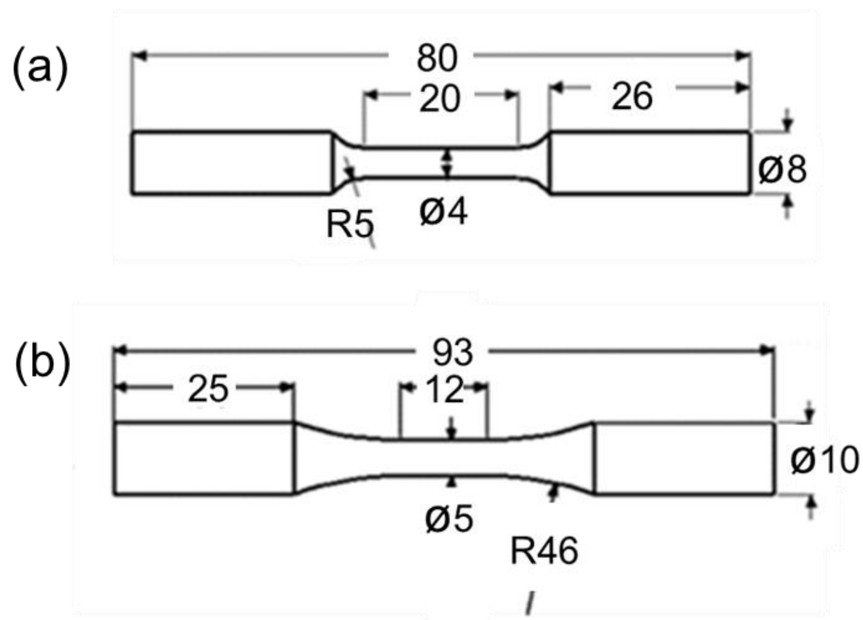

Figure A6-2. Geometries of (a) tensile and (b) fatigue L-PBF Ti-6Al-4V specimens. All the dimensions are in mm.

6.1.3. Microstructural analysis

Back-scattered electron, BSE, images of L-PBF Ti-6Al-4V fabricated using different process parameters, obtained in the longitudinal plane (i.e., the plane parallel to the long axis of the specimen) employing a scanning electron microscope, are shown in Figure A6-3. The methodology for sample preparation for BSE is described in the main manuscript, Section 2.2.2. As shown in Figure A6-3, α-laths of comparable sizes were observed in the microstructure of L-PBF Ti-6Al-4V specimens fabricated using different process parameters. No significant difference in the microstructure of L-PBF Ti-6Al-4V fabricated using different process parameters was observed.

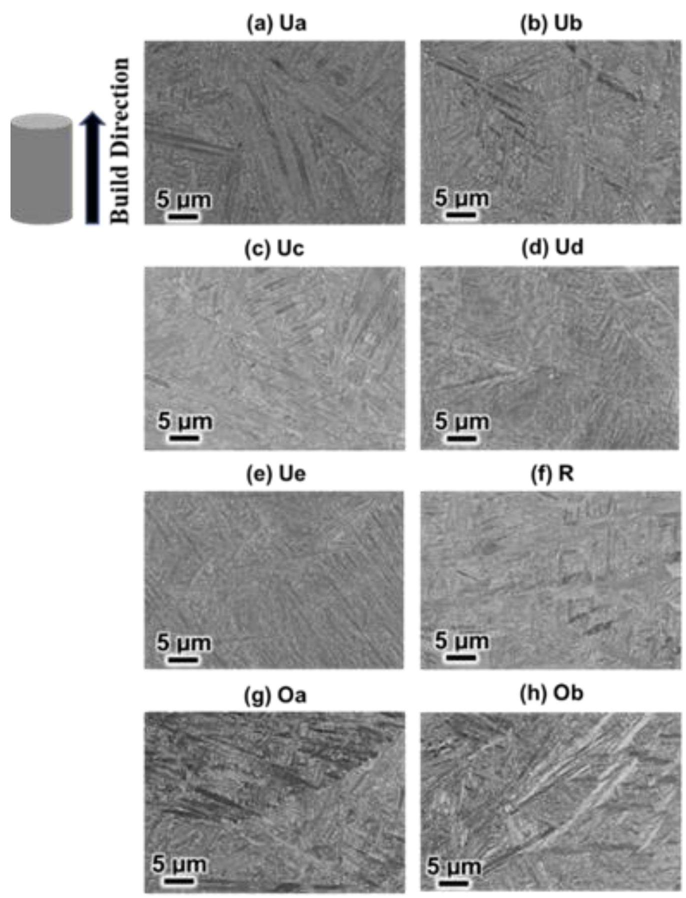

Figure A6-3. BSE micrographs of L-PBF Ti-6Al-4V specimens fabricated using different process parameters and in vertical orientation.

6.1.4. Chemical analysis

Chemical analysis results of the oxygen and nitrogen content of selected L-PBF Ti-6Al-4V specimens fabricated using different process parameters are shown in Figure A6-4. The oxygen and nitrogen content analyses were conducted employing the inert gas fusion method in a Bruker G8 Galileo instrument based on the ASTM F2924-14 standard [83].

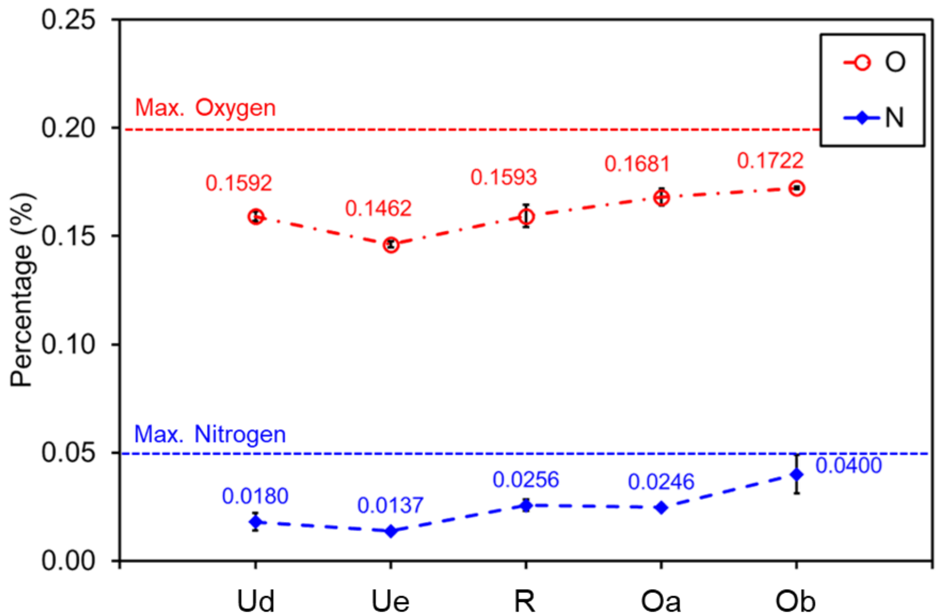

Figure A6-4. Chemical analysis of L-PBF Ti-6Al-4V specimens fabricated using different process parameters. The maximum nitrogen and oxygen contents shown in the figure by red-dashed and blue-dashed lines are based on the ASTM F2924-14 standard [83].

6.1.5. Tensile behavior

Fracture surfaces of selected failed tensile specimens of L-PBF Ti-6Al-4V specimens fabricated using different process parameters are shown in Figure A6-5. The tensile fracture surfaces of specimens from all sets exhibited similar features—contained dimples (indicated by red arrows) and shear lips, suggesting ductile fracture.

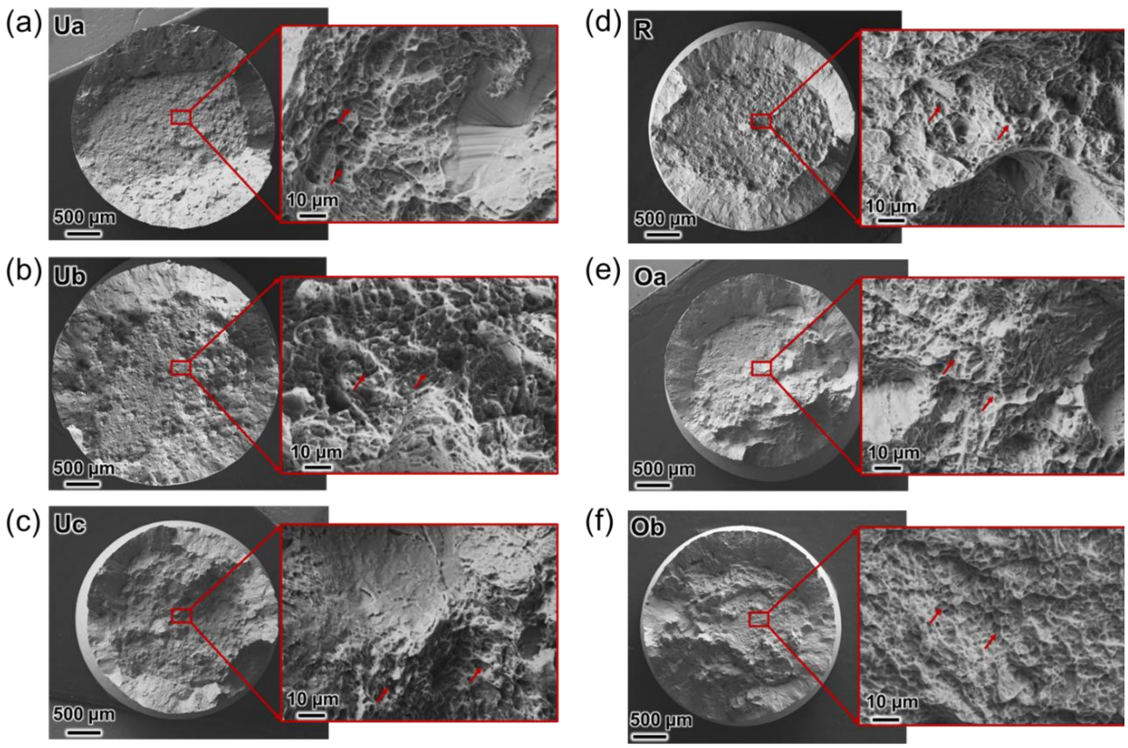

Figure A6-5. Tensile fracture surfaces of L-PBF Ti-6Al-4V specimens fabricated using different process parameters. The dimples are indicated by red arrows.

6.1.6. Defect size measurement approaches

Three different approaches were used to measure defect size: $\sqrt{area}_{Actual}$, $\sqrt{area}_{Murakami}$ [26] , and $\sqrt{area}_{MIC}$. For defect size measurements, defects were classified into surface-exposed, near-surface and internal categories following the methodology suggested by Wu et al. [64] (shown in Figure A6-6 (a) and also discussed in the main manuscript Section 2.3.3.1). Defects were classified as “surface defects” if they were either surface-exposed (e = 0) or near-surface ($\sqrt{area}_{eff} \geq e$). Internal defects were classified as those where $\sqrt{area}_{eff} \leq e$. Here, e represents the distance from the free surface to the nearest point of the defect, and $\sqrt{area}_{eff}$ denotes the square root of area enclosed between the curve enveloping the defect and free surface, as illustrated by the red dashed lines in Figure A6-6 (a). Figure A6-6 (b)-(d) illustrates the measurement approach followed for each defect location. $\sqrt{area}_{Actual}$ corresponds to the area enclosed within the two-dimensional, 2D, defect profile outline (enclosed by the purple line) obtained from the fracture surface. $\sqrt{area}_{Murakami}$ represents the area enclosed by the convex hull (enclosed by red lines) surrounding the defect profile. $\sqrt{area}_{MIC}$ corresponds to the area of the 2D profile’s maximum inscribed circle (enclosed by cyan line). $\sqrt{area}_{Actual}$, $\sqrt{area}_{Murakami}$, and $\sqrt{area}_{MIC}$ are indicated by purple, red, and cyan arrows, respectively in Figure A6-6.

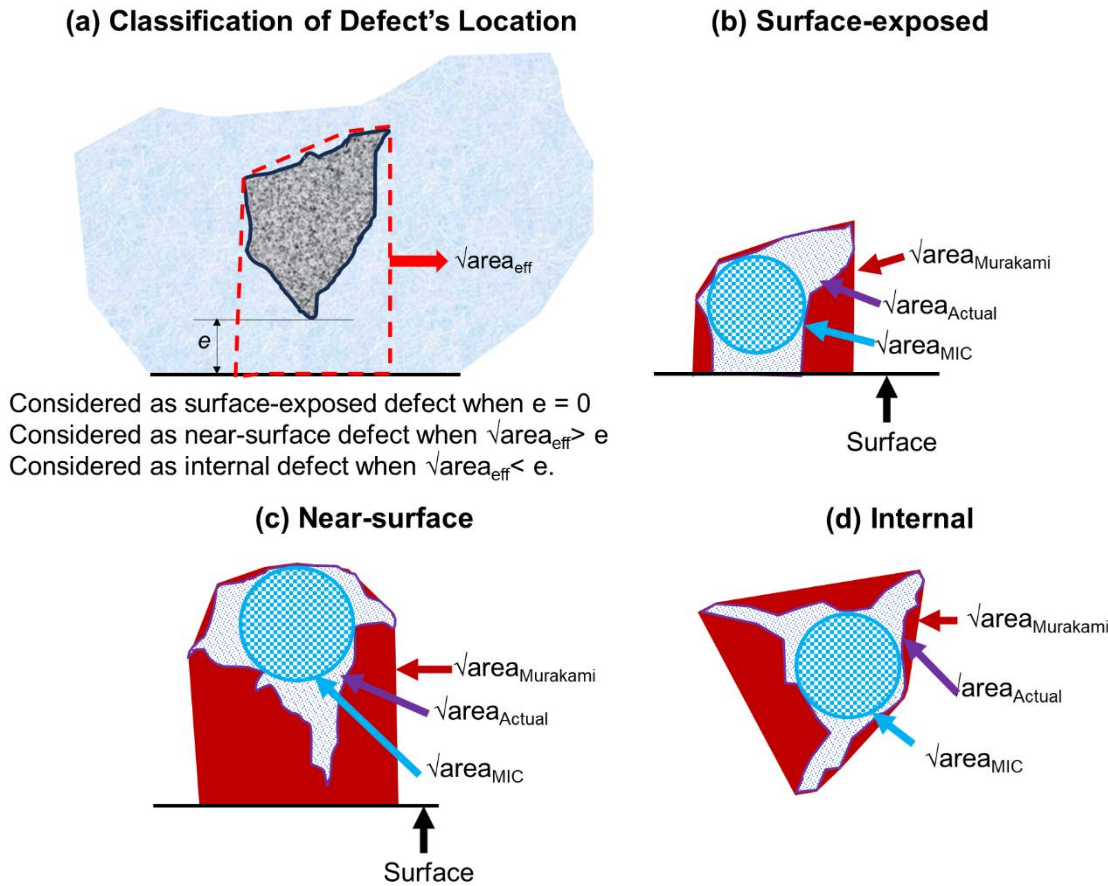

Figure A6-6. Schematic illustration of (a) defect classification based on their location; and different defect size measurement approaches used in this study for (b) surface-exposed, (b) near-surface, and (d) internal defects. √area$_{Actual}$, √area$_{Murakami}$, and √area$_{MIC}$ are indicated by purple, red, and cyan arrows, respectively.

6.1.7. Residual stress

Stress vs. depth plot showing the residual stress measurement on selected L-PBF Ti-6Al-4V specimens is shown in Figure A6-7. The residual stresses were measured at specific depth intervals from the free surface using a LXRD 20214. The measured results were corrected for stress gradient and material removal according to the SAE HS 784 standard [115].

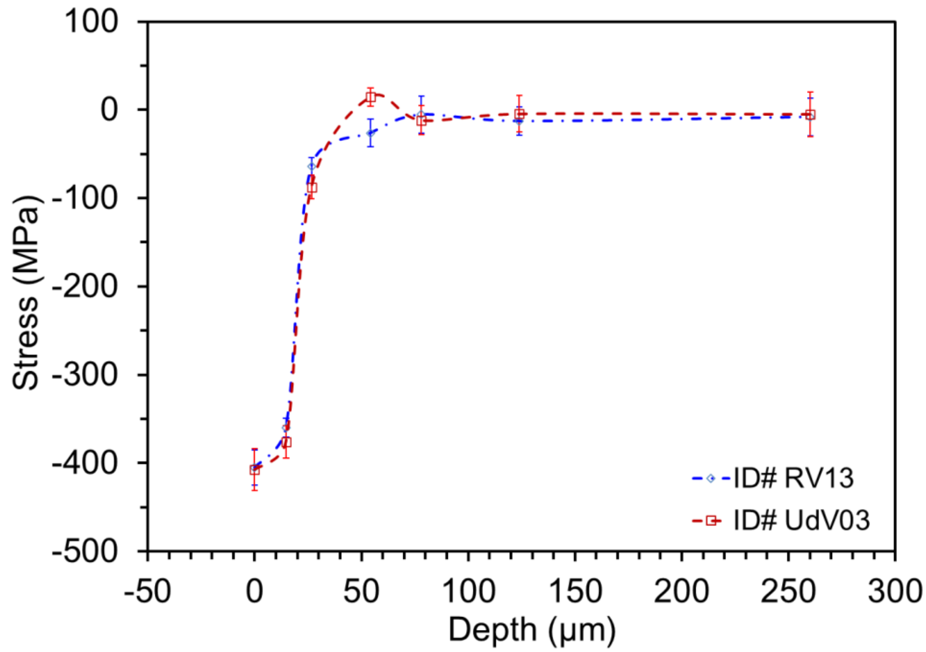

Figure A6-7. Measured residual stresses at different depths from surfaces for L-PBF Ti-6Al-4V specimens.

6.1.8. Linear elastic finite element analyses

Linear elastic finite element analyses were performed to calculate the stress intensity factor, SIF, of planar cracks whose shapes were extracted from the 2D profiles of the defects on the fractographs. The methodology used for analysis is described in Section 2.2.4 of the main manuscript and illustrated in Figure A6-8.

Additional images visualizing the distribution of normalized SIF on planar cracks whose shapes are identical to the 2D profiles of the respective defects (first column) and the normalized SIFs as a function of distance along the crack front (second column) are shown in Figure A6-9**.** The crack geometries were obtained from the fracture surfaces, and the numerical simulations were performed using the methodologies discussed in Section 2.2.4 of the main manuscript.

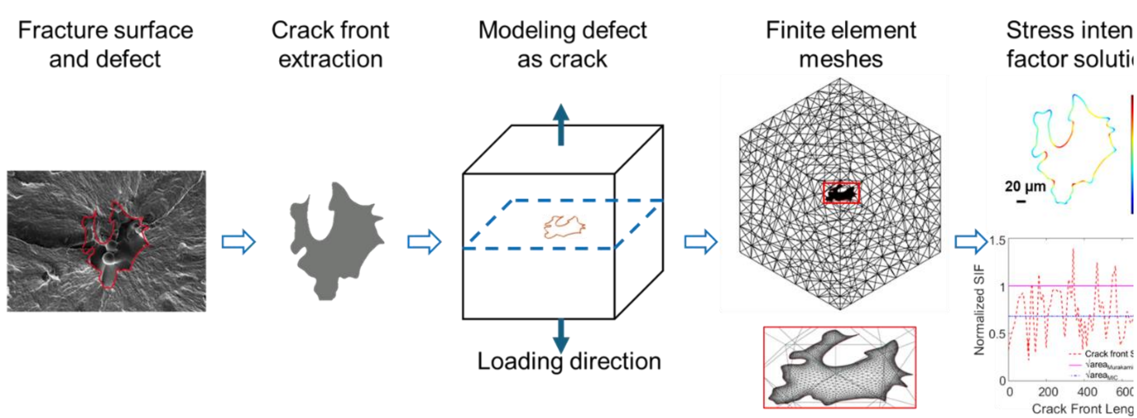

Figure A6-8. The simulation methodology used to calculate SIF considering the defect contours as 2D cracks.

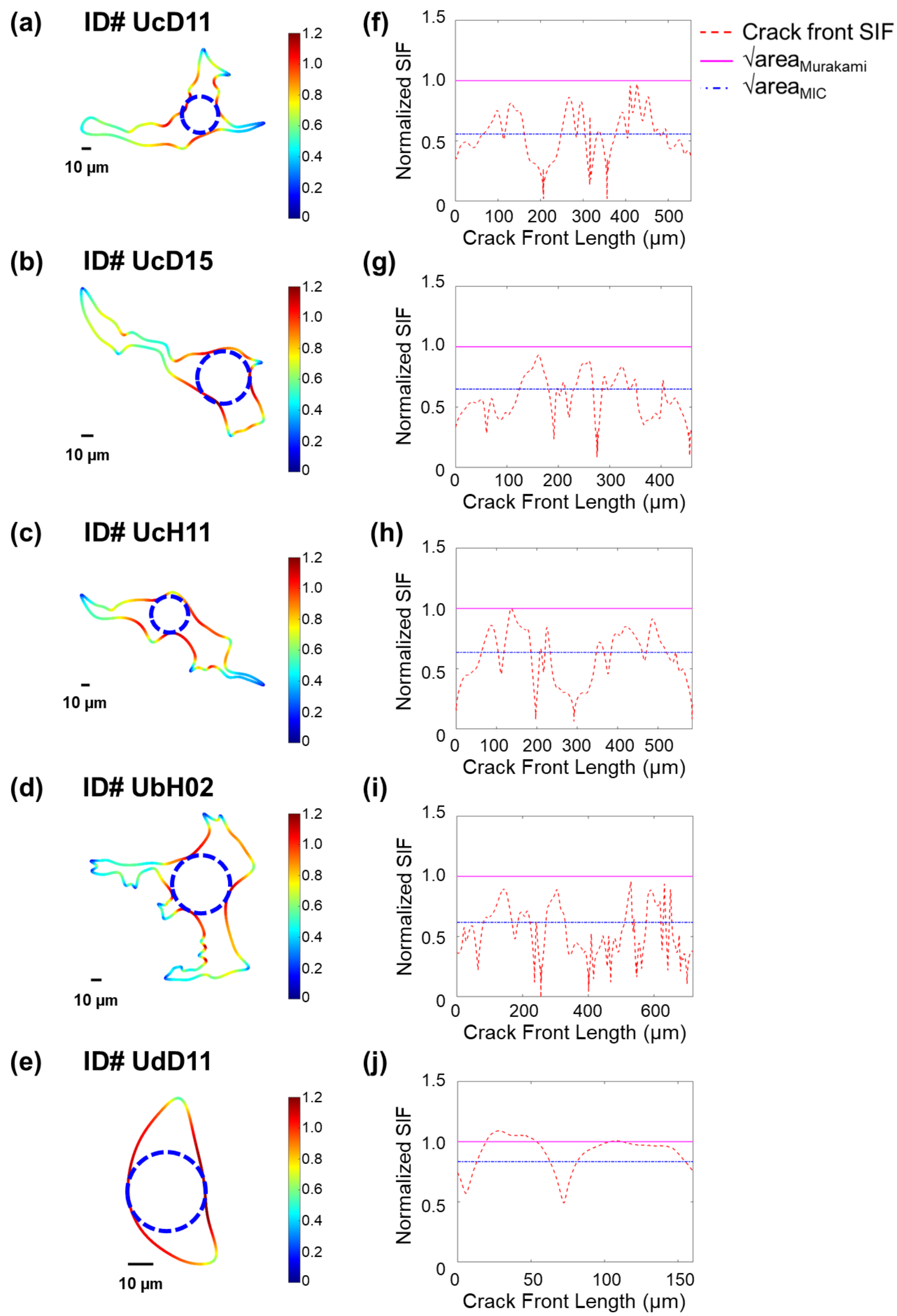

Figure A6-9. (a)-(e) SIFs obtained from the finite element analysis are superimposed on the defect profiles to illustrate the regions of the crack experiencing higher SIFs and (f)-(j) normalized SIFs along the crack front and SIFs estimated using Eq. (2.2) of the main manuscript. MIC are drawn with blue dot-dashed lines in (a)-(e).

6.1.9. Probability plots of defects

The various measurements of defect size were ranked from smallest to largest and then the largest extreme value distribution, LEVD, [70] was calculated using the non-parametric Moments method [87,88] in terms of the probability density functions, PDF, as:

$$PDF\ (x) = 1/\delta[\exp\left(-(\sqrt{area} - \lambda)/\delta\right] \times \exp\left[-\exp\left(-(\sqrt{area} - \lambda)/\delta\right]\right) \quad \text{(A1)}$$

where δ and λ are scale and location parameters, respectively, which were determined using the non-parametric Moments method.

The probability plots of irregular and circular defects using three different size measures, i.e., $\sqrt{area}_{Actual}$, $\sqrt{area}_{Murakami}$, and $\sqrt{area}_{MIC}$, in terms of Y_i, and the corresponding probability density functions are shown in Figure A6-10. In addition, the probability density plots of reversals to failure, $2N_f$, for irregular and circular defects are shown in Figure A6-11. No significant difference in fatigue lives between irregular and circular defects is observed in Figure A6-11, which suggests the defect size distributions should also be identical. While the distribution of defect sizes estimated using $\sqrt{area}_{Actual}$ and $\sqrt{area}_{Murakami}$ showed significant differences between circular and irregular defects (see Figure A6-10 (a)-(d)), the defect size estimated using $\sqrt{area}_{MIC}$ exhibited minimal difference (see Figure A6-10 (e)-(f)). This could be because the $\sqrt{area}_{Actual}$ and $\sqrt{area}_{Murakami}$ do not account for the influence of defect shape; however, $\sqrt{area}_{MIC}$ somewhat accounts for such defect shape influence.

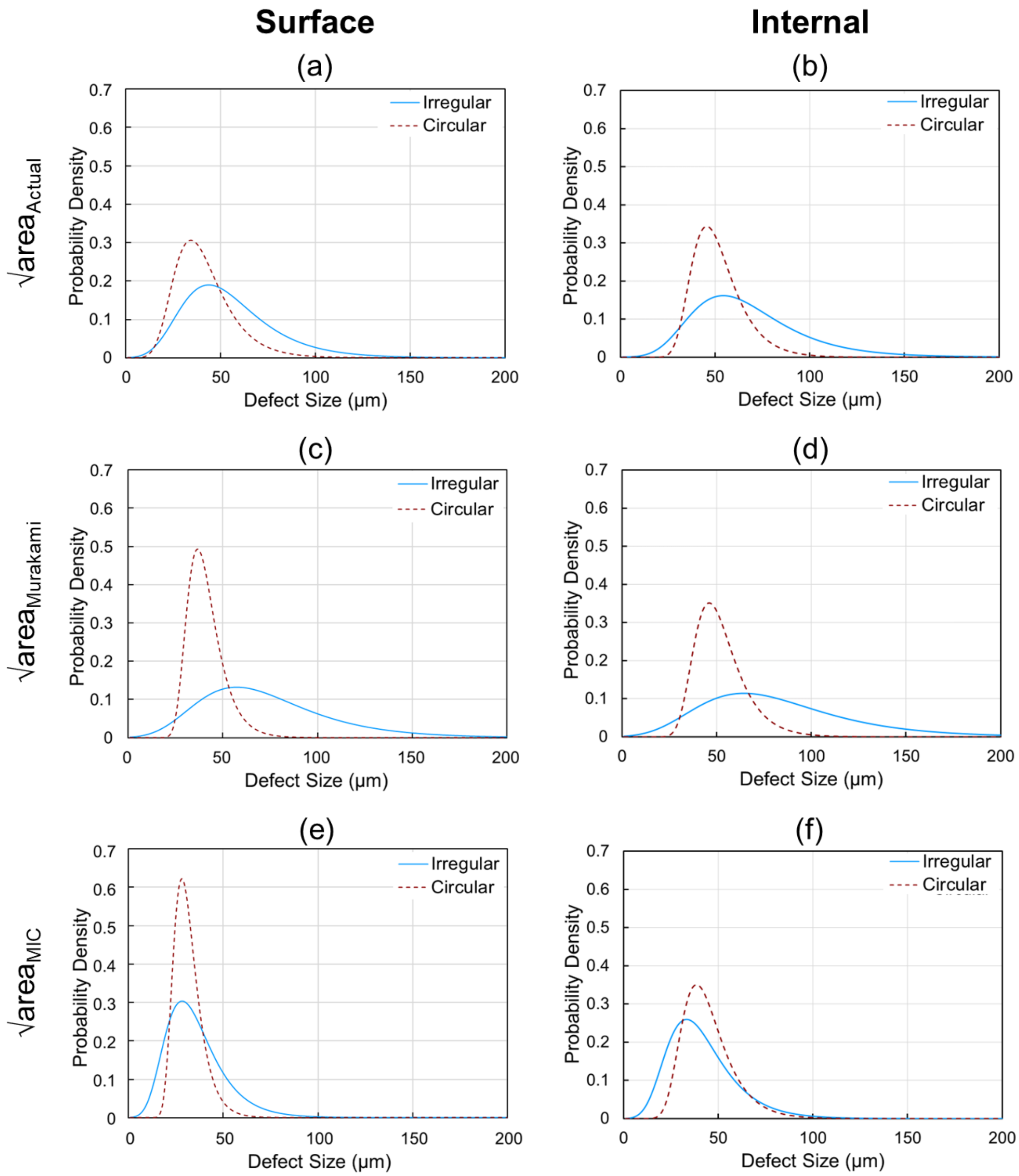

Figure A6-10. Probability density distribution with respect to crack initiating defect size measured using different defect size parameters: (a)-(b) $\sqrt{area}_{Actual}$, (c)-(d) $\sqrt{area}_{Murakami}$, and (e)-(f) $\sqrt{area}_{MIC}$. Surface defects include both surface-exposed and near-surface ones.

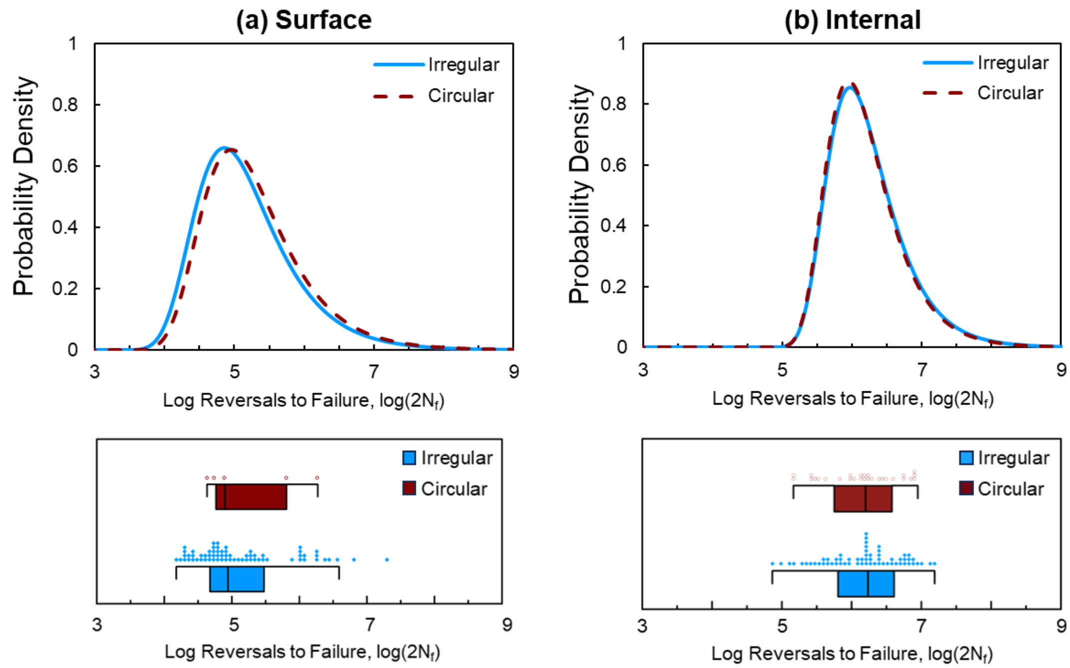

Figure A6-11. Probability density distribution of $2N_f$ along with box plots for (a) surface and (b) internal crack-initiating defects. Surface defects include both surface-exposed and near-surface ones.

6.2. Appendix B

6.2.1. Final geometry of fatigue specimen

Laser powder bed fused (L-PBF) Ti-6Al-4V rods were machined to the fatigue specimens following the ASTM E466 standard [78]. The final geometry and dimensions of the fatigue specimens are provided in Figure A6-12. The fatigue specimens were tested after they were polished to a mirror finish.

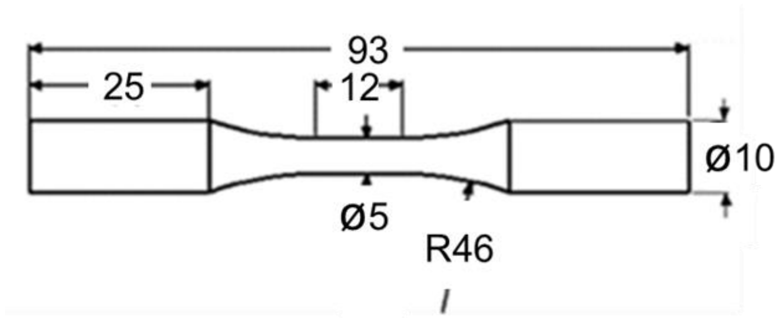

Figure A6-12. Geometries of fatigue L-PBF Ti-6Al-4V specimens. All the dimensions are in mm.

6.2.2. Residual stress

At specific depth intervals from the free surface of the selected fatigue specimens, the normal components of residual stress (RS) acting along the loading direction were measured using an LXRD 20214, following the SAE HS 784 standard [115], and reported in the previous study of the authors [93]. Stress vs. depth plot showing the RS measurement on selected L-PBF Ti-6Al-4V specimens is shown in Figure A6-13.

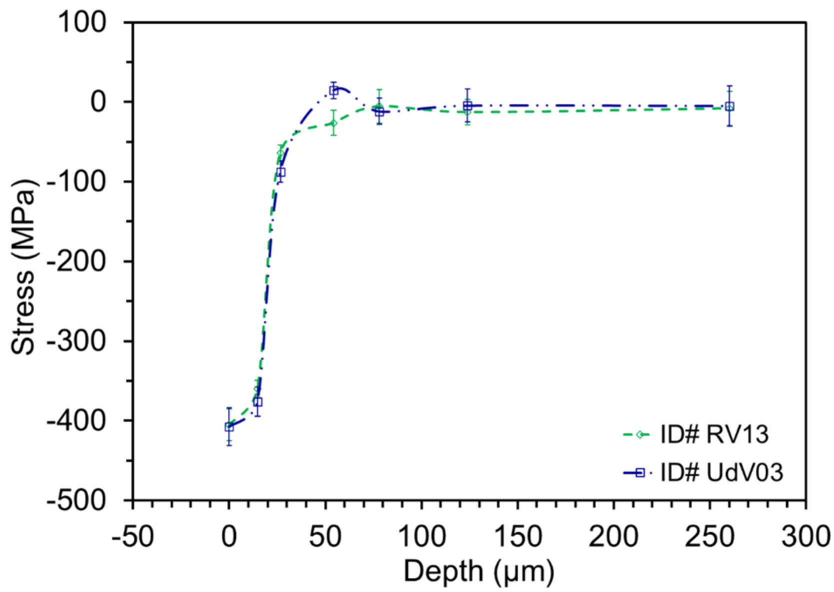

Figure A6-13. Measured RS at specific depths from free surfaces for selected L-PBF Ti-6Al-4V specimens, reported in Ref. [93].

6.2.3. Calculation of Δσ incorporating residual stress

Effective stress range, $\Delta\sigma$, in the presence of RS was estimated using the approach described in [108,164]. For this, firstly, the effective stress ratio, R_{eff}, was calculated as:

$$R_{eff} = \frac{\sigma_{min}^{eff}}{\sigma_{max}^{eff}}, \tag{A2}$$

where σ_{max}^{eff} is the maximum effective stress and σ_{min}^{eff} is the minimum effective stress considering the RS. σ_{min}^{eff} and σ_{max}^{eff} were calculated as:

$$\sigma_{min}^{eff} = \frac{\Delta\sigma}{1 - R_\sigma} . R_\sigma + RS, \tag{A3}$$

$$\sigma_{max}^{eff} = \frac{\Delta\sigma}{1 - R_\sigma} + RS, \tag{A4}$$

where R_σ is the stress ratio. RS was measured radially from the surface of the specimens and collected from the previous study of the authors [93]. For the following step, based on the calculated R_{eff}, $\Delta\sigma$ could be calculated using the following equation [14]:

$$\Delta\sigma_{(R_\sigma \neq 0)} = \Delta\sigma_{(R_\sigma = 0)}(1 - R_\sigma)^{(1-\gamma)}, \tag{A5}$$

where γ is the material constant, the value of which (i.e., 0.5431) was collected from [165].

6.3. Appendix C

6.3.1. Geometry of tensile specimen and tensile testing

Cylindrical laser powder bed fused (L-PBF) Ti-6Al-4V bars were machined to the final geometries of the tensile specimens in accordance with the ASTM E8 standard [77]. The final geometry and dimensions of the tensile are presented in Figure A6-14.

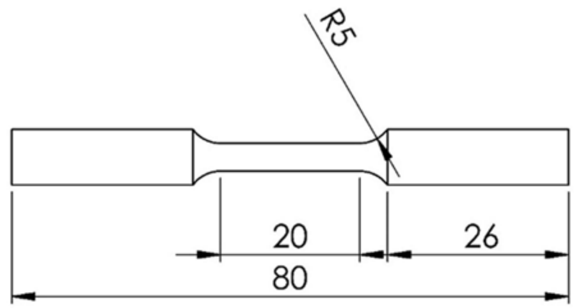

Figure A6-14. Dimensions and the geometry of tensile L-PBF Ti-6Al-4V specimen investigated in this study. All dimensions are in mm.

Quasi-static tensile testing of L-PBF Ti-6Al-4V specimens fabricated with different process parameters was performed at room temperature using an MTS servo-hydraulic testing system. A mechanical extensometer was employed to capture the strain experienced by the specimens during testing up to the point of final fracture. The percentage elongation to failure, %El, was manually calculated by measuring the change in length between the gage section markings before and after testing. Tensile testing of at least three specimens per set was conducted to ensure repeatability.

6.3.2. Tensile behavior

Column charts illustrating the yield strength, S_y, ultimate tensile strength, S_u, and %El of L-PBF Ti-6Al-4V specimens fabricated on both Platform 1 and Platform 2 using varying processing conditions and different part orientations are shown in Figure A6-15. The tensile behavior of Platform 2 specimens exhibited similar trends to those of Platform 1 specimens, as reported in the previous study by the authors [93]. In Figure A6-15, specimens from both underheated (U) and recommended (R) sets demonstrated comparable tensile properties, including Sy, Su, and %El. This indicated that the variation of defect content across the specimen sets (see Error! Reference source not found. in the main manuscript) did not appear to correlate with tensile b ehavior, despite the significantly higher defect content and lower part density of U1 specimens from Platform 2 compared to the R specimens.

However, the overheated (O) specimens from both O1 and O2 sets exhibited slightly higher tensile strengths (both Sy and Su) than the specimens in the other sets. This increase might be attributed to the higher oxygen and nitrogen content (see Section 6.3.3 for detailed chemical analysis), a result of excessive energy input during fabrication. Higher levels of oxygen and nitrogen likely contributed to the formation of interstitial oxygen and nitrogen, which marginally enhanced tensile strengths [81,82]. This phenomenon of the slight increase in tensile strengths of O specimens from Platform 2 is similar to the observations from Platform 1 specimens [93].

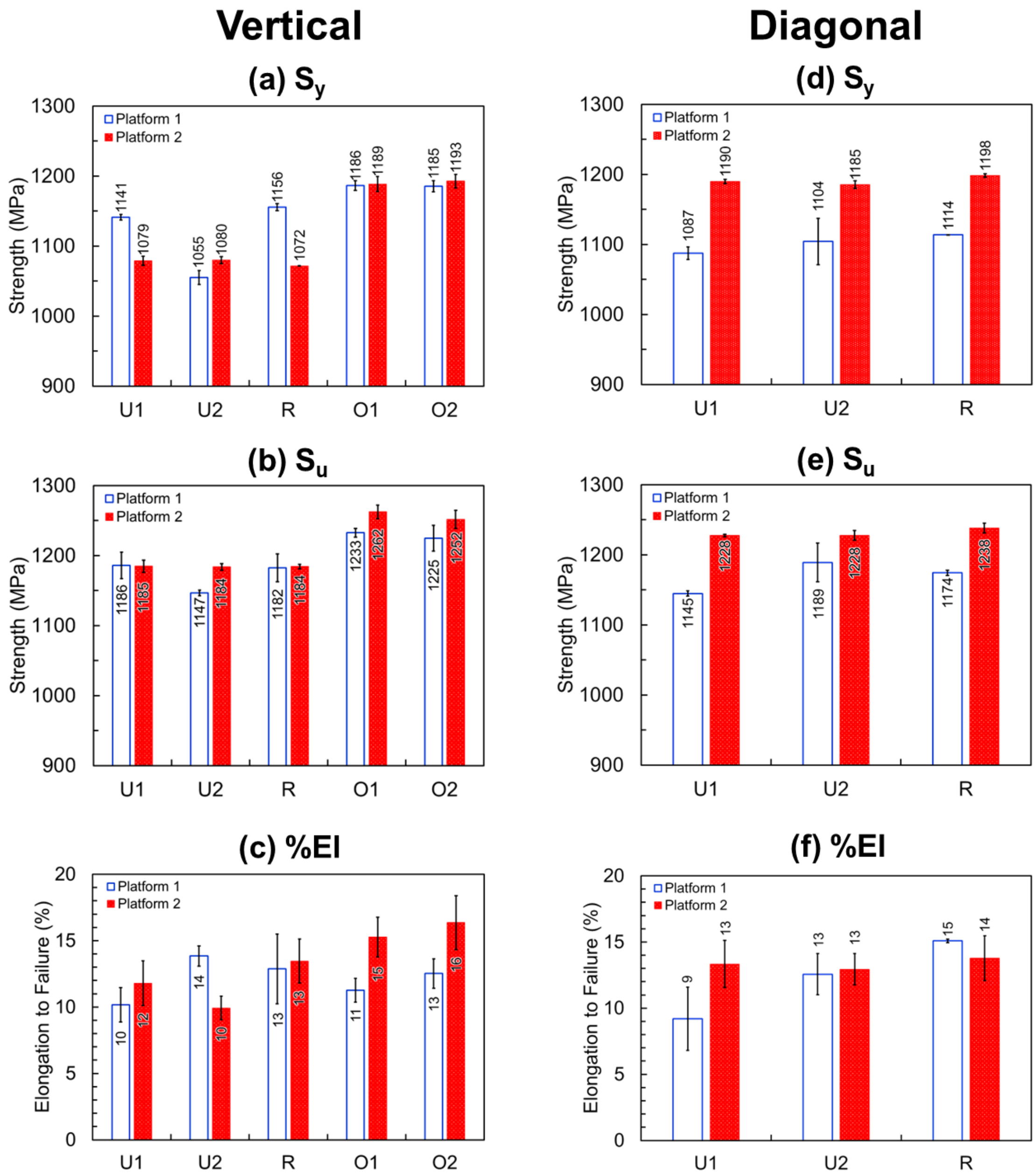

Figure A6-15. Column charts comparing the tensile properties between Platform 1 and Platform 2 L-PBF Ti-6Al-4V specimens fabricated using different processing conditions in (a)-(c) vertical and (d)-(f) diagonal orientation.

6.3.3. Chemical analysis

The Oxygen and nitrogen contents of selected L-PBF Ti-6Al-4V specimens fabricated using different processing conditions on both platforms, as determined through chemical analysis, are shown in Figure A6-4. The measurements were performed using a Bruker G8 Galileo instrument in accordance with the ASTM F2924-14 standard [83], employing the inert gas fusion method.

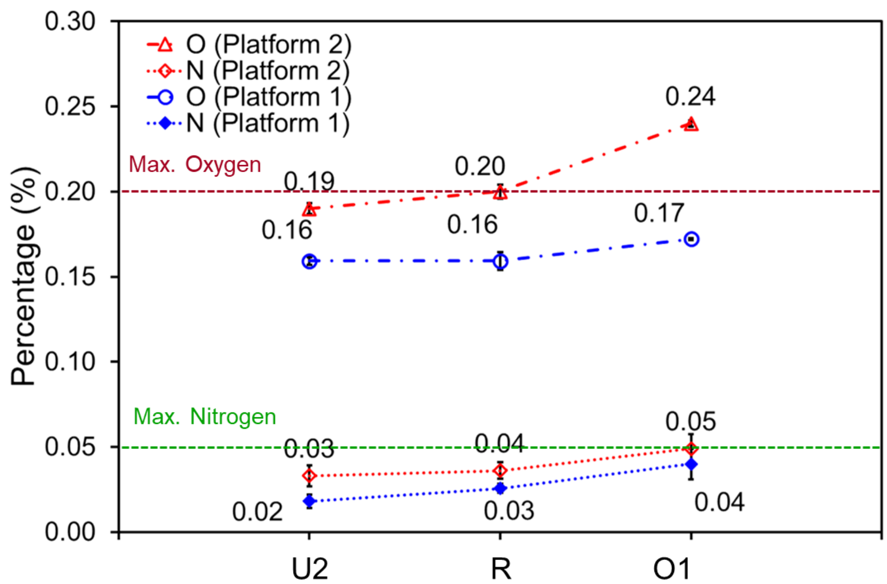

Figure A6-16. Chemical analysis of the oxygen and nitrogen content in L-PBF Ti-6Al-4V specimens. The horizontal dashed lines represent the maximum oxygen and nitrogen content based on the ASTM F2924-14 standard.

The maximum oxygen and nitrogen content, as recommended by the ASTM F2924-14 standard [83], are indicated using red and green dashed lines, respectively, in Figure A6-16. Consistent with the observations for Platform 1 specimens, the O1 specimens from Platform 2 exhibited slightly higher oxygen and nitrogen content than the R ones. This increase in interstitial oxygen and nitrogen content may be attributed to the higher energy input utilized during the fabrication of the O specimens, which likely enhanced the dissolution of oxygen and nitrogen within the α-laths of Ti-6Al-4V [81,82]. The presence of these interstitial elements is known to contribute to an increase in tensile strengths by impeding the motion of dislocations [81,82].

6.3.4. Fatigue fractography

Fractography images of selected specimens fabricated using different process parameters are shown in Figure A6-17. Apart from three instances, fatigue cracks from all failed specimens were initiated by process-induced volumetric defects. Actual √area of the crack-initiating defects on the plane perpendicular to the loading axis, $\sqrt{area}_{Actual}$, of each fracture surface is shown on the right side of each panel in Figure A6-17.

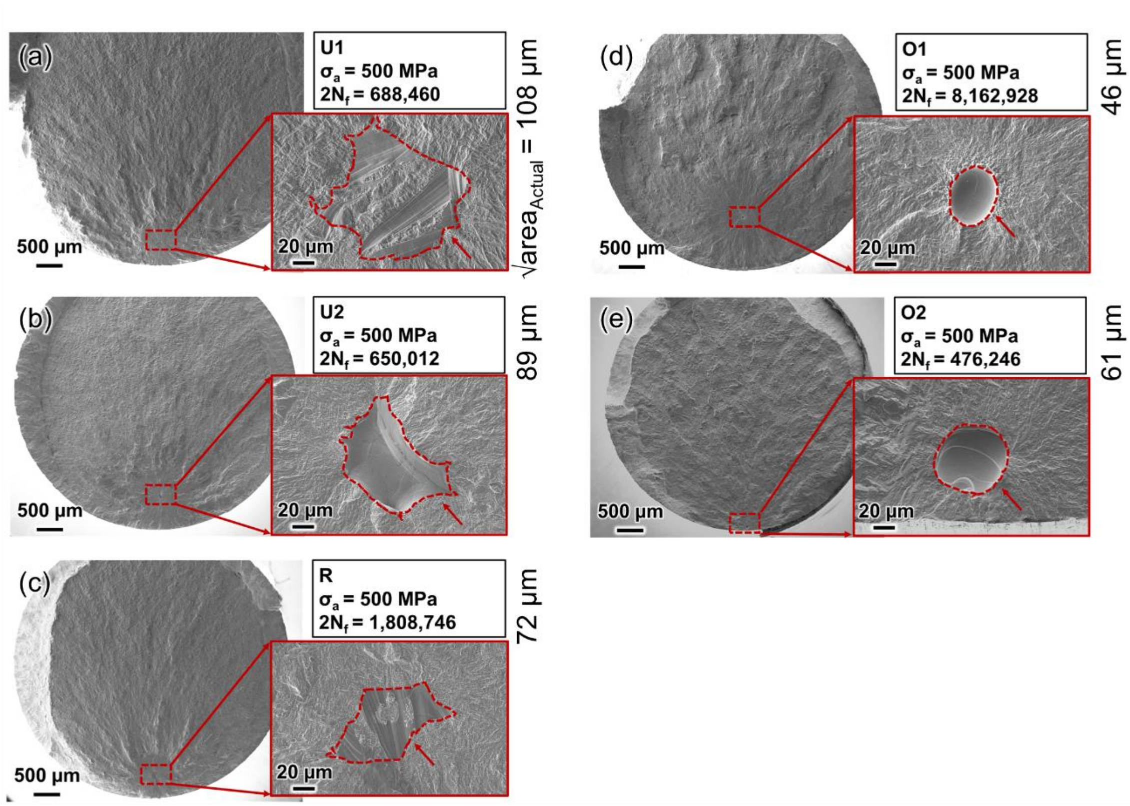

Figure A6-17. Fracture surfaces of L-PBF Ti-6Al-4V specimens fabricated using different process parameters.

References

[1] ISO/ASTM 52900. Additive manufacturing-General principles-Fundamentals and vocabulary. 2021.

[2] Mostafaei A, Zhao C, He Y, Reza Ghiaasiaan S, Shi B, Shao S, et al. Defects and anomalies in powder bed fusion metal additive manufacturing. Curr Opin Solid State Mater Sci 2022;26:100974. https://doi.org/10.1016/j.cossms.2021.100974.

[3] Molaei R, Fatemi A, Sanaei N, Pegues J, Shamsaei N, Shao S, et al. Fatigue of additive manufactured Ti-6Al-4V, Part II: The relationship between microstructure, material cyclic properties, and component performance. Int J Fatigue 2020;132:105363. https://doi.org/10.1016/j.ijfatigue.2019.105363.

[4] Yasin MS, Stonaker K, Shao S, Shamsaei N. Mechanical performance of laser powder bed fused Ti-6Al-4V: The influence of filter condition and part location. Additive Manufacturing Letters 2024;11:100255. https://doi.org/10.1016/j.addlet.2024.100255.

[5] Pegues JW, Shao S, Shamsaei N, Sanaei N, Fatemi A, Warner DH, et al. Fatigue of additive manufactured Ti-6Al-4V, Part I: The effects of powder feedstock, manufacturing, and post-process conditions on the resulting microstructure and defects. Int J Fatigue 2020;132:105358. https://doi.org/10.1016/j.ijfatigue.2019.105358.

[6] Gordon J V., Narra SP, Cunningham RW, Liu H, Chen H, Suter RM, et al. Defect structure process maps for laser powder bed fusion additive manufacturing. Addit Manuf 2020;36:101552. https://doi.org/10.1016/J.ADDMA.2020.101552.

[7] Kiss AM, Fong AY, Calta NP, Thampy V, Martin AA, Depond PJ, et al. Laser-Induced Keyhole Defect Dynamics during Metal Additive Manufacturing. Adv Eng Mater 2019;21:1900455. https://doi.org/10.1002/adem.201900455.

[8] Martin AA, Calta NP, Khairallah SA, Wang J, Depond PJ, Fong AY, et al. Dynamics of pore formation during laser powder bed fusion additive manufacturing. Nat Commun 2019;10. https://doi.org/10.1038/s41467-019-10009-2.

[9] Debroy T, David SA. Physical processes in fusion welding. Rev Mod Phys 1995;67:85. https://doi.org/10.1103/RevModPhys.67.85.

[10] Soltani-Tehrani A, Pegues J, Shamsaei N. Fatigue behavior of additively manufactured 17-4 PH stainless steel: The effects of part location and powder re-use. Addit Manuf 2020;36:101398. https://doi.org/10.1016/j.addma.2020.101398.

[11] Carrion PE, Soltani-Tehrani A, Phan N, Shamsaei N. Powder recycling effects on the tensile and fatigue behavior of additively manufactured Ti-6Al-4V parts. JOM 2019;71:963–73. https://doi.org/10.1007/s11837-018-3248-7.

[12] Soltani-Tehrani A, Shrestha R, Phan N, Seifi M, Shamsaei N. Establishing specimen property to part performance relationships for laser beam powder bed fusion additive manufacturing. Int J Fatigue 2021;151:106384. https://doi.org/10.1016/j.ijfatigue.2021.106384.

[13] Yadollahi A, Shamsaei N. Additive manufacturing of fatigue resistant materials: Challenges and opportunities. Int J Fatigue 2017;98:14–31. https://doi.org/10.1016/j.ijfatigue.2017.01.001.

[14] Stephens RI, Fatemi A, Stephens RR, Fuchs HO. Metal fatigue in engineering, 2nd Edition. 2000.

[15] Torries B, Imandoust A, Beretta S, Shao S, Shamsaei N. Overview on Microstructure- and Defect-Sensitive Fatigue Modeling of Additively Manufactured Materials. JOM 2018. https://doi.org/10.1007/s11837-018-2987-9.

[16] Kim FH, Moylan SP. Literature review of metal additive manufacturing defects. Gaithersburg, MD: 2018. https://doi.org/10.6028/NIST.AMS.100-16.

[17] Bauereiß A, Scharowsky T, Körner C. Defect generation and propagation mechanism during additive manufacturing by selective beam melting. J Mater Process Technol 2014;214. https://doi.org/10.1016/j.jmatprotec.2014.05.002.

[18] King WE, Barth HD, Castillo VM, Gallegos GF, Gibbs JW, Hahn DE, et al. Observation of keyhole-mode laser melting in laser powder-bed fusion additive manufacturing. J Mater Process Technol 2014;214:2915–25. https://doi.org/10.1016/j.jmatprotec.2014.06.005.

[19] Sterling AJ, Torries B, Shamsaei N, Thompson SM, Seely DW. Fatigue behavior and failure mechanisms of direct laser deposited Ti–6Al–4V. Materials Science and Engineering: A 2016;655:100–12. https://doi.org/10.1016/j.msea.2015.12.026.

[20] Shao S, Poudel A, Shamsaei N. A linear elastic finite element approach to fatigue life estimation for defect laden materials. Eng Fract Mech 2023;285:109298. https://doi.org/10.1016/j.engfracmech.2023.109298.

[21] Härkegård G. Intrinsic-crack modelling of the notch fatigue limit of a solid with an elliptical-cylindrical or a spheroidal cavity. Eng Fract Mech 2023;279:109057. https://doi.org/10.1016/j.engfracmech.2023.109057.

[22] Serrano-Munoz I, Buffiere J-Y, Mokso R, Verdu C, Nadot Y. Location, location & size: defects close to surfaces dominate fatigue crack initiation. Sci Rep 2017;7:45239. https://doi.org/10.1038/srep45239.

[23] Nadot Y. Fatigue from defect: Influence of size, type, position, morphology and loading. Int J Fatigue 2022;154:106531. https://doi.org/10.1016/j.ijfatigue.2021.106531.

[24] Junet A, Messager A, Weck A, Nadot Y, Boulnat X, Buffiere J-Y. Internal fatigue crack propagation in a Ti-6Al-4V alloy: An in situ study. Int J Fatigue 2023;168:107450. https://doi.org/10.1016/j.ijfatigue.2022.107450.

[25] Messager A, Junet A, Palin-Luc T, Buffiere J, Saintier N, Ranc N, et al. In situ synchrotron ultrasonic fatigue testing device for 3D characterisation of internal crack initiation and growth. Fatigue Fract Eng Mater Struct 2020;43:558–67. https://doi.org/10.1111/ffe.13140.

[26] Murakami Y. Effects of small defects and nonmetallic inclusions on the fatigue strength of metals. Key Eng Mater 1991;51–52:37–42. https://doi.org/10.4028/www.scientific.net/KEM.51-52.37.

[27] Merot P, Morel F, Robert C, Pessard E, Gallegos Mayorga L, Buttin P. Non local multiaxial fatigue modeling of defects : A unified approach to interpret size and shape effects. Theoretical and Applied Fracture Mechanics 2024;131:104378. https://doi.org/10.1016/j.tafmec.2024.104378.

[28] Snell R, Tammas-Williams S, Chechik L, Lyle A, Hernández-Nava E, Boig C, et al. Methods for Rapid Pore Classification in Metal Additive Manufacturing. JOM 2020;72:101–9. https://doi.org/10.1007/s11837-019-03761-9.

[29] Acar E, Haftka RT, Kim NH. Effects of structural tests on aircraft safety. AIAA Journal 2010;48:2235–48. https://doi.org/10.2514/1.J050202.

[30] Del Rosario Z, Iaccarino G, Fenrich RW. Fast precision margin with the first-order reliability method. AIAA Journal 2019;57:5042–53. https://doi.org/10.2514/1.J058345/ASSET/IMAGES/LARGE/FIGURE14.JPEG.

[31] del Rosario Z, Fenrich RW, Iaccarino G. Cutting the double loop: Theory and algorithms for reliability-based design optimization with parametric uncertainty. Int J Numer Methods Eng 2019;118:718–40. https://doi.org/10.1002/NME.6035;SUBPAGE:STRING:FULL.

[32] NASGRO® fracture mechanics & fatigue crack growth software | SwRI n.d. https://www.swri.org/consortia/nasgro (accessed October 27, 2022).

[33] Zhang W, Wang Q, Li X, He J. A simple fatigue life prediction algorithm using the modified NASGRO equation. Math Probl Eng 2016;2016:1–8. https://doi.org/10.1155/2016/4298507.

[34] Harter JA. Comparison of contemporary FCG life prediction tools. Int J Fatigue 1999;21:S181–5. https://doi.org/10.1016/S0142-1123(99)00070-5.

[35] Harter JA. Afgrow Users Guide and Technical Manual. Interface 2008.

[36] Han S, Dinh TD, De Baere I, Boone M, Josipovic I, Van Paepegem W. Study of the effect of defects on fatigue life prediction of additive manufactured Ti-6Al-4V by combined use

of micro-computed tomography and fracture-mechanics-based simulation. Int J Fatigue 2024;180:108110. https://doi.org/10.1016/j.ijfatigue.2023.108110.

[37] Serrano-Munoz I, Buffiere JY, Mokso R, Verdu C, Nadot Y. Location, location &size: Defects close to surfaces dominate fatigue crack initiation. Sci Rep 2017. https://doi.org/10.1038/srep45239.

[38] Ahmed Obeidi M, Uí Mhurchadha SM, Raghavendra R, Conway A, Souto C, Tormey D, et al. Comparison of the porosity and mechanical performance of 316L stainless steel manufactured on different laser powder bed fusion metal additive manufacturing machines. Journal of Materials Research and Technology 2021;13. https://doi.org/10.1016/j.jmrt.2021.06.027.

[39] America Makes, AMSC. Standardization Roadmap for Additive Manufacturing - Version 2.0. America Makes & ANSI Additive Manufacturing Standardization Collaborative (AMSC) 2018;2:1–203.

[40] Leyens C, Peters M. Titanium and Titanium Alloys. Wiley; 2003. https://doi.org/10.1002/3527602119.

[41] Oh IH, Nomura N, Masahashi N, Hanada S. Mechanical properties of porous titanium compacts prepared by powder sintering. Scr Mater 2003;49:1197–202. https://doi.org/10.1016/j.scriptamat.2003.08.018.

[42] Niinomi M. Mechanical biocompatibilities of titanium alloys for biomedical applications. J Mech Behav Biomed Mater 2008;1:30–42. https://doi.org/10.1016/j.jmbbm.2007.07.001.

[43] Chi W, Wang W, Li Y, Xu W, Sun C. Defect induced cracking and modeling of fatigue strength for an additively manufactured Ti-6Al-4V alloy in very high cycle fatigue regime. Theoretical and Applied Fracture Mechanics 2022;119:103380. https://doi.org/10.1016/J.TAFMEC.2022.103380.

[44] Masuo H, Tanaka Y, Morokoshi S, Yagura H, Uchida T, Yamamoto Y, et al. Influence of defects, surface roughness and HIP on the fatigue strength of Ti-6Al-4V manufactured by additive manufacturing. Int J Fatigue 2018. https://doi.org/10.1016/j.ijfatigue.2018.07.020.

[45] Fatemi A, Molaei R, Simsiriwong J, Sanaei N, Pegues J, Torries B, et al. Fatigue behaviour of additive manufactured materials: An overview of some recent experimental studies on Ti-6Al-4V considering various processing and loading direction effects. Fatigue Fract Eng Mater Struct 2019;42:991–1009. https://doi.org/10.1111/ffe.13000.

[46] Murakami Y. Material Defects as the Basis of Fatigue Design. Int J Fatigue 2012;41:2–10.

[47] Yamashita Y, Murakami T, Mihara R, Okada M, Murakami Y. Defect analysis and fatigue design basis for Ni-based superalloy 718 manufactured by selective laser melting. Int J Fatigue 2018;117:485–95. https://doi.org/10.1016/j.ijfatigue.2018.08.002.

[48] Murakami Y, Endo M. Effects of defects, inclusions and inhomogeneities on fatigue strength. Int J Fatigue 1994;16:163–82. https://doi.org/10.1016/0142-1123(94)90001-9.

[49] Murakami Y, Endo T. Effects of small defects on fatigue strength of metals. Int J Fatigue 1980;2:23–30. https://doi.org/10.1016/0142-1123(80)90024-9.

[50] El Haddad MH, Topper TH, Smith KN. Prediction of non propagating cracks. Eng Fract Mech 1979;11:573–84. https://doi.org/10.1016/0013-7944(79)90081-X.

[51] Alegre JM, Cuesta II, Díaz A. Stress-intensity factor solutions for embedded elliptical cracks in round bars subjected to tensile load. Theoretical and Applied Fracture Mechanics 2022;117:103189. https://doi.org/10.1016/j.tafmec.2021.103189.

[52] Zerbst U, Madia M, Schork B, Hensel J, Kucharczyk P, Ngoula D, et al. Fatigue and Fracture of Weldments. Fatigue and Fracture of Weldments, 2019. https://doi.org/10.1007/978-3-030-04073-4_1.

[53] Beretta S, Romano S. A comparison of fatigue strength sensitivity to defects for materials manufactured by AM or traditional processes. Int J Fatigue 2017;94:178–91. https://doi.org/10.1016/j.ijfatigue.2016.06.020.

[54] Romano S, Patriarca L, Foletti S, Beretta S. LCF behaviour and a comprehensive life prediction model for AlSi10Mg obtained by SLM. Int J Fatigue 2018;117:47–62. https://doi.org/10.1016/j.ijfatigue.2018.07.030.

[55] Sanaei N, Fatemi A. Defects in additive manufactured metals and their effect on fatigue performance: A state-of-the-art review. Prog Mater Sci 2021;117:100724. https://doi.org/10.1016/j.pmatsci.2020.100724.

[56] Romano S, Nezhadfar PD, Shamsaei N, Seifi M, Beretta S. High cycle fatigue behavior and life prediction for additively manufactured 17-4 PH stainless steel: Effect of sub-surface porosity and surface roughness. Theoretical and Applied Fracture Mechanics 2020;106:102477. https://doi.org/10.1016/j.tafmec.2020.102477.

[57] Murakami Y, Takagi T, Wada K, Matsunaga H. Essential structure of S-N curve: Prediction of fatigue life and fatigue limit of defective materials and nature of scatter. Int J Fatigue 2021;146:106138. https://doi.org/10.1016/j.ijfatigue.2020.106138.

[58] Poudel A, Yasin MS, Ye J, Liu J, Vinel A, Shao S, et al. Feature-based volumetric defect classification in metal additive manufacturing. Nat Commun 2022;13:6369. https://doi.org/10.1038/s41467-022-34122-x.

[59] Kasperovich G, Haubrich J, Gussone J, Requena G. Correlation between porosity and processing parameters in TiAl6V4 produced by selective laser melting. Mater Des 2016;105:160–70. https://doi.org/10.1016/j.matdes.2016.05.070.

[60] Ferro P, Fabrizi A, Berto F, Savio G, Meneghello R, Rosso S. Defects as a root cause of fatigue weakening of additively manufactured AlSi10Mg components. Theoretical and Applied Fracture Mechanics 2020;108:102611. https://doi.org/10.1016/j.tafmec.2020.102611.

[61] Zhang Z, Zhi G, Liu Y, Chen Y, Rong P, Ma S, et al. Microstructure and properties nonuniformity of Ti6Al4V component fabricated by high-power laser melting deposition. Materials Science and Engineering: A 2024;902:146604. https://doi.org/10.1016/j.msea.2024.146604.

[62] Naragani D, Sangid MD, Shade PA, Schuren JC, Sharma H, Park JS, et al. Investigation of fatigue crack initiation from a non-metallic inclusion via high energy x-ray diffraction microscopy. Acta Mater 2017;137:71–84. https://doi.org/10.1016/J.ACTAMAT.2017.07.027.

[63] Vincent M, Nadot-Martin C, Nadot Y, Dragon A. Fatigue from defect under multiaxial loading: Defect Stress Gradient (DSG) approach using ellipsoidal Equivalent Inclusion Method. Int J Fatigue 2014;59:176–87. https://doi.org/10.1016/j.ijfatigue.2013.08.027.

[64] Wu Z, Wu S, Bao J, Qian W, Karabal S, Sun W, et al. The effect of defect population on the anisotropic fatigue resistance of AlSi10Mg alloy fabricated by laser powder bed fusion. Int J Fatigue 2021;151:106317. https://doi.org/10.1016/j.ijfatigue.2021.106317.

[65] Niu X, He C, Zhu SP, Foti P, Berto F, Wang L, et al. Defect sensitivity and fatigue design: Deterministic and probabilistic aspects in additively manufactured metallic materials. Prog Mater Sci 2024;144:101290. https://doi.org/10.1016/J.PMATSCI.2024.101290.

[66] Zhu S-P, Ai Y, Liao D, Correia JAFO, De Jesus AMP, Wang Q. Recent advances on size effect in metal fatigue under defects: a review. Int J Fract 2022;234:21–43. https://doi.org/10.1007/s10704-021-00526-x.

[67] Chen H, Wang X, Ren X. Size effect on fatigue performance of SLM-ed AlSi10Mg alloy: Role of defect size distribution. Int J Fatigue 2024;182. https://doi.org/10.1016/j.ijfatigue.2024.108163.

[68] Merot P, Morel F, Gallegos Mayorga L, Pessard E, Buttin P, Baffie T. Observations on the influence of process and corrosion related defects on the fatigue strength of 316L stainless steel manufactured by Laser Powder Bed Fusion (L-PBF). Int J Fatigue 2022;155. https://doi.org/10.1016/j.ijfatigue.2021.106552.

[69] Beretta S. More than 25 years of extreme value statistics for defects: Fundamentals, historical developments, recent applications. Int J Fatigue 2021;151:106407. https://doi.org/10.1016/j.ijfatigue.2021.106407.

[70] Beretta S, Anderson C, Murakami Y. Extreme value models for the assessment of steels containing multiple types of inclusion. Acta Mater 2006;54:2277–89. https://doi.org/10.1016/j.actamat.2006.01.016.

[71] Soltani-Tehrani A, Isaac JP, Tippur H V., Silva DF, Shao S, Shamsaei N. Ti-6Al-4V powder reuse in laser powder bed fusion (L-PBF): The effect on porosity, microstructure, and mechanical behavior. Int J Fatigue 2023;167:107343. https://doi.org/10.1016/j.ijfatigue.2022.107343.

[72] Gupta A, Bennett CJ, Sun W. High cycle fatigue performance evaluation of a laser powder bed fusion manufactured Ti-6Al-4V bracket for aero-engine applications. Eng Fail Anal 2022;140. https://doi.org/10.1016/j.engfailanal.2022.106494.

[73] Liu Z, He B, Lyu T, Zou Y. A Review on Additive Manufacturing of Titanium Alloys for Aerospace Applications: Directed Energy Deposition and Beyond Ti-6Al-4V. JOM 2021;73. https://doi.org/10.1007/s11837-021-04670-6.

[74] Dang L, He X, Tang D, Xin H, Wang X, Wu B, et al. Pore-induced fatigue failure: Critical pore criterion for Ti-6Al-4V alloy manufactured by laser-directed energy deposition. Theoretical and Applied Fracture Mechanics 2024;129:104204. https://doi.org/10.1016/j.tafmec.2023.104204.

[75] Carson C. Heat treating of titanium and titanium alloys. Heat treating of nonferrous alloys, ASM International; 2018, p. 511–34. https://doi.org/10.31399/asm.hb.v04e.a0006283.

[76] Schmidt FF, Wood RA. Heat treatment of Titanium and Titanium alloys. NASA Tech Memo 1966.

[77] ASTM E8/E8M. Standard test methods for tension testing of metallic materials 1. Annual Book of ASTM Standards 4 2010:1–27. https://doi.org/10.1520/E0008.

[78] ASTM International. E466-15 Standard Practice for Conducting Force Controlled Constant Amplitude Axial Fatigue Tests of Metallic Materials. West Conshohocken, PA; ASTM International 2015. https://doi.org/https://doi.org/10.1520/E0466-15.

[79] ASTM E3. ASTM E3 Standard Guide for Preparation of Metallographic Specimens Standard Guide for Preparation of Metallographic Specimens 1. ASTM International 2017;03.01:1–12. https://doi.org/10.1520/E0003-11R17.1.

[80] Zaefferer S, Elhami NN. Theory and application of electron channelling contrast imaging under controlled diffraction conditions. Acta Mater 2014;75:20–50. https://doi.org/10.1016/J.ACTAMAT.2014.04.018.

[81] Engblom E. Effect of oxygen concentration in build chamber during laser metal deposition of Ti-64 wire. 2018.

[82] Dietrich K, Diller J, Dubiez-Le Goff S, Bauer D, Forêt P, Witt G. The influence of oxygen on the chemical composition and mechanical properties of Ti-6Al-4V during laser powder bed fusion (L-PBF). Addit Manuf 2020;32:100980. https://doi.org/10.1016/j.addma.2019.100980.

[83] ASTM F2924-14. Standard specification for additive manufacturing Ti-6Al-4V with Powder Bed Fusion 2014. https://doi.org/10.1520/F2924-14R21.

[84] Schneider CA, Rasband WS, Eliceiri KW. NIH Image to ImageJ: 25 years of image analysis. Nat Methods 2012;9. https://doi.org/10.1038/nmeth.2089.

[85] Murakami Y, Nemat-Nasser S. Growth and stability of interacting surface flaws of arbitrary shape. Eng Fract Mech 1983;17:193–210. https://doi.org/10.1016/0013-7944(83)90027-9.

[86] Yasin MS, Jam A, Habibnejad-Korayem M, Haghshenas M, Shao S, Shamsaei N. Additively manufactured Ti-5Al-5V-5Mo-3Cr: Understanding defect-fatigue relationships. Int J Fatigue 2024;187:108426. https://doi.org/10.1016/j.ijfatigue.2024.108426.

[87] Soltani-Tehrani A, Habibnejad-Korayem M, Shao S, Haghshenas M, Shamsaei N. Ti-6Al-4V powder characteristics in laser powder bed fusion: The effect on tensile and fatigue behavior. Addit Manuf 2022;51:102584. https://doi.org/10.1016/j.addma.2021.102584.

[88] ASTM E2283. Practice for extreme value analysis of nonmetallic inclusions in steel and other microstructural features 2019. https://doi.org/10.1520/E2283-08R19.

[89] Ye J, Poudel A, Liu J, Vinel A, Silva D, Shao S, et al. Machine learning augmented X-ray computed tomography features for volumetric defect classification in laser beam powder bed fusion. The International Journal of Advanced Manufacturing Technology 2023;126:3093–107. https://doi.org/10.1007/s00170-023-11281-9.

[90] du Plessis A, Yadroitsava I, Yadroitsev I. Effects of defects on mechanical properties in metal additive manufacturing: A review focusing on X-ray tomography insights. Mater Des 2020;187:108385. https://doi.org/10.1016/j.matdes.2019.108385.

[91] Baig S, Jam A, Beretta S, Shao S, Shamsaei N. Non-destructive detection of critical defects in additive manufacturing. Sci Rep 2025;15:6740. https://doi.org/10.1038/s41598-025-91608-6.

[92] Gorelik M. Additive manufacturing in the context of structural integrity. Int J Fatigue 2017;94:168–77. https://doi.org/10.1016/J.IJFATIGUE.2016.07.005.

[93] Muhammad M, Yasin MS, Soman S, Shao S, Shamsaei N. Defect features critical to the fatigue of additively manufactured Ti-6Al-4V. Theoretical and Applied Fracture Mechanics 2025;138:104981. https://doi.org/10.1016/j.tafmec.2025.104981.

[94] Masoomi M, Pegues JW, Thompson SM, Shamsaei N. A numerical and experimental investigation of convective heat transfer during laser-powder bed fusion. Addit Manuf 2018;22:729–45. https://doi.org/10.1016/j.addma.2018.06.021.

[95] Rice RC, Jackson JL, Bakuckas J, Thompson S. Metallic materials properties development and standardization. 2003.

[96] Federal Aviation Administration. FAA AC 33.14-1: Damage tolerance for high energy turbine engine rotors n.d. https://www.faa.gov/regulations_policies/advisory_circulars/index.cfm/go/document.information/documentID/22920 (accessed June 8, 2025).

[97] Beretta S, Regazzi D. Probabilistic fatigue assessment for railway axles and derivation of a simple format for damage calculations. Int J Fatigue 2016;86:13–23. https://doi.org/10.1016/J.IJFATIGUE.2015.08.010.

[98] NASA-HBDK-5026. Guidance on strength, fatigue, and fracture control requirements for additively manufactured spaceflight hardware. 2024.

[99] Herausgeber F. Analytical strength assessment of components in mechanical engineering. 5th ed. 2003.

[100] ISO EN1993. Eurocode 3: Design of steel structures. 2005.

[101] Chee Tong Y. Literature review on aircraft structural risk and reliability analysis. 2001.

[102] Boyd-Lee AD, Harrison GF, Henderson MB. Evaluation of standard life assessment procedures and life extension methodologies for fracture-critical components. Int J Fatigue 2001;23:11–9. https://doi.org/10.1016/S0142-1123(01)00116-5.

[103] Zerbst U, Bruno G, Buffière JY, Wegener T, Niendorf T, Wu T, et al. Damage tolerant design of additively manufactured metallic components subjected to cyclic loading: State of the art and challenges. Prog Mater Sci 2021;121:100786. https://doi.org/10.1016/J.PMATSCI.2021.100786.

[104] Maierhofer J, Kolitsch S, Pippan R, Gänser HP, Madia M, Zerbst U. The cyclic R-curve – Determination, problems, limitations and application. Eng Fract Mech 2018;198:45–64. https://doi.org/10.1016/J.ENGFRACMECH.2017.09.032.

[105] Murakami Y, Endo M. Prediction model of S-N curve without fatigue test or with a minimum number of fatigue tests. Eng Fail Anal 2023;154:107647. https://doi.org/10.1016/j.engfailanal.2023.107647.

[106] Shiozawa K, Lu L. Effect of Non-Metallic Inclusion Size and Residual Stresses on Gigacycle Fatigue Properties in High Strength Steel. Adv Mat Res 2008;44–46:33–42. https://doi.org/10.4028/WWW.SCIENTIFIC.NET/AMR.44-46.33.

[107] Tenkamp J, Stern F, Walther F. Uniform fatigue damage tolerance assessment for additively manufactured and cast Al-Si alloys: An elastic-plastic fracture mechanical approach. Additive Manufacturing Letters 2022;3:100054. https://doi.org/10.1016/J.ADDLET.2022.100054.

[108] Beretta S, Patriarca L, Gargourimotlagh M, Hardaker A, Brackett D, Salimian M, et al. A benchmark activity on the fatigue life assessment of AlSi10Mg components manufactured by L-PBF. Mater Des 2022;218:110713. https://doi.org/10.1016/J.MATDES.2022.110713.

[109] Macallister N, Becker TH. Fatigue life estimation of additively manufactured Ti-6Al-4V: Sensitivity, scatter and defect description in Damage-tolerant models. Acta Mater 2022;237:118189. https://doi.org/10.1016/J.ACTAMAT.2022.118189.

[110] Yadollahi A, Mahtabi MJ, Khalili A, Doude HR, Newman JC. Fatigue life prediction of additively manufactured material: Effects of surface roughness, defect size, and shape. Fatigue Fract Eng Mater Struct 2018;41:1602–14. https://doi.org/10.1111/ffe.12799.

[111] Ng GKL, Jarfors AEW, Bi G, Zheng HY. Porosity formation and gas bubble retention in laser metal deposition. Applied Physics A 2009;97:641. https://doi.org/10.1007/s00339-009-5266-3.

[112] Wang L, Zhang Y, Chia HY, Yan W. Mechanism of keyhole pore formation in metal additive manufacturing. NPJ Comput Mater 2022;8:22. https://doi.org/10.1038/s41524-022-00699-6.

[113] Kies F, Wilms MB, Pirch N, Pradeep KG, Schleifenbaum JH, Haase C. Defect formation and prevention in directed energy deposition of high-manganese steels and the effect on mechanical properties. Materials Science and Engineering: A 2020;772:138688. https://doi.org/10.1016/j.msea.2019.138688.

[114] ASTM E466. Standard practice for conducting force controlled constant amplitude axial fatigue tests of metallic materials. West Conshohocken, PA 2002:1–6. https://doi.org/10.1520/E0466-07.2.

[115] Ahmad A, Prevey P, Rudd C. Residual stress measurement by X-ray diffraction. SAE HS-784, SAE International, Warrendale, PA 2003.

[116] ASTM E739. Practice for statistical analysis of linear or linearized stress-life (S-N) and strain-life (ε-N) fatigue data 2015. https://doi.org/10.1520/E0739-10R15.

[117] Nelson W. Applied life data analysis. Wiley; 1982. https://doi.org/10.1002/0471725234.

[118] Federal Aviation Administration. 14 CFR part 25 subpart D -- design and construction (FAR part 25 subpart D) n.d. https://www.ecfr.gov/current/title-14/chapter-I/subchapter-C/part-25/subpart-D (accessed May 7, 2025).

[119] Syed AK, Vesga W, Dutton B, Berentshaw T, Zhang X. Defect tolerance and fatigue limit prediction for laser powder bed fusion Ti6Al4V. Int J Fatigue 2024;184:108285. https://doi.org/10.1016/j.ijfatigue.2024.108285.

[120] Zou J, Xia X, Feng Z, Wang J, Guo Y, Gao D. The fatigue mechanism and a new defect-based life prediction model for selective laser melted Al-Mg-Sc-Zr alloy. Int J Fatigue 2025;190:108590. https://doi.org/10.1016/J.IJFATIGUE.2024.108590.

[121] Shiozawa K, Lu L. Effect of non-metallic inclusion size and residual stresses on gigacycle fatigue properties in high strength steel. Adv Mat Res 2008;44–46:33–42. https://doi.org/10.4028/www.scientific.net/AMR.44-46.33.

[122] Paris PC, Gomez MP, Anderson WE. A rational analytic theory of fatigue. The Trend in Engineering 1961;13:9–14.

[123] Paris P, Erdogan F. A critical analysis of crack propagation laws. Journal of Basic Engineering 1963;85:528–33. https://doi.org/10.1115/1.3656900.

[124] Minerva G, Awd M, Tenkamp J, Walther F, Beretta S. Machine learning-assisted extreme value statistics of anomalies in AlSi10Mg manufactured by L-PBF for robust fatigue strength predictions. Mater Des 2023;235:112392. https://doi.org/10.1016/j.matdes.2023.112392.

[125] Junet A, Messager A, Boulnat X, Weck A, Boller E, Helfen L, et al. Fabrication of artificial defects to study internal fatigue crack propagation in metals. Scr Mater 2019;171:87–91. https://doi.org/10.1016/j.scriptamat.2019.05.018.

[126] Junet A, Messager A, Weck A, Nadot Y, Boulnat X, Buffiere JY. Internal fatigue crack propagation in a Ti-6Al-4V alloy: An in situ study. Int J Fatigue 2023;168:107450. https://doi.org/10.1016/J.IJFATIGUE.2022.107450.

[127] Chi W, Li G, Wang W, Sun C. Interior initiation and early growth of very high cycle fatigue crack in an additively manufactured Ti-alloy. Int J Fatigue 2022;160:106862. https://doi.org/10.1016/J.IJFATIGUE.2022.106862.

[128] Caivano R, Tridello A, Chiandussi G, Qian G, Paolino D, Berto F. Very high cycle fatigue (VHCF) response of additively manufactured materials: A review. Fatigue Fract Eng Mater Struct 2021;44:2919–43. https://doi.org/10.1111/FFE.13567.

[129] Muhammad M, Lee S, Frye P, Simsiriwong J, Shao S, Shamsaei N. High cycle and very high cycle fatigue behavior of additively manufactured Inconel 718: Effects of stress-relieving, surface texture, part orientation, and test frequency. Eng Fail Anal 2025;169:109227. https://doi.org/10.1016/J.ENGFAILANAL.2024.109227.

[130] Tenkamp J, Awd M, Siddique S, Starke P, Walther F. Fracture–mechanical assessment of the effect of defects on the fatigue lifetime and limit in cast and additively manufactured

aluminum–silicon alloys from HCF to VHCF regime. Metals 2020, Vol 10, Page 943 2020;10:943. https://doi.org/10.3390/MET10070943.

[131] Bonneric M, Saintier N, El Khoukhi D, Bega J. Influence of the defect size, type, and position on the High Cycle Fatigue behavior of Ti-6Al-4V processed by laser powder bed fusion. Int J Fatigue 2025;193:108783. https://doi.org/10.1016/J.IJFATIGUE.2024.108783.

[132] Yoshinaka F, Nakamura T, Takeuchi A, Uesugi M, Uesugi K. Initiation and growth behaviour of small internal fatigue cracks in Ti-6Al-4V via synchrotron radiation microcomputed tomography. Fatigue Fract Eng Mater Struct 2019;42:2093–105. https://doi.org/10.1111/FFE.13085.

[133] Yoshinaka F, Nakamura T, Takaku K. Effects of vacuum environment on small fatigue crack propagation in Ti–6Al–4V. Int J Fatigue 2016;91:29–38. https://doi.org/10.1016/J.IJFATIGUE.2016.05.024.

[134] Miedlar PC, Berens AP, Gunderson A, Gallagher JP. Analysis and support initiative for structural technology (ASIST) delivery order 0016: USAF damage tolerant design Handbook: Guidelines for the analysis and design of damage tolerant aircraft Structures. 2002.

[135] Forman R, Shivakumar V. Growth behavior of surface cracks in the circumferential plane of solid and hollow cylinders. Fracture Mechanics: Seventeenth Volume, ASTM International100 Barr Harbor Drive, PO Box C700, West Conshohocken, PA 19428-2959; 1986, p. 59–74. https://doi.org/10.1520/STP17388S.

[136] Sajith S, Murthy KSRK, Robi PS. Experimental and numerical investigation of mixed mode fatigue crack growth models in aluminum 6061-T6. Int J Fatigue 2020;130:105285. https://doi.org/10.1016/j.ijfatigue.2019.105285.

[137] Newman J, Raju I. Stress-intensity factor equations for cracks in three-dimensional finite bodies. 1984.

[138] Alegre JM, Cuesta II, Díaz A. Closed-form equations for the calculation of stress intensity factors for embedded cracks in round bars subjected to tensile load. Theoretical and Applied Fracture Mechanics 2022;121:103438. https://doi.org/10.1016/J.TAFMEC.2022.103438.

[139] Gumbel EJ. Statistics of extremes. Columbia University Press; 1958. https://doi.org/10.7312/GUMB92958/HTML.

[140] Beretta S, Murakami Y. Statistical analysis of defects for fatigue strength prediction and quality control of materials. Fatigue Fract Eng Mater Struct 1998;21:1049–65. https://doi.org/10.1046/J.1460-2695.1998.00104.X.

[141] Leverant GR, Millwater HR, McClung RC, Enright MP. A New Tool for Design and Certification of Aircraft Turbine Rotors. J Eng Gas Turbine Power 2004;126:155–9. https://doi.org/10.1115/1.1622409.

[142] Fjeldstad A, Wormsen A, Härkegård G. Simulation of fatigue crack growth in components with random defects. Eng Fract Mech 2008;75:1184–203. https://doi.org/10.1016/J.ENGFRACMECH.2007.04.006.

[143] Minerva G, Awd M, Koch A, Walther F, Beretta S. Transferability of anomaly data to fatigue properties of PBF-LB AlSi10Mg parts with different volumes. Int J Fatigue 2025;195:108852. https://doi.org/10.1016/J.IJFATIGUE.2025.108852.

[144] DNV GL. DNVGL-RP-C203: Fatigue design of offshore steel structures. DNV GL - Recommended Practice 2016.

[145] Lotsberg I, Sigurdsson G, Fjeldstad A, Moan T. Probabilistic methods for planning of inspection for fatigue cracks in offshore structures. Marine Structures 2016;46:167–92. https://doi.org/10.1016/J.MARSTRUC.2016.02.002.

[146] Tridello A, Boursier Niutta C, Rossetto M, Berto F, Paolino DS. Fatigue Design Curves for Industrial Applications: A Review. Fatigue Fract Eng Mater Struct 2025;48:1001–21. https://doi.org/10.1111/FFE.14545.

[147] Antunes RA, Salvador CAF, Oliveira MCL de. Materials selection of optimized titanium alloys for aircraft applications. Materials Research 2018;21:e20170979. https://doi.org/10.1590/1980-5373-mr-2017-0979.

[148] Crossley FJ. Aircraft applications of titanium: A review of the past and potential for the future. J Aircr 1981;18:993–1002. https://doi.org/10.2514/3.57592.

[149] Singh P, Pungotra H, Kalsi NS. On the characteristics of titanium alloys for the aircraft applications. Mater Today Proc 2017;4:8971–82. https://doi.org/10.1016/J.MATPR.2017.07.249.

[150] Eric W, Claus E, Shafaqat S, Frank W. High cycle fatigue (HCF) performance of Ti-6Al-4V alloy processed by selective laser melting. Adv Mat Res, 2013. https://doi.org/10.4028/www.scientific.net/AMR.816-817.134.

[151] Soltani-Tehrani A, Yasin MS, Shao S, Haghshenas M, Shamsaei N. Effects of Powder Particle Size on Fatigue Performance of Laser Powder-Bed Fused Ti-6Al-4V. Procedia Structural Integrity 2022;38:84–93. https://doi.org/10.1016/j.prostr.2022.03.010.

[152] Antonysamy AA, Meyer J, Prangnell PB. Effect of build geometry on the β-grain structure and texture in additive manufacture of Ti6Al4V by selective electron beam melting. Mater Charact 2013;84:153–68. https://doi.org/10.1016/j.matchar.2013.07.012.

[153] Razavi SMJ, Van Hooreweder B, Berto F. Effect of build thickness and geometry on quasi-static and fatigue behavior of Ti-6Al-4V produced by Electron Beam Melting. Addit Manuf 2020;36:101426. https://doi.org/10.1016/j.addma.2020.101426.

[154] Beretta S, Gargourimotlagh M, Foletti S, du Plessis A, Riccio M. Fatigue strength assessment of "as built" AlSi10Mg manufactured by SLM with different build orientations. Int J Fatigue 2020;139:105737. https://doi.org/10.1016/j.ijfatigue.2020.105737.

[155] Ghorbanpour S, Deshmukh K, Sahu S, Riemslag T, Reinton E, Borisov E, et al. Additive manufacturing of functionally graded inconel 718: Effect of heat treatment and building orientation on microstructure and fatigue behaviour. Journal of Materials Processing Tech 2022;306:117573. https://doi.org/10.1016/j.jmatprotec.2022.117573.

[156] Muhammad M, Yasin MS, Soman S, Beretta S, Shao S, Shamsaei N. A fracture mechanics based semi-probabilistic fatigue lifing approach for additively manufactured Ti-6Al-4V (Submitted). Theoretical and Applied Fracture Mechanics 2025.

[157] Oliveira JP, LaLonde AD, Ma J. Processing parameters in laser powder bed fusion metal additive manufacturing. Mater Des 2020;193:108762. https://doi.org/10.1016/J.MATDES.2020.108762.

[158] E466-15. Practice for conducting force controlled constant amplitude axial fatigue tests of metallic materials. ASTM Book of Standards 2015. https://doi.org/10.1520/E0466-15.2.

[159] Kitagawa H, Takahashi S. Applicability of fracture mechanics to very small cracks or the cracks in the early stage. In: Proc 2nd Int conf mech behaviour of mater - ICM2, 1976.

[160] Beretta S, Carboni M, Madia M. Modelling of fatigue thresholds for small cracks in a mild steel by “Strip-Yield” model. Eng Fract Mech 2009;76:1548–61. https://doi.org/10.1016/j.engfracmech.2009.04.015.

[161] Romano S, Brückner-Foit A, Brandão A, Gumpinger J, Ghidini T, Beretta S. Fatigue properties of AlSi10Mg obtained by additive manufacturing: Defect-based modelling and prediction of fatigue strength. Eng Fract Mech 2018;187:165–89. https://doi.org/10.1016/j.engfracmech.2017.11.002.

[162] Maierhofer J, Gänser H-P, Pippan R. Modified Kitagawa–Takahashi diagram accounting for finite notch depths. Int J Fatigue 2015;70:503–9. https://doi.org/10.1016/j.ijfatigue.2014.07.007.

[163] Moriarty PJ, Holley WE, Butterfield SP. Extrapolation of extreme and fatigue loads using probabilistic methods 2004. https://doi.org/10.2172/15011693.

[164] Sausto F, Carrion PE, Shamsaei N, Beretta S. Fatigue failure mechanisms for AlSi10Mg manufactured by L-PBF under axial and torsional loads: The role of defects and residual

stresses. Int J Fatigue 2022;162:106903. https://doi.org/10.1016/J.IJFATIGUE.2022.106903.

[165] Dowling NE. Mean stress effects in strain–life fatigue. Fatigue Fract Eng Mater Struct 2009;32:1004–19. https://doi.org/10.1111/J.1460-2695.2009.01404.X.